



HAL
open science

Multiscale modeling of laminated composites under extreme environmental conditions

Fangzhou Zhang

► **To cite this version:**

Fangzhou Zhang. Multiscale modeling of laminated composites under extreme environmental conditions. Mechanics [physics.med-ph]. École normale supérieure de Cachan - ENS Cachan, 2014. English. NNT : 2014DENS0027 . tel-01198997

HAL Id: tel-01198997

<https://theses.hal.science/tel-01198997>

Submitted on 15 Oct 2015

HAL is a multi-disciplinary open access archive for the deposit and dissemination of scientific research documents, whether they are published or not. The documents may come from teaching and research institutions in France or abroad, or from public or private research centers.

L'archive ouverte pluridisciplinaire **HAL**, est destinée au dépôt et à la diffusion de documents scientifiques de niveau recherche, publiés ou non, émanant des établissements d'enseignement et de recherche français ou étrangers, des laboratoires publics ou privés.



ENSC-2013/2014

**THÈSE DE DOCTORAT
DE L'ÉCOLE NORMALE SUPÉRIEURE DE CACHAN**

Présentée par

Fangzhou ZHANG

pour obtenir le grade de

DOCTEUR DE L'ÉCOLE NORMALE SUPÉRIEURE DE CACHAN

Domaine

MÉCANIQUE - GÉNIE MÉCANIQUE - GÉNIE CIVIL

Sujet de la thèse

**Multiscale modeling of laminated composites under
extreme environmental conditions**

Soutenance à Cachan le 11 juillet 2014 devant le jury composé de :

Christian Hochard	Professeur, Aix-Marseille Université	Rapporteur
Marco Gigliotti	Maître de Conférences, ENSMA	Rapporteur
Yves Remond	Professeur, Université de Strasbourg	Examineur
Jacques Cinquin	Ingénieur de recherche, AGI	Examineur
Jean-Mathieu Guimard	Ingénieur de recherche, AGI	Examineur
Pierre Ladevèze	Professeur, ENS Cachan	Directeur de thèse
Federica Daghia	Maître de Conférences, ENS Cachan	Co-encadrante

LMT-Cachan

ENS Cachan / CNRS / PRES UniverSud Paris

61 avenue du Président Wilson, F-94235 Cachan cedex, France

Acknowledgements

My deepest gratitude goes first and foremost to Professor Pierre Ladevèze, my doctoral advisor, for his guidance, his instructive advices and illuminating suggestions on my research.

High tribute shall be also paid to my co-advisor, Federica Daghia, who has generally gave me her time in helping me work out my problems during the difficult course of the thesis. Without her great patience, understanding and responsibility, this thesis could not have been completed or written.

I would like to express my gratitude to Christophe Cluzel for his precious advices and help on the experimental aspect of my study. I will surely benefit from the ‘Cahier de manip’ in my future research life.

Many thanks to Benjamin who has taught me how to polish a sample, to Lydia who has helped me resolve the administration problem, to Guillaume, Sylvain, Jérémy and Mahmoud who has corrected my bad French. I also owe an indebted to Emmanuel, to Xavier, to the team of CDC, to all the professors and students of LMT-Cachan for the help and the friendly environment they provided. It’s my honor to be a member of you.

Beyond the research, special thanks should go to my friends, Zhenzhen Yi, Huang He, Wang Yao, Zongzei Tang and Ergou Wangs, who have walked me through these years. Finally, I owe my sincere gratitude to my parents for their continuous support and great confidence in me. I would like to dedicate my thesis to them!

Contents

Introduction	1
1 Background	5
1.1 Introduction	6
1.2 The mesomodel of LMT-Cachan	6
1.2.1 Damage model for the ply	6
1.2.1.1 Diffuse damage	8
1.2.1.2 Transverse cracking damage	8
1.2.1.3 Fiber breakage damage	9
1.2.1.4 Inelasticity	10
1.2.2 Damage model for the interface	10
1.3 Oxidation aging on neat resin	12
1.3.1 The diffusion/reaction process	12
1.3.2 Effects of the oxidation aging	15
1.3.3 Coupling between oxidation and damage	17
1.4 Modeling of the oxidation aging on neat resin	18
1.4.1 General model of the diffusion/reaction process	18
1.4.2 Models of the oxidation reaction	19
1.4.2.1 Model of the temperature dependent reaction	19
1.4.2.2 Model based on the mechanistic schemes of the oxidation reaction	20
1.4.3 Models of the effects of the oxidation aging	22
1.5 Oxidation aging on composite material	24

1.5.1	The anisotropic propagation of the oxidation aging on a composite ply	25
1.5.2	Effects of the oxidation aging on composite materials	28
1.5.3	Damages and fractures of oxidized composite materials	30
1.6	Modeling of the oxidation aging on composite materials	31
1.6.1	Microscale models of the oxidation aging on composite materials	31
1.6.2	Mesoscale model of the anisotropic propagation	33
1.7	Conclusion	34
2	Preliminary observations on effects of the oxidation aging on the laminated composite material	37
2.1	Introduction	38
2.2	Preparations of samples	38
2.2.1	Material and aging conditions	38
2.2.2	Preparation of surfaces for microscopic observations	39
2.3	Preliminary observations with optical microscope	40
2.3.1	Light field illumination and dark field illumination	40
2.3.2	The anisotropic propagation of the oxidation aging	43
2.3.3	Coupling between the oxidation aging propagation and damage mechanisms	47
2.4	Conclusion	49
3	Micro-scale modeling and homogenization of the oxidized composite material	51
3.1	Introduction	52
3.2	The properties of the oxidized resin	52
3.3	Homogenization method	54
3.3.1	Homogenization without the effects of the oxidation aging	54
3.3.2	Homogenization with the effects of the oxidation aging	57
3.3.3	FEM calculations of a unit cell of composite materials	60
3.3.3.1	Modelling of a unit cell of unaged composite materials	60
3.3.3.2	Introducing the oxidation effects into the micro-scale models	62

3.4	Stress field around fibers	62
3.5	Homogenized properties of composite materials	64
3.5.1	Stiffness of unaged composite materials	64
3.5.2	Elastic modulus of aged composite materials	64
3.5.3	Shrinkage of aged composite materials	66
3.6	Discussion	66
4	Experimental characterization of the mechanical behavior of oxidized composite specimens	69
4.1	Introduction	70
4.2	Material and aging conditions	70
4.3	Quasi-static tensile test	71
4.3.1	Test setup	71
4.3.2	Digital image correlation (DIC)	72
4.3.3	Evaluating the kinetics of transverse cracking with DIC	74
4.3.4	Results	78
4.3.4.1	Global behavior of the aged and the unaged specimens	78
4.3.4.2	Crack density evolution	79
4.4	Non-destructive free vibration tests	81
4.4.1	Identification of the transverse modulus by vibration tests	81
4.4.2	Modeling of the free vibration tests	83
4.5	Conclusion	85
5	Towards a mesoscale modeling of transverse cracking in oxidized specimens	87
5.1	Introduction	88
5.2	Identification of G_c from the experimental results of the unaged samples	89
5.2.1	The micro-meso bridge for unaged plies	91
5.2.2	G_c of unaged samples	92
5.3	Modeling of the oxidized layer	94
5.3.1	Definition of a homogeneous equivalent oxidized layer	94
5.3.2	Oxidation profiles in the 90° ply	96

5.4	Micro-scale modeling of tranverse cracking of the oxidized samples . . .	98
5.4.1	Transverse cracking during oxidation aging	98
5.4.2	Transverse cracking kinetics of the aged samples under tensile loading	100
5.5	Meso-scale modeling of tranverse cracking of the oxidized samples . . .	105
5.6	Conclusion	106
6	The oxi-delamination test	109
6.1	Introduction	110
6.2	Material and experimental technology	110
6.2.1	The classical climbing drum peel test	111
6.2.2	Samples for the CDP tests	113
6.2.3	The oxi-delamination test: crack propagation driven by the oxidation	113
6.3	Results	115
6.3.1	G_c of unaged samples	115
6.3.2	Evolution of the displacement during the oxi-delamination tests	116
6.3.3	The propagation velocities under different external loads	117
6.4	Modeling of G_c at different oxidation levels	118
6.5	Conclusions	120
	Conclusion and perspectives	121
	Bibliography	141

Introduction

Composite materials have been increasingly used in the aeronautic industry thanks to their excellent specific properties (strength and stiffness) and fatigue resistance. The aeronautic industry today is searching for powerful simulation for these materials to replace the tests on real structures with the less expensive virtual tests. Several approaches exist to meet this demand. The approaches called “micro” [1, 2] describe precisely the behavior of composite materials with non-homogeneous components or discrete damage mechanisms, but they are too computationally expensive to describe the complete behavior until failure of laminated composites. In contrast, approaches called “macro” [3] based on global failure criteria of laminated composites, cost less but are often not accurate enough to predict the final fracture in more general situations. For thirty years, the LMT-Cachan has developed a model at an intermediate scale, which is called the “mesomodel” [7–12]. It is fine enough to take into account all damage mechanisms but without generating huge calculation cost.

The organic matrix composites reinforced with carbon fibers (CFRP) are currently considered for long-term applications on civil aircrafts in the zone of the engine where the temperature condition is from 150 °C to 250 °C. High temperatures accelerate the oxygen diffusion and the oxidation reaction with the matrix of CFRP, which is called the oxidation aging. The variations of the material properties due to the oxidation aging may damage the composite materials and lead to a dramatic decrease of the material lifetime after long-term aging. Therefore the behavior of an oxidized laminated composite is an essential phenomenon to understand. Previous studies have shown that the oxidation aging leads an increase of the Young’s modulus [13, 14] and shrinkage [15–17] of the polymer resin. Other studies at the micro-scale showed that the oxidation aging may damage the fiber/matrix interface [18]. However, some problems still exist to describe the mechanical behavior of the aged samples at the scale of composite plies.

The object of this thesis is to model the behavior of laminated composites under extreme environmental conditions by extending the mesoscale modeling strategy developed at the LMT-Cachan. A part of this work is carried out within the research program “COMPTINN” of world competitiveness cluster “Aerospace Vallée” composed by EADS, SAFRAN, Airbus and university laboratories including the LMT-Cachan.

The oxidation aging of composite materials is a complex phenomenon composed of several effects on material properties and on structural behaviors at different scales. A preliminary study devoted to the bibliographical research and experimental observations provides an overview of oxidation aging effects on neat resin and on composite materials. Given the complexity of the oxidation aging, both experimental studies and modeling studies are performed to understand and to identify individually different effects at different scales. Since the behavior of the oxidized samples results from the

oxidation reaction of the polymer matrix, studies were firstly realized at the fiber/matrix scale. A model at this scale is introduced to describe the behavior of composite materials integrating two effects of the oxidation aging on the matrix, which are the increase of the Young's modulus and the shrinkage. The meso-scale properties of the oxidized composite material can be obtained by homogenizing the micro-scale information provided by the fiber/matrix scale model. On the other side, the meso-scale tests are performed in order to understand the effect of the oxidation aging on the mechanical behavior of composite plies. Tensile tests are performed on unaged and aged $[90/0]_s$ samples to characterize the crack density evolution for different oxidation times and vibration tests are performed on the same specimens to gather information on the elastic properties of the oxidized layer. In order to represent the phenomena observed from tests, the cracking behavior of the oxidized laminated composites is simulated with the characterized properties at the micro-scale, in which a composite ply is considered as a homogenous material but damage mechanisms (cracks) are described discretely. Based on the results of the micro-scale studies, a meso-scale model is proposed to predict the crack density evolution of an aged composite ply. The proposed model takes into account the increase of the matrix elastic modulus and the shrinkage associated with the oxidation aging, but does not consider possible weakening effects of the oxidation aging due to the lack of available information. Therefore, a new test is developed based on the standard climbing drum test (ASTM D1781-98 [20]) to study the interlaminar fracture criterion for oxidized composites.

The first chapter presents the background of this research. In particular, it introduces the mesomodel of LMT-Cachan for unaged composite materials and discusses previous studies on the propagations and effects of the oxidation aging on neat resin and composite materials, which gives us the general idea to study the oxidation aging from the microscale to the mesoscale.

The second chapter presents the effort that we have put in the search of an oxidation indicator. At the mesoscale, the oxidation aging is generally a local phenomenon and is limited in the oxidized zone due to the coupled effect between the oxygen diffusion and the oxidation reaction, which requires an indicator to distinguish the oxidized part from the rest of the specimen. The oxidized/damaged zone lighted under the dark field mode of microscopy has been chosen to be the indicator. It allowed us to confirm the anisotropic diffusion of oxygen. A structural phenomenon that is cracks crossing partially the 90° ply was also observed.

The third chapter is devoted to the characterization of the meso-scale properties of the oxidized composite material. The effects of oxidation aging on the matrix referenced from literature or identified experimentally by project partners are introduced in a micro-scale model to obtain the mesoscale properties of the oxidized composite materials via a homogenization method. The elastic modulus and shrinkage of the aged composite material are showed to vary with the variation of the matrix and modeled as functions of the oxidation levels.

The fourth chapter presents the tests that have been carried out on the unaged and aged $[90/0]_s$ samples. Tensile test allowed to detect cracks crossing the entire outer plies by digital image correlation (DIC). Results showed that the oxidation aging advanced the propagation of cracks and resulted in a higher crack density at the same applied strain. We measured also the first natural frequencies from non-destructive vibration tests. They provided information of the stiffness of the oxidized layer and showed that the effective modulus of oxidized composite material results from the balance between the increase of the elastic modulus and the damages generated by the oxidation induced shrinkage.

The fifth chapter presents the efforts towards a mesoscale modeling of the transverse cracking of the oxidized composites. In order to simplify the meso-scale modeling, a homogeneous oxidized layer is introduced based on the oxidized zone obtained from a diffusion/reaction model [15]. The structure of an oxidized ply is described as two related layers, the homogeneous oxidized layer and the non-oxidized layer. The cracking behavior of the oxidized laminated composites was studied at the micro-scale with the above structure. The properties of the aged composite materials characterized in the third chapter are integrated into the micro-scale periodic models of laminated composites to calculate the strain energy release rates (G). Results explained the existence of cracks crossing partially the 90° ply by comparing G of cracks of different lengths. The tensile tests on aged $[90/0]_s$ samples were also simulated by the micro-scale incremental studies which take into account several scenarios. At last, a mesoscale model is proposed to predict the evolutions of aged samples based on the micro-scale simulations taking into account the competition between partial cracks and the classical cracks which cross the entire ply.

The sixth chapter is devoted to the study of the interlaminar fracture behavior of the oxidized laminated composites. A new test was developed in LMT-Cachan based on the standard test (ASTM D1781-98 [20]) the climbing drum peel test to study the coupled effect of the oxygen diffusion, the oxidation reaction and the modification of the interlaminar fracture criteria of laminated composite. The proposed test is based on the propagation of the mode I interlaminar delamination under a constant mechanical loading. The crack propagation is driven by the oxidation aging. By modifying the available energy levels, different speeds of delamination propagation are measured. These velocities provide an information to relate the oxidation level to the reduced critical strain energy release rate.

Finally, a conclusion summarizes the work that has been done in this thesis on the effects of the oxidation aging on the material properties and structural behavior of laminated composites. Difficulties existing in the tests or the modeling are summarized and some possible extensions of the current model are proposed as perspectives.

Chapter 1

Background

Contents

1.1	Introduction	6
1.2	The mesomodel of LMT-Cachan	6
1.2.1	Damage model for the ply	7
1.2.2	Damage model for the interface	11
1.3	Oxidation aging on neat resin	12
1.3.1	The diffusion/reaction process	13
1.3.2	Effects of the oxidation aging	15
1.3.3	Coupling between oxidation and damage	17
1.4	Modeling of the oxidation aging on neat resin	18
1.4.1	General model of the diffusion/reaction process	18
1.4.2	Models of the oxidation reaction	19
1.4.3	Models of the effects of the oxidation aging	22
1.5	Oxidation aging on composite material	25
1.5.1	The anisotropic propagation of the oxidation aging on a composite ply	25
1.5.2	Effects of the oxidation aging on composite materials	29
1.5.3	Damages and fractures of oxidized composite materials	31
1.6	Modeling of the oxidation aging on composite materials	32
1.6.1	Microscale models of the oxidation aging on composite materials	32
1.6.2	Mesoscale model of the anisotropic propagation	34
1.7	Conclusion	35

1.1 Introduction

In this thesis, we are interested particularly in the carbon fibers reinforced polymer material (CFRP). Due to the structure of the laminated composites, several types of damage mechanisms present in the behavior of laminated composites. For about 30 years, the LMT-Cachan has developed a model to predict the behavior and the fracture of laminated composites [4–8,11] at the mesoscale where the composite plies are modeled as damageable and anelastic continua.

The applications of composite materials face now more complicated environmental conditions. Therefore, the mesomodel is also required to take into account those environmental loadings, for example the oxidation aging at relatively high temperatures ($150\text{ }^{\circ}\text{C} \sim 250\text{ }^{\circ}\text{C}$). Experimental investigations have shown that the oxidative environment reduce significantly the resistance of composite materials to mechanical [21] or thermal [22] loadings. The behavior of the oxidized composite materials becomes an essential problem to understand. Many works have been performed to study the problem at the microscale, which is also the fiber/matrix scale. At the temperatures considered here, carbon fibers are found to be chemically inert to the oxidative environment. But the organic matrix reacts with the oxygen [23] leading to weight loss [24,25], shrinkage [15–17] and an increase of elastic modulus [26–28]. The above effects on the oxidized matrix may lead to the fiber/matrix interface debonding [18]. Approaches have been proposed to model and to predict the micro-scale behavior of the oxidized composite material [17,18]. But, a better understanding on the behavior of an oxidized composite ply seems to be still missing to relate the effects of the oxidation aging at the microscale to the macro-scale reduced performance.

1.2 The mesomodel of LMT-Cachan

The mesomodel of LMT-Cachan considers that a laminated composite is composed of two basic components, the ply and the interface. Damage mechanisms in the model are described in the framework of the mechanics of continuous media. They are also considered homogeneous throughout a composite ply. In the enhanced version of the mesomodel, four damage mechanisms are taken into account which are the fiber/matrix debonding, the transverse cracking, the fiber breakage and the interlaminar delamination. The former three mechanisms are considered to be located in plies and the latter one is considered to be the mechanism of interfaces. The mesomodel is recalled here following [11].

1.2.1 Damage model for the ply

The strain energy density of a ply is defined as

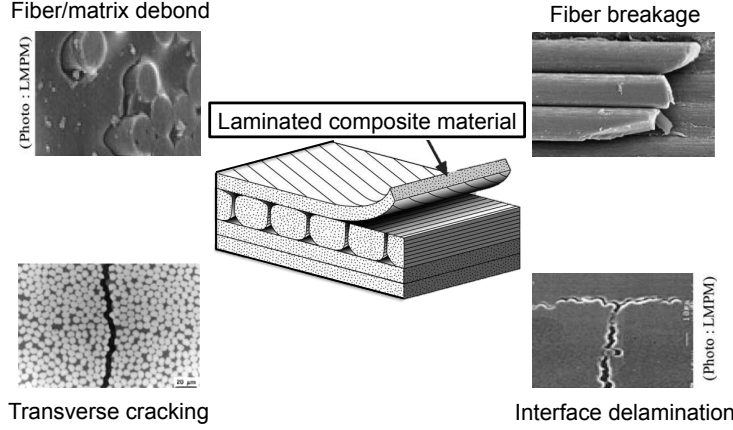


Figure 1.1: The damage mechanisms in laminated composites [29]

$$e_d = \frac{1}{2} \begin{bmatrix} \sigma_{11} \\ \sigma_{22} \\ \sigma_{33} \end{bmatrix}^t \begin{bmatrix} \frac{1}{E_1^0(1-d_f)} & -\frac{\nu_{12}^0}{E_1^0} & -\frac{\nu_{13}^0}{E_1^0} \\ -\frac{\nu_{12}^0}{E_1^0} & \frac{1}{E_2^0(1-[\sigma_{22}]^+ + \bar{d}_{22})(1-[\sigma_{22}]^+ d')} & -\frac{\nu_{23}^0}{E_2^0(1-[\sigma_{22}]^+ + \bar{d}_{22})} \\ -\frac{\nu_{13}^0}{E_1^0} & -\frac{\nu_{23}^0}{E_2^0(1-[\sigma_{22}]^+ + \bar{d}_{22})} & \frac{1}{E_3^0(1-[\sigma_{33}]^+ d')} \end{bmatrix} \begin{bmatrix} \sigma_{11} \\ \sigma_{22} \\ \sigma_{33} \end{bmatrix} \quad (1.1)$$

$$+ \frac{\sigma_{12}^2}{2G_{12}^0(1-\bar{d}_{12})(1-d)} + \frac{\sigma_{13}^2}{2G_{13}^0(1-d)} + \frac{\sigma_{23}^2}{2G_{23}^0(1-\bar{d}_{23})(1-d_{23})}$$

where d , d' , d_{23} are the damage variables representing the diffuse damage, \bar{d}_{12} , \bar{d}_{22} , \bar{d}_{23} are the damage variables representing the transverse cracking, d_f is the damage variable representing the fiber breakage, the symbol $[\bullet]^+$ denote the Heaviside function of \bullet . For each damage mechanism, the evolution laws are defined based on the definition of the conjugate thermodynamic force.

$$Y_{d_i} = \left\langle \left\langle \frac{\partial e_d}{\partial d_i} \right\rangle \right\rangle \quad (1.2)$$

where $\langle \langle \bullet \rangle \rangle$ denotes the mean value through the ply thickness, d_i denotes each damage variable. Furthermore, in order to limit the localization phenomenon during the calculation, the evolution laws of the damage variables are defined with a delay effect [30, 31]

$$\dot{d}_i = \frac{1}{\tau_c} \left(1 - e^{(-a[\langle w - d_i \rangle_+])} \right) \quad (1.3)$$

where $\langle \bullet \rangle_+$ denotes the positive part of \bullet , τ_c is characteristic time which limits the velocity of damage propagation, a is a material parameter, w are functions of the thermodynamic force.

1.2.1.1 Diffuse damage

The diffuse damage represents the damage induced by the fiber/matrix debonding which propagates under shear loads or transverse tensile loads. The variable w is defined as

$$w = \frac{\langle \sqrt{Y_d + b_2 Y_{d'}} - \sqrt{Y_0} \rangle_+}{\sqrt{Y_c} - \sqrt{Y_0}} \quad (1.4)$$

where b_2 , Y_0 , Y_c are material parameters. The damage variables are defined as

$$\begin{aligned} \dot{d} &= \frac{1}{\tau_c} (1 - e^{(-a[(w-d)+])}); \quad d \leq d_s \\ d' &= b_3 d \\ d_{23} &= 1 - \frac{1 - d'}{1 - \frac{\nu_{23}^0}{1 + \nu_{23}^0} d'} \end{aligned} \quad (1.5)$$

where d_s represents a maximum value of the diffuse damage, b_3 is a material parameter.

1.2.1.2 Transverse cracking damage

Transverse cracks in the mesomodel are defined to cross the entire thickness of a ply. To model the damage associated to transverse cracking at the mesoscale, a micro-scale parameter, the crack density (ρ), is introduced defined as

$$\rho = \frac{h}{D} = \frac{h}{\frac{L}{N}} \quad (1.6)$$

where h is the thickness of a ply, D is the average distance between two cracks, L is the length of the sample, N is the number of cracks laid along the length of the sample. Since the mesomodel consider a composite ply as a continuum structure, the energy released by cracks is represented by the meso-scale damage variables which are defined as functions of the micro-scale parameter ρ [8–10].

$$\bar{d}_{22} = f_{22}(\rho), \quad \bar{d}_{12} = f_{12}(\rho), \quad \bar{d}_{23} = f_{23}(\rho), \quad (1.7)$$

Furthermore, a previous study [19] has shown that transverse cracks initiate from the free edge when the stress reaches a criterion, however propagate crossing the width of the ply when the strain energy release rate reaches a criterion. Transverse cracking thus

behaves in two modes depending on the thickness of the ply. For thin plies, a crack may initiate but without crossing the entire width of the ply until enough energy is stored. For thick plies, enough energy usually has been stored before the stress reaches the critical value, the propagation of a crack is thus simultaneous to the initiation. It can be concluded that the transverse cracking phenomenon is driven by the energy for thin plies and by the stress for thick plies. In the mesomodel, a thickness h_c is introduced in the calculation of the thermodynamic force to represent the cracking driven by the critical stress in thick plies no matter the real thickness of the ply.

$$\bar{Y}_{d_i} = \min(h, h_c) \left\langle \left\langle \frac{\partial e_d}{\partial \bar{d}_i} \right\rangle \right\rangle \quad (1.8)$$

The variable w is defined as

$$w = g \left\{ [(\gamma_I Y_{22})^\alpha + (\gamma_{II} Y_{12})^\alpha + (\gamma_{III} Y_{23})^\alpha]^\frac{1}{\alpha} \right\} \quad (1.9)$$

where

$$g : x \rightarrow \frac{\partial \bar{d}_{22}}{\partial \rho}^{-1} \left(\frac{1}{x} \right), \quad (1.10)$$

$$\gamma_I = \frac{1}{G_I^c (1-d')}, \quad \gamma_{II} = \frac{\frac{\partial \bar{d}_{12}}{\partial \rho}}{\frac{\partial \bar{d}_{22}}{\partial \rho} G_{II}^c (1-d)}, \quad \gamma_{III} = \frac{\frac{\partial \bar{d}_{23}}{\partial \rho}}{\frac{\partial \bar{d}_{22}}{\partial \rho} G_{III}^c (1-d_{23})}$$

And the crack density is obtained as

$$\dot{\rho} = \frac{1}{\tau_c} \left(1 - e^{-a[(w-\rho)+]} \right); \quad \rho \leq \rho_s \quad (1.11)$$

where ρ_s is the saturation state of the crack density.

The cracking phenomenon on the oxidized composite material will be investigated in this thesis. Unlike the transverse cracking in the unaged composite materials, not all of the cracks on the aged composite material cross the thickness of the ply. It is not reasonable to relate all the cracks no matter their lengths with the thermodynamic force of the entire ply, which becomes one of the difficulties that we have faced.

1.2.1.3 Fiber breakage damage

The fiber breakage is a fragile phenomenon. In traction, it depends only on the tensile loading.

$$w = \begin{cases} 0 & \text{if } \frac{Y_{d_f}}{Y_{d_f}^T} < 1 \\ \frac{Y_{d_f}}{Y_{d_f}^T} & \text{if } \frac{Y_{d_f}}{Y_{d_f}^T} \geq 1 \end{cases} \quad (1.12)$$

In compressions, it depends also on the shear stress.

$$w = \begin{cases} 0 & \text{if } \frac{Y_{d_f}}{Y_{d_f}^C} + k \frac{Y_d}{Y_c} < 1 \\ \frac{Y_{d_f}}{Y_{d_f}^C} + k \frac{Y_d}{Y_c} & \text{if } \frac{Y_{d_f}}{Y_{d_f}^C} + k \frac{Y_d}{Y_c} \geq 1 \end{cases} \quad (1.13)$$

where $Y_{d_f}^T$, $Y_{d_f}^C$ are the thresholds of the thermodynamic force for traction and compression. k is a material parameter which allows to take into account the coupling with the shear stress. The damage variable d_f is defined as

$$\dot{d}_f = \frac{1}{\tau_c} (1 - e^{(-a[(w-d_f)+])}); \quad d_f \leq 1 \quad (1.14)$$

1.2.1.4 Inelasticity

In the direction of fibers, loads are supported by the rigid carbon fibers. But in the direction transverse to the fibers, the fiber/matrix debonding generates the friction in the interface, which leads to an inelastic deformation at the mesoscale. A plasticity model is thus introduced in the transverse direction of a composite ply and related to the diffuse damage. The effective stress is defined as

$$\tilde{\sigma}^t = \left[\sigma_{11} \quad \frac{\sigma_{22}}{1 - [\sigma_{22}]^+ d'} \quad \frac{\sigma_{33}}{1 - [\sigma_{33}]^+ d'} \quad \frac{\sigma_{12}}{1 - d} \quad \frac{\sigma_{13}}{1 - d} \quad \frac{\sigma_{23}}{1 - d_{23}} \right] \quad (1.15)$$

The yield function is defined as

$$f(\tilde{\sigma}, p) = \sqrt{\tilde{\sigma}_{12}^2 + \tilde{\sigma}_{13}^2 + \tilde{\sigma}_{23}^2 + a^2(\tilde{\sigma}_{22}^2 + \tilde{\sigma}_{33}^2)} - R(p) - R_0 \quad (1.16)$$

where a is a coupling parameter, R_0 is the threshold stress, $R(p)$ is the hardening function defined as $R(p) = Kp^M$.

The yield conditions are

$$\dot{\lambda} f = 0, \quad \dot{\lambda} \geq 0, \quad f \leq 0 \quad (1.17)$$

$$\dot{\tilde{\epsilon}} = \dot{\lambda} \frac{\partial f}{\partial \tilde{\sigma}} \quad \text{and} \quad \dot{p} = \dot{\lambda} \frac{\partial f}{\partial R} \quad (1.18)$$

1.2.2 Damage model for the interface

The interlaminar zone is modeled as a bidimensional structure to transfer stresses and displacements from one ply to another. Only one type of damage mechanism, the

interlaminar delamination, is taken into account in the model of the interface. The local coordinates of the interfaces depend on the direction of the adjacent plies. The strain energy density is defined as

$$e_{d,int} = \frac{1}{2} \begin{bmatrix} \sigma_{33} \\ \sigma_{13} \\ \sigma_{23} \end{bmatrix}^t \begin{bmatrix} \frac{1}{K_3^0(1-[\sigma_{33}]^+d_I)} & 0 & 0 \\ 0 & \frac{1}{K_1^0(1-d_{II})} & 0 \\ 0 & 0 & \frac{1}{K_2^0(1-d_{III})} \end{bmatrix} \begin{bmatrix} \sigma_{33} \\ \sigma_{13} \\ \sigma_{23} \end{bmatrix} \quad (1.19)$$

where

$$K_1^0 = \frac{2G_{13}}{e}, \quad K_2^0 = \frac{2G_{23}}{e}, \quad K_3^0 = \frac{E_3}{e}, \quad (1.20)$$

G_{13}, G_{23}, E_3 are the elastic properties of the matrix, e is the thickness of the interface zone which is very small compared with the in-plane dimension, d_I, d_{II}, d_{III} are the damage variables of the interlaminar delamination.

The variable w is defined as

$$w = \left(\frac{n}{n+1} \frac{\langle [Y_I^{\alpha_{int}} + (\gamma_{II,int} Y_{II})^{\alpha_{int}} + (\gamma_{III,int} Y_{III})^{\alpha_{int}}]^{\frac{1}{\alpha_{int}}} - Y_{0,int} \rangle_+}{Y_{c,int} - Y_{0,int}} \right)^n \quad (1.21)$$

where $Y_{0,int}, \alpha_{int}, n$ are the material parameters of the interface,

$$Y_{c,int} = G_{I,int}^c, \quad \gamma_{II,int} = \frac{G_{I,int}^c}{G_{II,int}^c}, \quad \gamma_{III,int} = \frac{G_{I,int}^c}{G_{III,int}^c} \quad (1.22)$$

$G_{I,int}, G_{II,int}, G_{III,int}$ are the energy release rates of the three modes of delaminations.

The delamination generated at the crack tips by the transverse cracking in the adjacent plies are taken into account. The damage variables of the interface delamination are related additionally to the mean crack density of the adjacent plies $\bar{\rho}$

$$\begin{aligned} \dot{d}_I &= \frac{1}{\tau_c} (1 - e^{(-a[(w-d_I)^+])}); \quad \bar{\rho} \leq \rho_s \\ d_{II} &= d_I + (1 - d_I) 2a_{int} \bar{\rho} \sin^2 \left(\frac{\theta}{2} \right) \\ d_{III} &= d_I + (1 - d_I) 2a_{int} \bar{\rho} \cos^2 \left(\frac{\theta}{2} \right) \end{aligned} \quad (1.23)$$

When the $\bar{\rho}$ reaches to the saturation state, the interface is considered to be locally delaminated.

$$d_I = d_{II} = d_{III} = 1 \quad \bar{\rho} = \rho_s \quad (1.24)$$

In the enhanced version of the interface model [36], the delamination induced by the transverse cracking is modeled as functions of the crack densities respectively in the two adjacent plies instead of the average of the two, which allows the model to be applied in more general situations.

The mesomodel of LMT-Cachan has been implanted into several commercial tools. Its predictions have been validated even in some critical examples under mechanical loadings [32]. Modifications performed by Hochard et al. [33] allow to extend its application to woven composites.

Composite materials face now more severe environmental conditions such as the oxidation aging at relatively high temperatures ($150\text{ }^\circ\text{C} \sim 250\text{ }^\circ\text{C}$). As it will be presented in the following sections, the oxidation aging on the composite material is a local phenomenon and non-homogeneous throughout the oxidized ply. It is quite different from the classical mesomodel which considers the mechanisms to be homogeneous through a ply. The aim of this thesis is to extend to the mesomodel to describe the behavior of a laminated composite taking into account the effects of the oxidation aging.

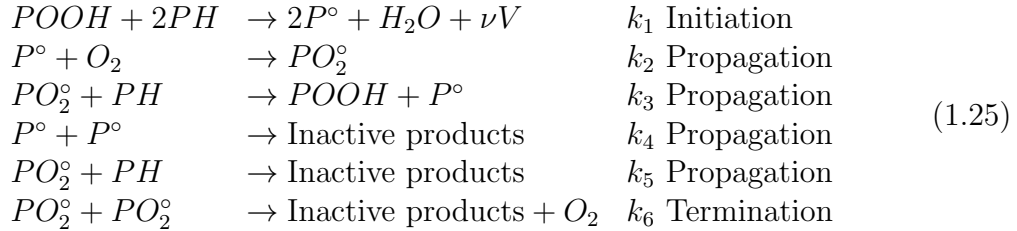
1.3 Oxidation aging on neat resin

At relatively high temperatures ($150\text{ }^\circ\text{C} \sim 250\text{ }^\circ\text{C}$), oxygen diffuses into the neat resin and reacts with it, which leads the oxidation aging to be limited within a certain distance from the exposed surface [23, 37–39]. Within the oxidized layer of the resin, the variation of the chemical composition generates various effects including weight loss [23–25], shrinkage [15–17] and an increase of the elastic modulus [26–28]. Some approaches have been developed to model the diffusion/reaction process of the oxidation propagation on the neat resin [23, 45]. Based on the diffusion/reaction models, the oxidation effects are usually related to a parameter which represents the oxidation level [14, 16, 17, 26].

1.3.1 The diffusion/reaction process

The oxidation aging is a combined process of the oxygen diffusion and the oxidation reactions. Oxygen diffuses into neat resin and changes the chemical composition of the polymer by a series of chemical reactions whose mechanistic scheme has been firstly established in the 1940s [34] and modified depending on materials and on aging condi-

tions since then [23, 35]. The following equations give an example of the mechanistic scheme [23].



where $[POOH]$ is the hydroperoxides, $[P^\circ]$ is the free radical site, $[PO_2^\circ]$ is the grafted radical, $[PH]$ is the oxidizable site. The variation of the chemical composition of the resin can be analyzed experimentally, for example the quantum yield of carbonyl with IR spectrophotometry [23, 37].

The coupling between the oxygen diffusion and the oxidation reactions leads the propagation of the oxidation aging to tend to an asymptotical thickness. On the exposed surface of the resin, the oxidation aging is dominated by the oxidation reactions because sufficient oxygen could be provided by the environment. Due to the oxygen consumption, less and less oxygen diffuses into the deeper zone and reacts with the polymer. The oxidation aging on neat resin is thus limited within a certain distance and becomes a local and non-homogeneous phenomenon.

The oxidized layer on neat resin can be detected with numerous techniques [35]. Optical indicators are usually used in mechanical studies [23, 38, 39]. The color of resin is one of the simplest indicators [23, 38]. Due to the variation of the chemical composition, the color of the resin turns from light to dark after aging (Fig. 1.2(a)). Another indicator is the elevations of the polished surface [23]. The resin weakened by the oxidation aging shows a rough surface after polishing, which is considered as an oxidized/damaged zone. It can be observed with special microscopies such as the dark field illumination or the differential interference contrast microscopy (Fig. 1.2(b)).

Two examples of the evolution of the oxidized layer reported in the literature are shown in the following.

By monitoring the optical indicators (Fig. 1.2(b)), Colin [23] has evaluated the propagation of the oxidized layer (*Criterion 2*) and of the oxidized/damaged layer (*Criterion 1*) for an epoxy resin (Fig. 1.2(b)). Thicknesses of both the layers increase sharply at the beginning of the aging, then tend to an asymptotic value (Fig. 1.3).

Tandon et al. [39] observed the oxidized PRM-15 resin with classical microscopy. Three zones were observed (Fig. 1.4(a)) which are the oxidation layer, the transition region and the unoxidized core. The propagation of the oxidation aging is obtained by measuring the thickness of the zones (Fig. 1.4(b)). The thickness of the transition region is almost constant whereas the thickness of the oxidation layer seems to approach

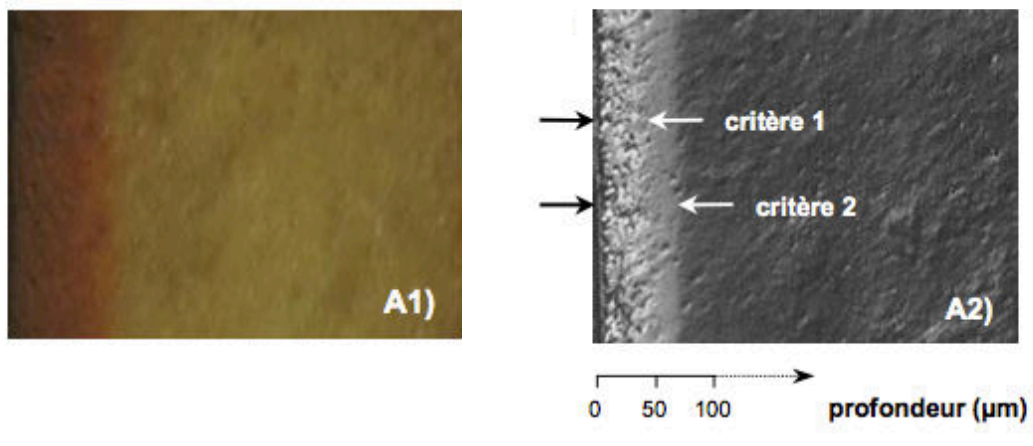


Figure 1.2: Microscopic observation under lightfield illumination (A1) and differential interference contrast observation (A2) of a polished section of an epoxy resin aged for 200 h at 240 °C in the air [23]

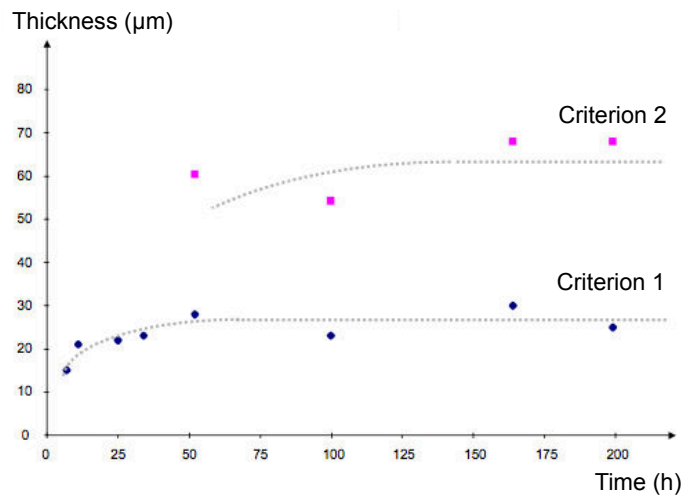


Figure 1.3: Evolution of the thickness of the oxidized layers according to the two criteria on an epoxy resin aged at 240 °C in the air [23]

an asymptotical value after the long-term aging.

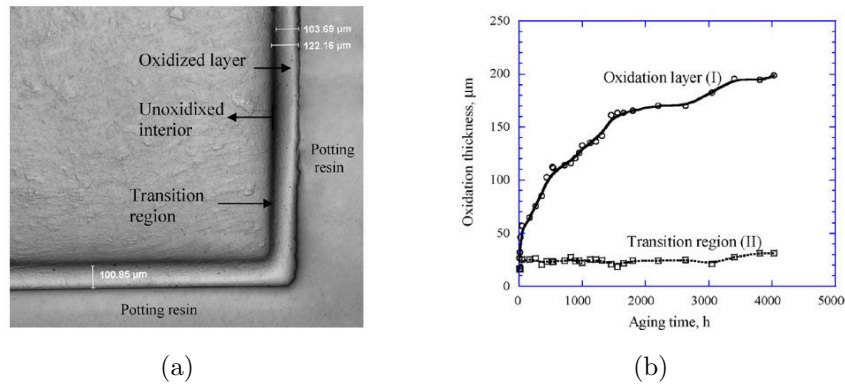


Figure 1.4: (a) Photomicrograph of PMR-15 resin aged at 288 $^{\circ}\text{C}$ in the air (b) Thicknesses of the oxidation layer and of the transition region versus the aging time. [39]

1.3.2 Effects of the oxidation aging

Aged resin, on one hand, loses weight because chemical segments liberated by chain scission depart as volatile products [23–25, 40]. In practice, the weight loss, which depends on the temperature and on the oxygen concentration (Fig. 1.5), is usually studied with thermogravimetric tests [23–25, 40]. The results of the thermogravimetric test are either used as an important indicator of the material stability [25] or to identify parameters of the oxidation reaction process [23].

Aged resin, on the other hand, gains molecular density by the oxygen grafting [23]. The decreased mass and the increased density result in shrinkage of the oxidized resin. Pochiraju and al. [17] has compared the shrinkage of the PMR-15 resin in the oxidative environment and the non-oxidative environment. The oxidation induced shrinkage is measured from the volume change assuming that there is no erosion loss at the surface of the resin. Decelle et al. [16] have measured the shrinkage of thin epoxy resin films (70 μm) with a high resolution microscope (0.01 μm) (Fig. 1.6(b)). As the films are very thin, it can be considered that the oxidation aging and the volume variation is homogeneous in the resin. Shrinkage tends to an asymptotical value, which indicates that the oxidation process slows down with the consumption of polymer.

Furthermore, chain scissions decrease the activity of β transition of the oxidized resin (T_{β} in Fig. 1.7(a)) and thus lead to an increase of the elastic modulus at the ambient temperature, which is also called an antiplastic phenomenon [26–28]. Various techniques allow to measure the indentation elastic modulus at the ambient temperature, such as the atomic force microscope (AFM) [13] and the ultra-micro indentation (UMI) [14].

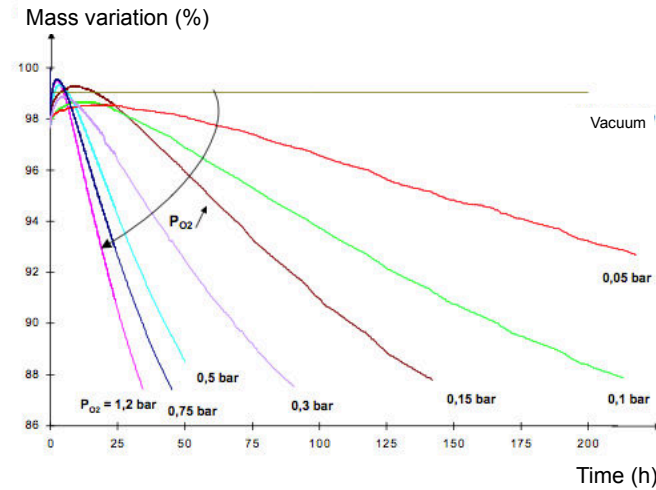


Figure 1.5: Mass variation of $50 \mu\text{m}$ thick bismaleimide resin aged in the environment of different oxygen pressure at $240 \text{ }^\circ\text{C}$ [23]

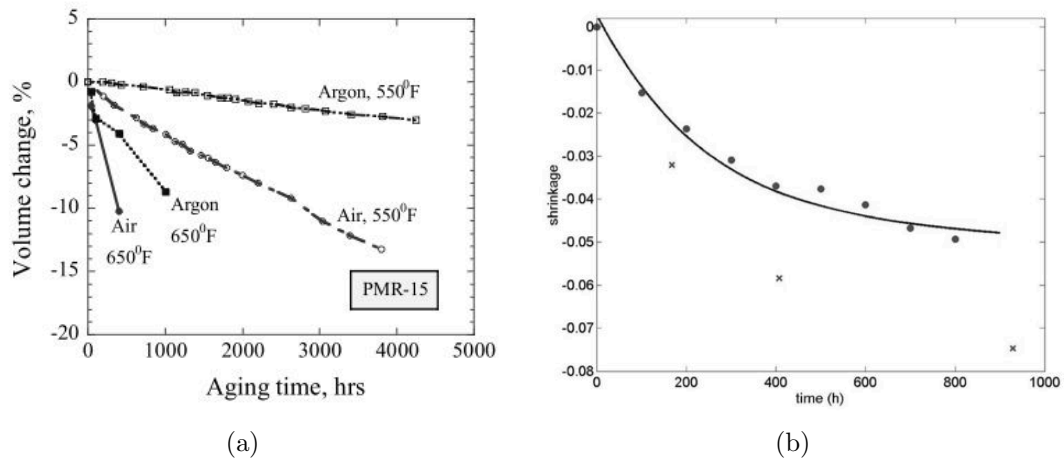


Figure 1.6: (a) Volume change of PMR-15 specimen in the air and in the argon [17] (b) Shrinkage of a $70 \mu\text{m}$ matrix film aged at $180 \text{ }^\circ\text{C}$ in the air [23]

All of these tests proposed a similar profile of the elastic indentation modulus for the section of aged resin. The elastic indentation modulus in the oxidized layer is higher than the unaged part as shown in Fig. 1.7(b).

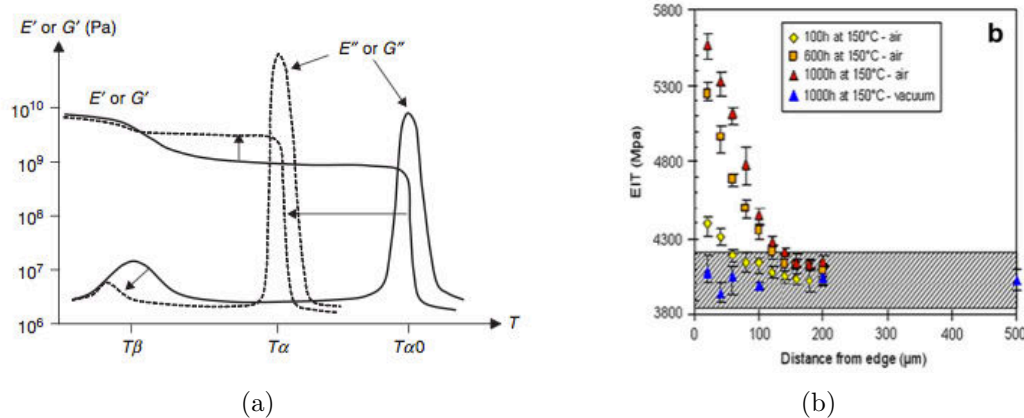


Figure 1.7: (a) Shape of dynamic mechanical analysis (DMA) curves for a network before (full line) and after aging (dashed line) [26] (b) Isothermal aging at 150 °C of epoxy resin specimens, the elastic indentation modulus versus the distance from the edge [14]

The mechanical properties of the oxidized resin are essential to be identified as they influence directly the the mechanical behavior of the neat resin and the composite material.

1.3.3 Coupling between oxidation and damage

The combination of the oxidation effects may result in damage mechanisms. The oxidation aging on neat resin generates an important stress field in the oxidized layer due to the different shrinkage between the outer oxidized layer and the inner unoxidized core. Cracks can be initiated from the oxidized layer (Fig. 1.8), at the meanwhile, provide new exposed surfaces which allows the oxygen to diffuse into the deeper zone around the crack tips. Pochiraju and co-workers [44] observed that cracks and oxygen diffusion may couple to accelerate each other and penetrate towards the core of the material. However, few further studies have been performed to explorer the phenomenon, which leads the understanding on the phenomenon to remain phenomenological. In this thesis, a similar mechanism, which is the cracks crossing the oxidized layer of a composite ply, will be further discussed.

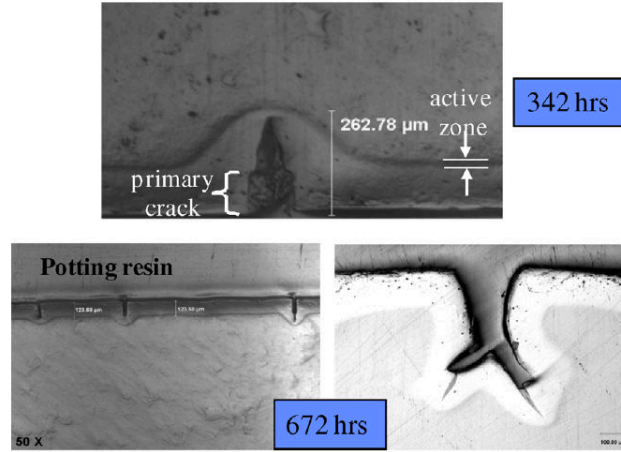


Figure 1.8: Oxidation layer growth (lighter regions) and damage evolution in neat PMR-15 resin at 343 °C [44]

1.4 Modeling of the oxidation aging on neat resin

1.4.1 General model of the diffusion/reaction process

Approaches [35,45,47] have been developed to model the propagation and the effects of the oxidation aging on neat resin. The diffusion/reaction process is usually described by an equation (Eq. 5.12) based on Fick's law.

$$\frac{\partial C}{\partial t} = D \frac{\partial^2 C}{\partial x^2} - R(C) \quad (1.26)$$

where x is the coordinate, D is the diffusivity, $R(C)$ is the oxygen consumption in the oxidation reaction, C is the oxygen concentration in resin varying between 0 and the oxygen concentration at the exposed surface (C_s) defined as

$$C_s = SP_{O_2} \quad (1.27)$$

where P_{O_2} is the partial pressure of the oxygen in the environment. The solubility (S) and the diffusivity (D) can be identified with permeability tests [23]. The diffusivity is a temperature dependent parameter described by the Arrhenius equation

$$D = D_0 \exp\left(-\frac{E_a}{RT}\right) \quad (1.28)$$

where D_0 is a coefficient, E_a is the activation energy, R is the universal gas constant (8.314 J/mol.K) and T is the temperature in the Kelvin scale.

1.4.2 Models of the oxidation reaction

1.4.2.1 Model of the temperature dependent reaction

McManus et al. [45, 46] expressed $R(C)$ with an Arrhenius-type approach

$$R(C) = R_0 k_0 \exp\left(-\frac{E_a}{RT}\right) (1-a)^n C^m \quad (1.29)$$

where R_0 is a constant factor fitted as 0.01 with tests on PMR-15 resin, $k_0 \exp\left(-\frac{E_a}{RT}\right)$ is the temperature dependent reaction rate in the form of Arrhenius equation, n and m are exponential factors, a is the local oxidation level varying between 0 and 1 which represent respectively the unoxidized state and the saturation of the oxidation aging defined as Eq. (1.30).

$$a = \frac{\rho_0 - \rho}{\rho_0 - \rho_d} \quad (1.30)$$

where ρ is the density of the oxidized resin, ρ_0 and ρ_d are the densities of the unoxidized resin and of the resin at the saturation state. They as well as n and m are identified from thermogravimetic tests on resin powder assuming that no volume change has occurred.

This phenomenological model describes the oxidation reaction with empirical exponential factors. It takes into account the temperature dependence of the oxidation reaction and allows to predict the profile of the oxygen concentration (C) (Fig. 1.9), the oxidation level (a) and the local density (ρ) in neat resin. However the application of this model is limited by the assumption that there is no volume change during aging, which is inconsistent with the experimental identifications [16, 17].

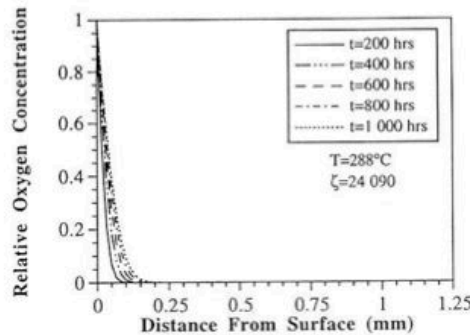


Figure 1.9: Relative oxygen concentration of PMR-15 resin exposed in the air at 288 °C [45]

1.4.2.2 Model based on the mechanistic schemes of the oxidation reaction

Another type of approach is developed based on the oxidation mechanistic schemes [35,47]. The oxidation reaction process is represented by a serie of nonlinear differential equations (Eq. (1.31)). The concentrations of the chemical sites can be obtained by resolving numerically the equations.

$$\begin{aligned}
R(C) &= -\frac{d[O_2]}{dt} = k_2C[P^\circ] - k_6[PO_2^\circ]^2 \\
\frac{d[POOH]}{dt} &= k_3[PH][PO_2^\circ] - k_1[POOH] \\
\frac{d[PH]}{dt} &= -k_0[PH] - 2k_1[POOH] - k_3[PH][PO_2^\circ] \\
\frac{d[PO_2^\circ]}{dt} &= k_2C[P^\circ] - k_3[PH][PO_2^\circ] - k_5[P^\circ][PO_2^\circ] - 2k_6[PO_2^\circ]^2 \\
\frac{d[P^\circ]}{dt} &= 2k_1[POOH] - k_2C[P^\circ] + k_3[PH][PO_2^\circ] - 2k_4[P^\circ]^2 - k_5[P^\circ][PO_2^\circ]
\end{aligned} \tag{1.31}$$

where $k_{1,\dots,6}$ are the reaction rates. Some parameters are determined from the theoretical structure of the polymer network ($[PH]_0$) or from structure/property relationships established for model compounds (k_2, k_3), others are identified using an inverse method from the experimental weight loss [15] which is modeled as.

$$\frac{1}{m_0} \frac{dm}{dt} = \frac{32}{\rho_0} (R(C)) - \frac{18}{\rho_0} k_1[POOH] - \frac{vM_V}{\rho_0} k_1[POOH] \tag{1.32}$$

where $vM_V = \sum v_i V_i$, v_i and V_i are the yield and molar mass of every volatile species. The kinetic diffusion/reaction model allows to predict the profiles of kinetic parameters such as the weight loss and the oxygen concentration (Fig. 1.10).

The model based on the chemical mechanistic scheme contains less empiric parameters. However the differential equation group can not be resolved analytically. A simplified approach is proposed assuming low conversion ratios, that is considering that the consumption of the polymer is negligible compared with its initial total quantity ($[PH] \approx [PH]_0$). $R(C)$ is simplified as

$$R(C) = 2R_0 \frac{\beta C}{1 + \beta C} \left[1 - \frac{\beta C}{2(1 + \beta C)} \right] \tag{1.33}$$

where β is a coefficient as a function of the reaction rates

$$\beta = \frac{k_2 k_6}{2k_5 k_3 [PH]} \tag{1.34}$$

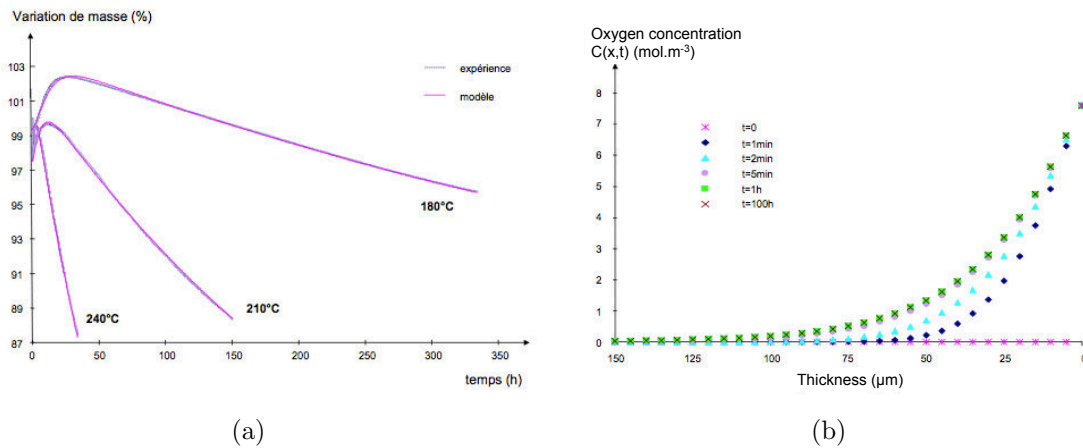


Figure 1.10: (a) Mass variation of $50 \mu\text{m}$ thick bismaleimide resin aged in 1.2 bar oxygen at different temperatures (b) Oxygen concentration profile of bismaleimide aged for different times at 240° [23]

Since $[PH]$ is assumed to be invariable, β becomes a constant. After the oxygen concentration reaching the stationary state, polymer reacts at a constant rate without the deceleration due to the polymer consumption. The simplified model overestimates the oxidation process compared with the reality. Taking the weight lose as an example, the overestimation of the prediction can be negligible in the short-time aging on some materials (Fig. 1.11(a)), while can not in others cases (Fig. 1.11(b)) depending strongly on the chemical composition of the materials and the aging conditions.

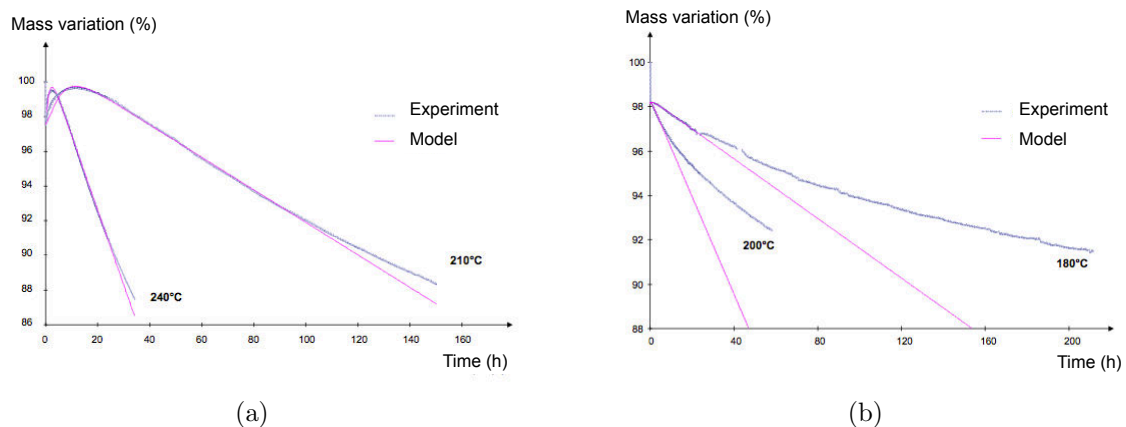


Figure 1.11: Mass variation of $50 \mu\text{m}$ thick resin aged at different temperatures [23] (a) Bismaleimide in 1.2 bar oxygen (b) Epoxy in 1 bar oxygen

Given this defect, Pochiraju and co-workers [50] introduce additionally a saturation level of the oxidation aging into the simplified model to limit the oxidation aging (Eq. (1.35)).

$$R(C) = \begin{cases} 2R_0 \frac{\beta C}{1+\beta C} (1 - \frac{\beta C}{2(1+\beta C)}) & \text{for } \phi < \phi_{ox} \\ 0 & \text{for } \phi = \phi_{ox} \end{cases} \quad (1.35)$$

$$\text{with } \frac{d\phi}{dt} = -\alpha R(C) \quad (1.36)$$

where ϕ represents the oxidation level which varies between 1 et ϕ_{ox} corresponding respectively to the unoxidized state and to the saturation state of the oxidation reaction, α is the proportionality factor. ϕ_{ox} and α can be determined from thermogravitic tests. In this thesis, the simplified model, which contains the assumption of the low conversion ratios, is also chosen to describe the diffusion/reaction process due to the simplicity of the resolution.

1.4.3 Models of the effects of the oxidation aging

Based on the kinetic diffusion/reaction model and its simplified version, various approaches have been developed to model the effects of the oxidation aging on neat resin.

The shrinkage is one third of the volume variation because the shrinkage in pure polymer is isotropic [15].

$$\epsilon_o = \frac{1}{3} \frac{\Delta V}{V_0} = \frac{1}{3} \left(\frac{\Delta m}{m_0} - \frac{\Delta \rho}{\rho_0} \right) \quad (1.37)$$

with

$$\frac{\Delta \rho}{\rho} = \frac{k_2 M_{a0}}{\rho_0} \left(\frac{\Delta m}{m_0} - \frac{\Delta n}{n_0} \right) \quad (1.38)$$

where ρ_0 is the density of the unaged resin, $\frac{\Delta m}{m_0}$ is the weight loss obtained from the kinetic diffusion/reaction model, k_2 is a coefficient, M_{a0} is the average atomic mass of the unaged resin depending on the chemical composition, $\frac{\Delta n}{n_0}$ is the variation of the total atomic number calculated from the chemical composition of resin

The chain scissions of the oxidation ageing reduce the atom activity and result in a decrease of the glass transition temperature as it has been modeled by Colin et al. [26].

$$T_{g0} - T_g = K_{EF} S \quad (1.39)$$

where T_{g0} and T_g are the glass transition temperature of unaged and aged resin in the Kelvin scale, K_{EF} is a material constant, S is the number of chain scissions calculated from the mechanistic schemes of the oxidation aging. Using the glass transition

temperature, one may predict the strain rate dependent storage modulus [48] or the elastic indentation modulus as shown in the following equation [26].

$$E = E_0 \left(1 - \alpha \frac{T}{T_g} \right) - \Delta E \quad (1.40)$$

where ΔE is the drop of the elastic modulus, α is a coefficient, E_0 is the elastic modulus at the absolute zero, T is the environment temperature in the Kelvin scale.

Olivier et al. [14] modeled the elastic modulus (E) with another indicator of the oxidation levels. They related the elastic modulus identified experimentally to the concentration of the oxidation products (Q) predicted by the kinetic diffusion/reaction model (Fig. 1.12).

$$Q(C) = \int_0^t R(C) dt \quad (1.41)$$

They used a mathematical correlation to describe empirically the elastic modulus of a well studied epoxy resin. Gigliotti et al. [53] enhanced the model by relating also the Poisson's ratio to Q and taking into account the viscoelasticity of the resin. This modeling strategy, that relates the effects of the oxidation aging to the concentration of the oxidation products, is also used in our study. In this thesis, the elastic modulus and the shrinkage of the aged matrix or of the aged composite materials are modeled as functions of the relative concentration of the oxidation products also.

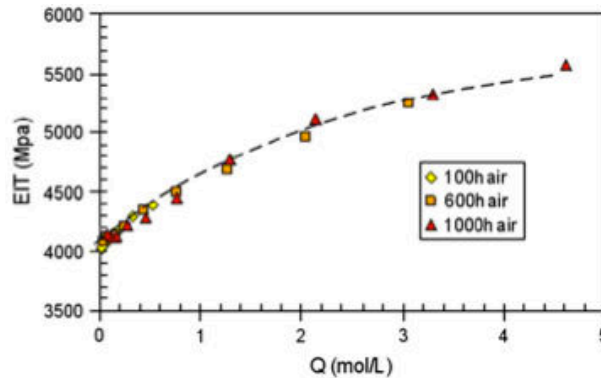


Figure 1.12: Correlation between the measured elastic indentation modulus (EIT) and the calculated concentration of the oxidation products (Q) [14]

Tandon et al. [17] describe the effects of the oxidation aging on the neat resin based on their observations. Due to the high reactivity and the low quantities of the oxidizable sites of PMR-15 resin, the polymer at the exposed surface of the sample is quickly consumed up and the oxidation aging continues at the transition zone. The oxidized PMR-15 resin is thus considered to be composed of three zones (Fig. 1.13) whose oxidation levels are represented by the parameter ϕ . The diffusivity [50, 51],

the shrinkage [17] and the elastic modulus [17] are all considered to be oxidation level dependent parameters. The diffusivity is defined as

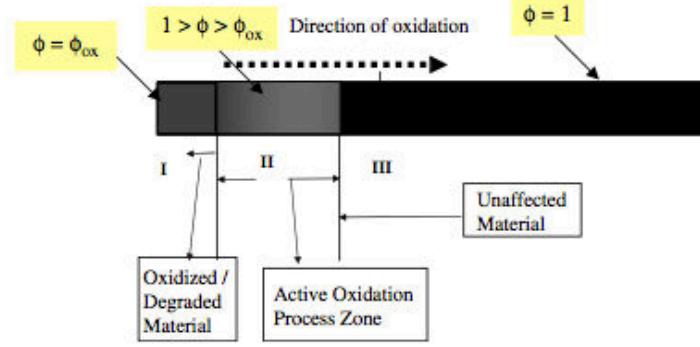


Figure 1.13: Schematic of the three zones in thermo-oxidation. [50, 51]

$$D(\phi) = D_{un} \frac{\phi - \phi_{ox}}{1 - \phi_{ox}} + D_{ox} \frac{1 - \phi}{1 - \phi_{ox}} \quad (1.42)$$

The local shrinkage of different oxidation levels (ϕ) are identified experimentally (Fig. 1.6) [17]. The elastic modulus is considered to depend on both temperatures and oxidation levels [17] stated as

$$E(\phi, T) = E_{un}(T) \exp\left(K_{ox} \frac{1 - \phi}{1 - \phi_{ox}}\right) \quad (1.43)$$

where $E_{un}(T)$ is the temperature dependent elastic modulus of unaged resin. K_{ox} is identified from nano-indentation tests.

1.5 Oxidation aging on composite material

Though carbon fibers are almost chemically stable at the studied temperature interval ($150\text{ }^{\circ}\text{C} \sim 250\text{ }^{\circ}\text{C}$), additional phenomena occur in composite material during oxidation aging due to the complexity of the material micro-structure. Experimental and numerical studies have been performed at different scales. At the fiber/matrix scale, shrinkage of the aged matrix generates an important stress field around fibers which may induce the fiber/matrix debonding [52–54]. The presence of the carbon fibers leads also the propagation of the oxidation aging at the scale of a composite ply to be anisotropic [23, 39, 52, 57]. At the scale of laminated composites, the oxidation aging has been proved to reduce the performance of samples [21, 63–65].

1.5.1 The anisotropic propagation of the oxidation aging on a composite ply

The propagation of the oxidation aging on the composite materials has been generally observed as an anisotropic phenomenon. For example, some researchers [39, 52] have observed the polished section of the unidirectional composite aged for different times (Fig. 1.14(a)). By measuring the thicknesses of the lighted zones under the dark field illumination microscopy, the propagation of the oxidized/damaged zone is monitored (Fig. 1.14(b)). The oxidized/damaged zone in the direction along the fibers grows much faster than in the direction transverse to the fibers.

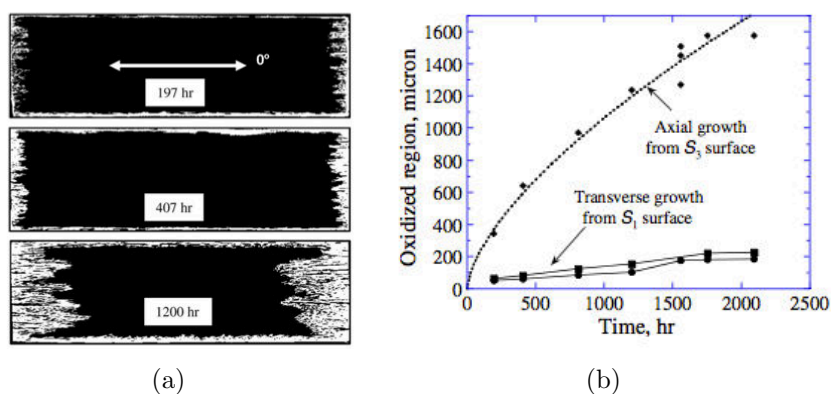


Figure 1.14: (a) Section of unidirectional G30-500/PMR-15 composite aged at 288 °C for different times. (b) Comparison of oxidation growth in the transverse and axial directions of unidirectional composites [52]

The anisotropic propagation results from several reasons. In the transverse direction of the composite material, inactive carbon fibers tend to delay the propagation of the oxidation aging compared with the propagation in the neat resin (Fig. 1.15).

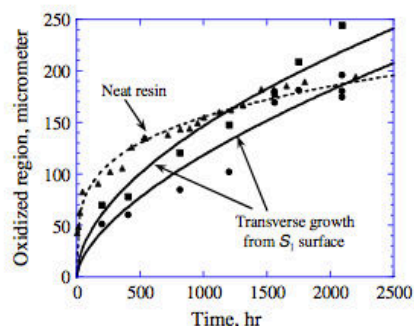


Figure 1.15: Comparison of oxidation growth in the transverse direction of composite and in the neat PMR-15 resin. [52]

In the axial direction of the composite materials, the fiber/matrix interface and the associated damage mechanisms accelerate the propagation of the oxidation aging along the direction of fibers. The oxidized matrix tends to shrink whereas the carbon fibers are almost unaffected by the oxidation aging. The different shrinkage between the fibers and the matrix leads to an important stress field and may generate the fiber/matrix debonding [52–54]. The shrinkage of the oxidized matrix has been observed with the scanning electron microscope (SEM) [52] and measured with the confocal interferometric microscopy (CIM) [53, 54] as shown in Fig. 1.16.

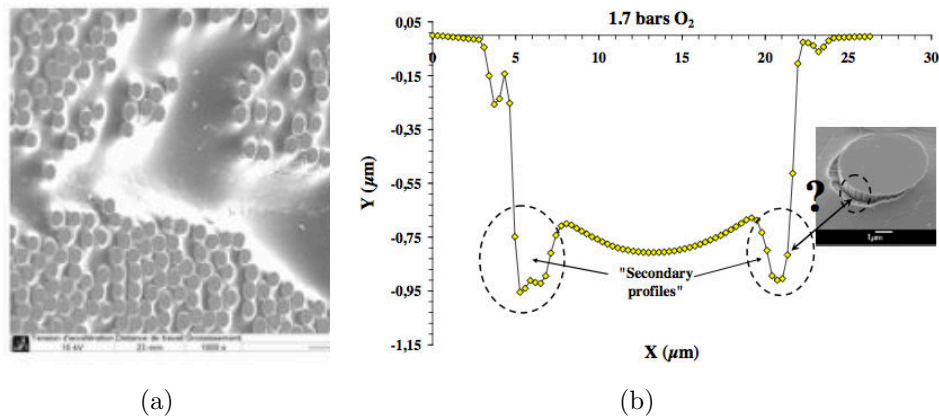


Figure 1.16: (a) SEM observations of specimen surface aged 1000 h in the air at 150 °C (b) Shrinkage of the matrix between fibers with the presence of fiber/matrix debonding measured with CIM [54]

The diffusion process in materials can be accelerated by the stress [71]. At the interphase zone, a stress field is generated by the thermal expansion mismatch between the fibers and the matrix due to the composite manufacture and the matrix shrinkage induced by the oxidation aging, which assists the oxygen diffusion at this zone [52]. Another scenario that may lead to the preferential propagation along the direction of the fibers is the fiber/matrix interface debonding [39, 54], which provides an additional pathway to penetrate. Furthermore, the different chemical composition of the interface may result in a different diffusivity also. But little information is available in the literature on the property of the interface.

Depending on the coupling between oxidation and damage, two modes of the damage assisted propagation exist. Colin et al. [57] have observed that the thickness of the damaged layer (TDL) in the fibers' direction grows cyclically in T800H/F655-2 material, whereas continually in IM7/977-2 material (Fig. 1.17). When interface damage mechanisms propagate faster than the oxidation, they stop at the unoxidized zone and restart until the formation of the new oxidized zone (Fig. 1.17(a)). On the other hand, when interface damage mechanisms propagate more slowly than the oxidation, they grow continually with the propagation of the oxidation (Fig. 1.17(b)) [57].

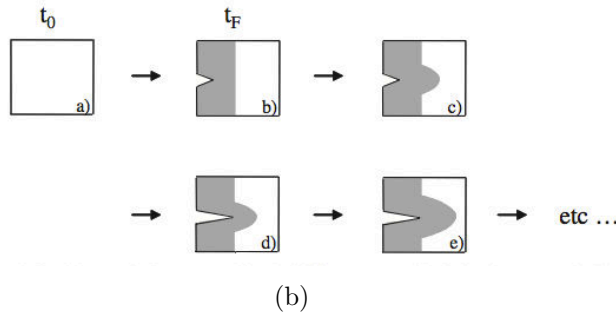
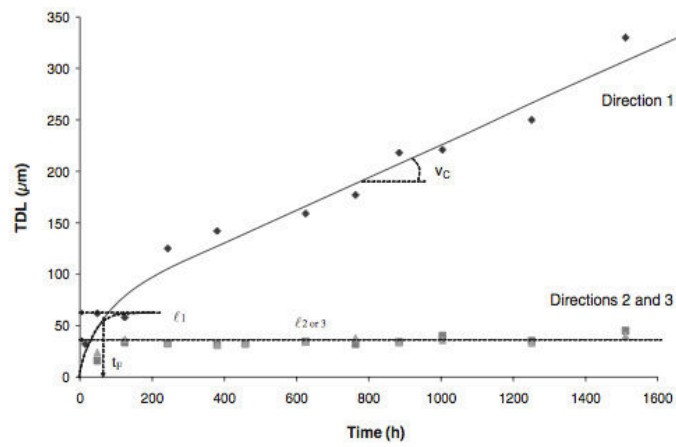
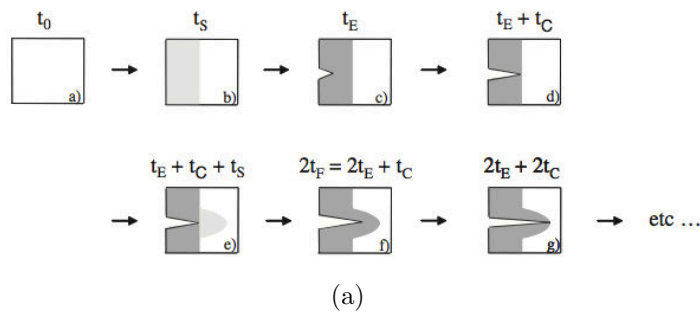
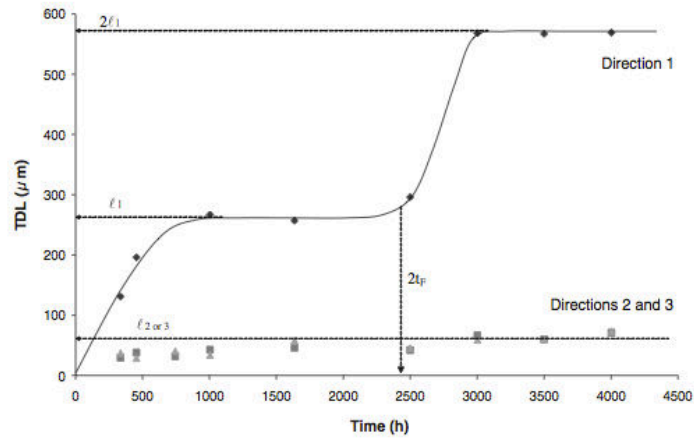


Figure 1.17: Evolution of TDL for (a) T800/HF655-2 system (b) IM7/977-2 system at 180 °C in the air and the expected cracking mechanisms [57]

1.5.2 Effects of the oxidation aging on composite materials

Due to the oxidized matrix, composite materials are also affected by the oxidation aging resulting in the weight loss [40, 58–60, 63], the shrinkage [52] and the variation of elastic modulus [60]. The experimental identification of the effects of the oxidation aging is usually carried out at the scale of the laminated composites. But unlike the aging on the thin neat resin film, the mechanism of the oxidation aging on the laminated composites is local and non-homogenous. Therefore, these studies are not fine enough to identify the properties of the composite materials as functions of the oxidation level.

The weight loss of the oxidized matrix leads to a weight loss of the total mass of composite materials. Thermogravimetric tests have been performed on composite materials to indicate material durability [40, 58–60, 63]. Some researchers have noted that composite laminates lose weight at a higher rate if their surfaces perpendicular to fibers present a more important area ratio, because of the anisotropic oxidation propagation [52, 59, 64].

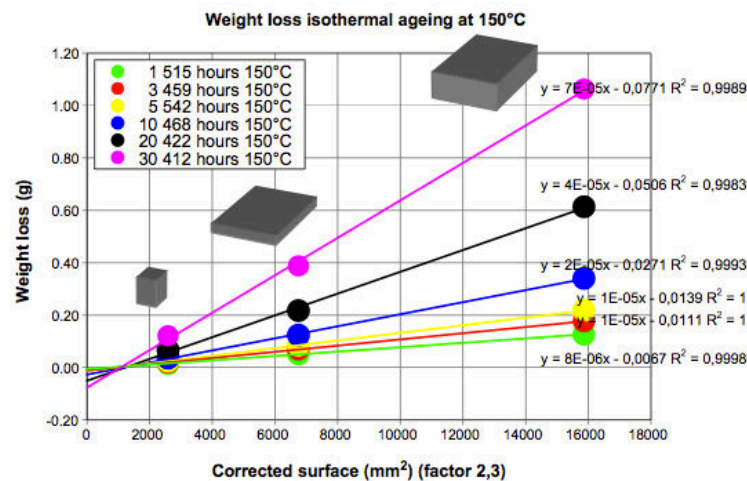


Figure 1.18: Weight loss evolution of different geometries during the isothermal aging at 150 °C [64].

Schoeppner et al. [52] have measured the volume change of the unidirectional G30-500/PMR-15 composite in the oxidative and the non-oxidative environments. The oxidation shrinkage on the matrix cause an additional volume change of composite materials compared with the non-oxidative environment (Fig. 1.19).

Parvatareddy et al. [60] identified the transverse modulus of the aged specimens with standard tensile test (ASTM D638M-91 [61]) on unidirectional specimens. The transverse modulus of two types of materials increased after aging at 150 °C for different times (Fig. 1.20) as a result of the increased elastic modulus of the matrix.

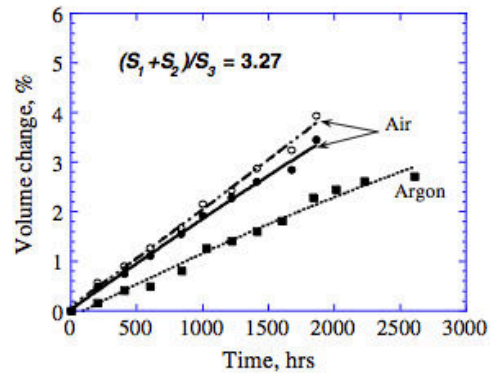


Figure 1.19: Volume change rates for specimens in the air and in the argon. [52]

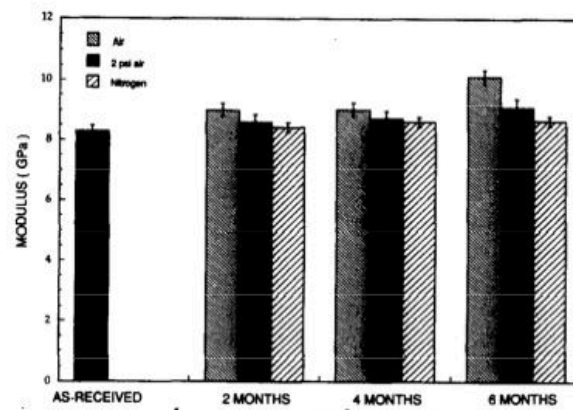


Figure 1.20: Change in transverse modulus of IM8/954-2 composites as a function of the aging time and environment at 150 °C. [60]

1.5.3 Damages and fractures of oxidized composite materials

Due the variation of the mechanical properties, the aged laminated composites behave differently from the unaged materials. Many tests have been performed to study the global ultimate strength or strain at the scale of laminated composite [21, 63–65] and the fatigue behavior [22, 66, 67]. The oxidation aging reduces the global fracture criteria of composite materials such as the short beam strength [63], compression and tensile strengths of the open hole specimens [64, 65] and the ultimate tensile strain of specimens (Fig. 1.21) [21].

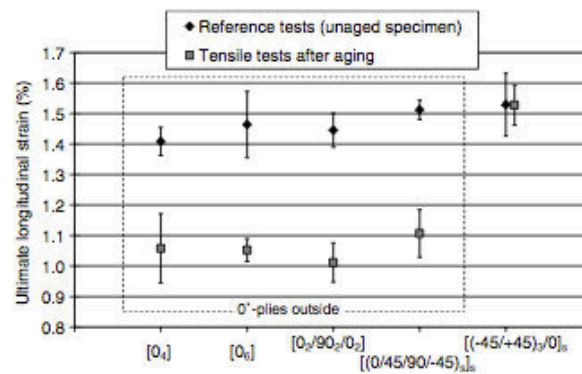


Figure 1.21: Comparison of ultimate axial strains of unaged samples and samples aged for 2 months at 210 °C. [21]

Lafarie-Frenot et al. [22, 66, 67] have carried out thermal fatigue loading ($-50\text{ }^{\circ}\text{C} \sim 180\text{ }^{\circ}\text{C}$) on samples of $[0_3/90_3]_s$ and $[\pm 45_3]_s$ in the non-oxidative and oxidative environment. X-radiographs have clearly illustrated that the oxidative environment generates more cracks, which shows the reduced fatigue resistance of laminated composites.

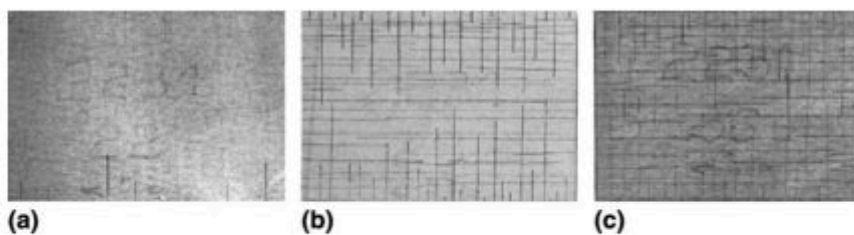


Figure 1.22: Comparison of X radiographs at 500 cycles in (a) nitrogen (b) air and (c) oxygen [22]

But, only a few studies have been carried out to identify the properties of the aged composite ply at the meso scale. Vu et al. [55] have studied the cracking behavior of the aged composite materials at the scale of a composite ply. Tensile tests were carried out on $[0/90_3/0]$ specimens aged in 1.7 bar oxygen for different times. The cracks on the

aged specimens initiated at a lower stress level compared with the unaged specimens. The aged specimens, however, behaved almost identically no matter the aging time.

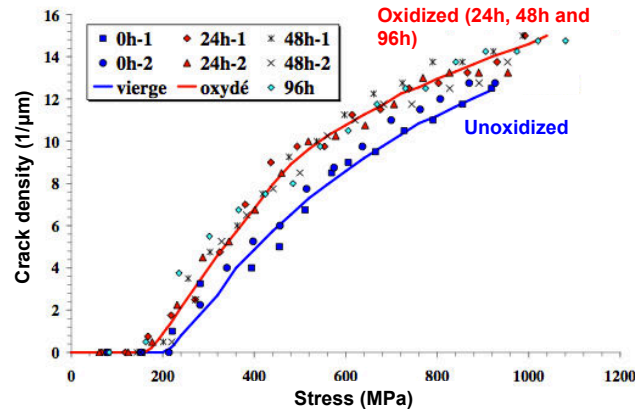


Figure 1.23: Crack density evolution as functions of the applied stress on $[0/90_3/0]$ specimens aged for different times [55]

In the lack of the studies at this scale, it is hard to achieve a better understanding of the global behavior of the laminated composites. The object of this thesis is thus to give our contribution on the studies of the oxidation aging on the composite materials at the meso-scale of a composite ply.

1.6 Modeling of the oxidation aging on composite materials

1.6.1 Microscale models of the oxidation aging on composite materials

Models at the microscale describe the composite material with discrete components or discrete damage mechanisms. Lafarie-Frenot et al. [18] developed a simulation tool based on a commercial FEM program. The model takes into account the diffusion/reaction process of the oxidation aging in the matrix (Eq. (1.25)). Shrinkage [16] and variations of elastic modulus [14] of the aged matrix are introduced as they are modeled for neat resin. The shrinkage of the matrix between fibers predicted by the model has a good consistency with the experimental measurements (Fig. 1.24(b)). Furthermore, the model shows also an important stress field around the fibers (Fig. 1.24(a)). But the possible damage at the fiber/matrix interface has not been taken into account.

Pochiraju et al. [44] consider a composite material ply as several representative volume elements (RVEs) containing two parts, the diffusive and reactive matrix and the

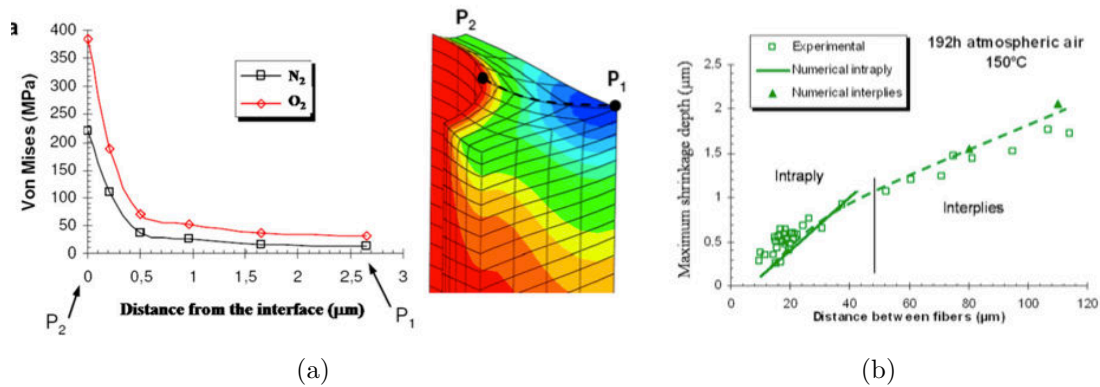


Figure 1.24: (a) Thermo-oxidation induced stress field close to the fibre/matrix interface (along path P1 to P2) (b) Experimentally measured vs. numerically predicted maximum chemical shrinkage depth as a function of the fibre-to-fibre distance in thermo-oxidized composite [18]

diffusive but inactive fiber-interphase assemblage. The model for the neat PMR-15 resin [17] has been used to describe the behavior of the oxidized matrix. The fibers-interphase assemblage is assumed inactive to oxygen and its diffusivity is assumed anisotropic to represent the anisotropic propagation of the oxidation aging on a composite ply. The diffusivity of the fiber-interphase assemblage is identified by fitting the numerical results with the experimental observations. Discrete axial cracks can be introduced into the model and assumed to propagate at a constant rate between two RVEs. The crack surface is also considered the exposed surface, which allows to simulate the damage assisted diffusion (Fig. 1.25) and to determine the energy release rate of cracking propagations. The model takes into account the damage assisted diffusion, but cracks are assumed to propagate at a constant rate independent of the nearby stress field generated by the oxidation.

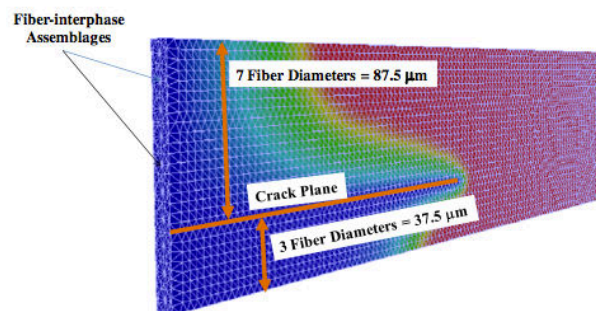


Figure 1.25: Oxidation growth prediction in an unidirectional composite with the orthotropic fiber-interphase assemblage diffusivity and the presence of a discrete crack [44]

A micromodel has been developed in LMT-Cachan to simulate the behavior of the laminated composites, in which cracks are represented discretely. Lubineau et al. [68,69] extended the model to take into account the effects of the oxidation aging. The oxidation assisted damage is introduced by reducing the critical strain energy release rate of the oxidized material (Eq. (1.44)). Furthermore, the model considers a surface is oxidized if it is contact with the environment through the cracks, which allows to simulate the damage assisted diffusion. However, the model remains phenomenological because all the effects of the oxidation aging is introduced as one empiric parameter reducing G_c .

$$G_c = \overline{G}_c(1 - \eta_{ox}) \quad (1.44)$$

where η_{ox} is the parameter associated to the oxidation aging depending on the temperature and the partial oxygen pressure, \overline{G}_c and G_c are respectively the critical strain energy release rate of the unaged and the aged composite material.

Thanks to the understanding of the oxidized neat resin, some micro-scale models [18, 44] are able to represent precisely the phenomena at the fiber/matrix scale, for example the stress field around fibers and the damage assisted diffusion. On the other side, some model [68,69] takes into account the oxidation assisted damage, but describes it in a phenomenological way. But a modeling containing a more scientific base of the coupling between the oxidation and the damage mechanisms is still missing so far. Moreover the micro-scale models are too numerically expensive to study the the behavior of laminated composites.

1.6.2 Mesoscale model of the anisotropic propagation

Colin et al. [23, 26, 57] modeled the anisotropic diffusion/reaction process in unidirectional composite materials at the mesoscale, which considers a composite ply as one structure whose diffusivities are anisotropic. The axial diffusivity (D_1) is considered to be the same as the oxygen diffusivity of the neat resin (D) if no interface damages occur

$$D_1 = D \quad (1.45)$$

The transverse diffusivity (D_2) is considered to be slower due to the presence of the fibers based on a geometric consideration:

$$D_2 = \frac{1 - 2\sqrt{V_f/\pi}}{1 - V_f} D_1 \quad (1.46)$$

The surfaces of carbon fibers are considered to participate in the oxidation reactions. Two equations of the kinetic diffusion/reaction model for the neat resin (Eq. 1.31) are modified to adapt the use on unidirectional composite.

$$\begin{aligned}
\frac{d[P^\circ]}{dt} &= 2k_1[POOH] - k_2C[P^\circ] + k_3[PH][PO_2^\circ] - 2k_4[P^\circ]^2 - k_5[P^\circ][PO_2^\circ] - k_7[P^\circ][Carb] \\
\frac{d[PO_2^\circ]}{dt} &= k_2C[P^\circ] - k_3[PH][PO_2^\circ] - k_5[P^\circ][PO_2^\circ] - 2k_6[PO_2^\circ]^2 - k_8[PO_2^\circ][Carb]
\end{aligned}
\tag{1.47}$$

The oxygen consumptions can be thus rewritten as

$$R(C) = 2R_0\Psi \frac{\beta^*C}{1 + \beta^*C} \left[1 - \frac{\Phi\beta^*C}{2(1 + \beta^*C)} \right] \tag{1.48}$$

where

$$\begin{aligned}
\Psi &= \left(1 - \frac{\varphi}{2}\right) \left(1 + \frac{\varphi}{4}\right), \quad \Phi = \frac{1 - \varphi/2}{1 + \varphi/4} \quad \text{and} \quad \beta^* = \frac{\beta}{1 + \varphi/4} \\
\text{with} \quad \varphi &= \frac{k_7[Carb]}{k_3[PH]}
\end{aligned}
\tag{1.49}$$

Comparing the predictions of the model with the thickness of the damaged layer (TDL) observed experimentally, only D_1 of IM7/977-2 material is similar to the D of the neat 977-2 resin. Colin et al. [23, 26, 57] attribute the difference between D_1 of the T800H/F655-2 material and D of the neat F655-2 resin to the additional diffusion path provided by cracks. The damage assisted oxygen diffusion is modeled by assuming the oxygen concentration (C) within the crack zone is as rich as the exposed surface.

$$C(0 \leq x \leq CL) = C_s \quad \text{for } t > t_F \tag{1.50}$$

where CL is the crack length, t_F is the crack initiation moment. The propagation of cracks is defined as

$$CL = v_C(t - t_F) \quad \text{for } t > t_F \tag{1.51}$$

where v_C is a constant propagation velocity. v_C and t_F seem obey the Arrhenius law [57]. They can be both identified graphically from the evolution of TDL. The predicted profile of the oxygen concentration is shown in Fig. 1.26

1.7 Conclusion

In this chapter, previous studies on the oxidation aging on neat resin and on composite material are summarized. The diffusion/reaction process of the oxidation aging on neat resin [23, 37–39] as well as its effects such as the weight loss [23–25], the

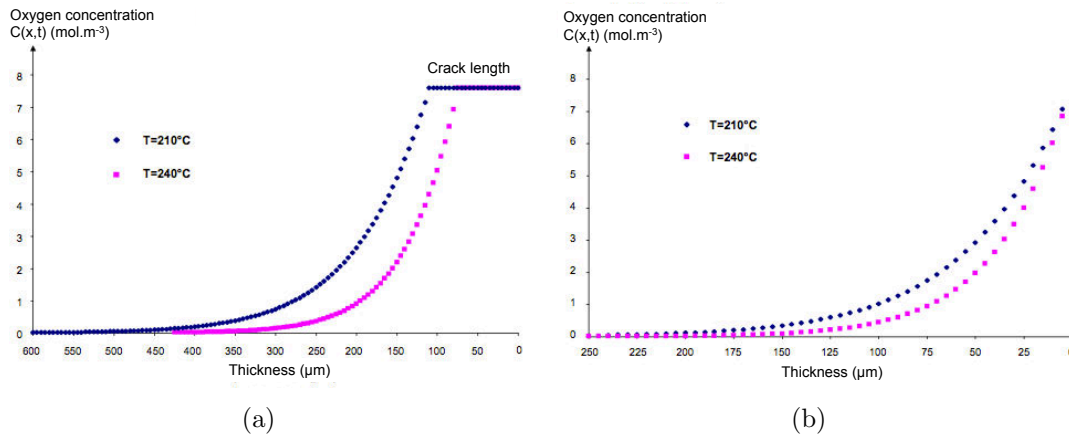


Figure 1.26: Profile of stationary oxygen concentration (a) in the direction along the fibers (b) in the direction transverse to fibers [23]

shrinkage [15–17], the increase of the elastic modulus [26–28] have been widely studied experimentally. Based on the rich experimental data, various approaches have been proposed to model the oxidation aging on neat resin. The kinetic diffusion/reaction approach based on the chemical mechanistic scheme [23] reduces the empirical parameters and seems to be applicable in more general studies on different materials and aging conditions. The shrinkage and the elastic modulus are either calculated from the kinetic diffusion/reaction approach [16, 26] or related to oxidation level indicators obtained from the kinetic diffusion/reaction approach [14, 17].

The studies of the oxidation aging on composite materials have been carried out at different scales due to the complexity of the material structure. At the microscale, both experimental and numerical studies are carried out. Several models [17, 18] have been proposed whose results seem to have a good consistency with the experimental researches [53, 54]. Some models [18, 44] take into account the damage assisted diffusions, some [69] has taken into account the oxidation assisted damage. But a better understanding on the coupling of the oxidation and the damage is still missing. For the same reason, although the propagation of the oxidation aging has been observed [23, 52] and modeled [23, 26] as an anisotropic phenomenon at the scale of a composite ply, crack are assumed to propagate at a constant velocity independent of the oxidation levels. Also, few studies have been successful in identifying the properties of the aged composite materials as functions of the oxidation levels at the mesoscale because the oxidation aging on a composite ply is a local and non-homogeneous phenomenon. A lack of the understanding on the mechanical behavior of an aged composite ply still exists. Thus no models can predict the behavior and the fracture of the oxidized laminated composite material with a more scientific base, though a large number experimental data exist at this scale [21, 63–65].

The objective of this work is thus to give our contribution on the understanding of

mesoscale mechanical behavior of an aged composite ply. The properties and damage mechanisms are going to be investigated with both experimental and numerical studies.

Chapter 2

Preliminary observations on effects of the oxidation aging on the laminated composite material

Contents

2.1	Introduction	40
2.2	Preparations of samples	40
2.2.1	Material and aging conditions	40
2.2.2	Preparation of surfaces for microscopic observations	41
2.3	Preliminary observations with optical microscope	42
2.3.1	Light field illumination and dark field illumination	42
2.3.2	The anisotropic propagation of the oxidation aging	45
2.3.3	Coupling between the oxidation aging propagation and damage mechanisms	49
2.4	Conclusion	51

2.1 Introduction

This part presents the work and the results of preliminary microscopic observations on samples aged for different durations. There are two reasons to perform the observations. First, different phenomena, for example the anisotropic propagation of the oxidation aging on composite materials or the fiber/matrix interface debonding, have been observed in previous studies [52, 54]. However, in LMT-Cachan, it is the first time that an experimental study on the oxidized composite material is carried out. By repeating the works in the literature, one can be familiar with the experimental methods of the study on oxidized composite materials and obtain a general understanding of the effects of the oxidation aging on our material. Second, since the oxidation aging on the laminated composites is a local phenomenon, it is necessary to distinguish the oxidized zone from the unaged part when modeling the problem at the mesoscale. In this context, the oxidized/damaged zone which is lighted under the dark field illumination might be able to provide an interesting indicator.

The chapter firstly presents the material, the observed surfaces and the aging conditions. The experimental methods are also detailed. Surfaces of samples are polished following an optimized polishing protocol, and then observed with an optical microscope in two modes of illuminations, which allow us to observe different phenomena. A lighted zone was found under the dark field illumination and used as an indicator of the oxidized/damaged zone. These observations helped us confirm the previous observations in the literature that oxidation aging is actually an anisotropic and local phenomenon for a composite ply. Furthermore, a new phenomenon that is the crack crossing only the oxidized layer is observed under the light field illumination.

2.2 Preparations of samples

2.2.1 Material and aging conditions

The material used in this study is an unidirectional pre-impregnated tape composed of an epoxy matrix and high tensile strength (HTS) carbon fibers. The laminated composite plates were provided by Airbus Group Innovaions. The matrix accounts for 34% of the mass fraction of the composite material. Sequences of the laminate panels used in this study are $[0_8]$ and $[90/0]_s$. The nominal thickness of each ply is 0.16 *mm*, however the average thickness of a ply is measured as 0.14 *mm*.

Square samples of 20 *mm* as the edge length were cut from the laminate panels with a saw machine. Samples were then dried in an oven (SAT-2046) at 70 °C for 7 days to eliminate the moisture and to avoid the coupling between the oxidation aging and the hygrothermal aging. The samples were then divided into 4 groups after drying. Each group contained one sample of each sequence. One group was kept directly in a

desiccator with the calcium chloride inside to keep the samples dry. Additionally, the desiccator was always connected to a pump to keep a vacuum condition. The other groups were aged at 180 °C in the oven for respectively 1, 3, 6 weeks. After aging, the oxidized samples were kept in the same desiccator with the unaged group until the polishing process.

2.2.2 Preparation of surfaces for microscopic observations

The samples were then cut one more time to show two internal sections, one parallel to the fibers, the other one perpendicular to the fibers. Only the edges of the sections but not the surfaces had been exposed to the air during the aging process, which allowed us to monitor the propagation of the oxidation aging along the direction of the fibers and transverse to the direction of the fibers. The cut samples were then embedded in an acrylic resin for the polishing process.

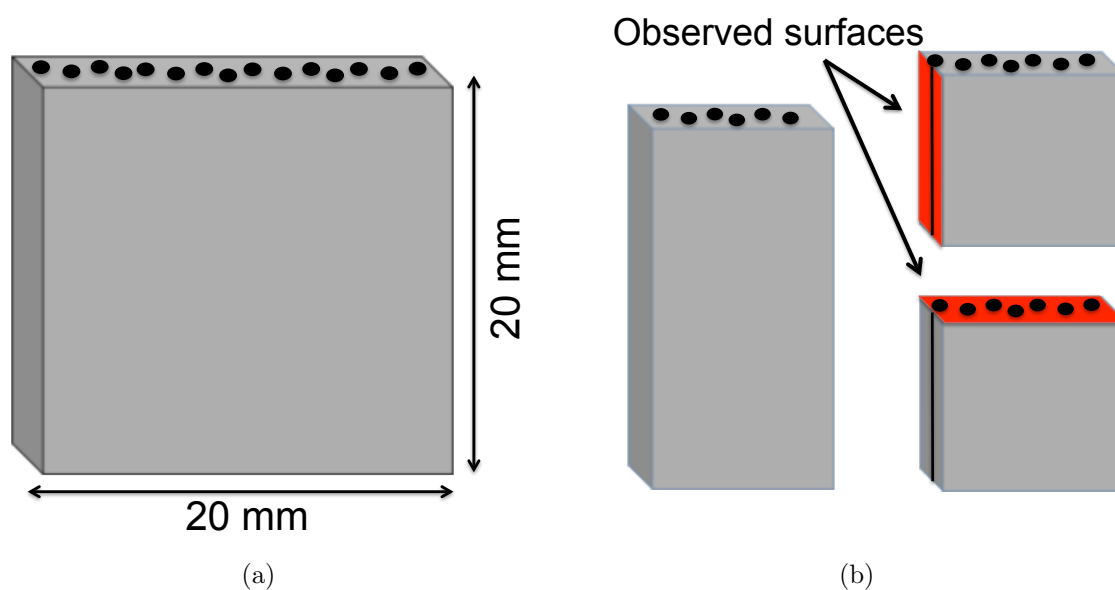


Figure 2.1: (a) The geometry of samples (b) The observed surfaces

The observation requires a good quality of the surface state. The preparation of the surfaces was realized with the polishing technique. Vu et al. [54] have studied systematically the influence of different control parameters of a polishing protocol on the surface state of a carbon/epoxy composite material. He proposed an optimized automatic protocol to polish the surface without generating many damages. According to the available equipments in our laboratory, we have used a similar protocol (Tab 2.1) based on his study. The automatic polishing process was realized with the polishing machine, Struers RotoPro-31, which makes the polishing process reproducible.

Table 2.1: The automatic polishing protocol

Step	Code of polishing paper or finesse of polishing diamond	Lubricant	Duration (min)	Speed (rpm)	Pressing force (N)
1	320	Water	1	150	30
2	600	Water	5	150	30
3	1200	Water	5	150	30
4	2400	Water	5	150	30
5	4000	Water	10	150	30
6	Struers DiaDuo-2 mixed liquid (1 μm diamond)		10	150	30

Microscope observations showed a clear and planar surface of the unaged samples after polishing (Fig. 2.2). The fibers and the matrix can be easily distinguished. No significant damages on fibers or in the fiber/matrix interfaces are observed.

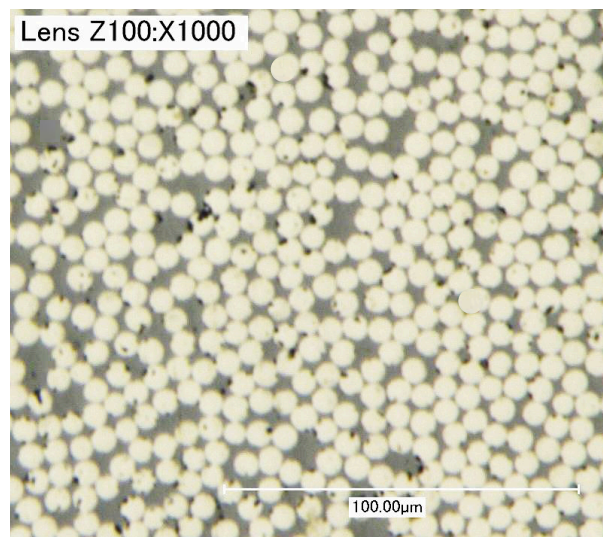


Figure 2.2: The surface of an unaged samples after polishing

2.3 Preliminary observations with optical microscope

2.3.1 Light field illumination and dark field illumination

After polishing, the samples were observed with the optical microscope in two modes of illumination, the light field illumination and the dark field illumination. The two modes are distinguished by the position of the light source as shown in Fig. 2.3. The light field is the zone from where a specular light can reach the eyepiece or the sensor

of a microscope after the reflection. On the contrary, the dark field is the zone from where a specular light is normally reflected away from the eyepiece or the sensor. They allowed us to observe different phenomena on the surfaces of the oxidized samples.

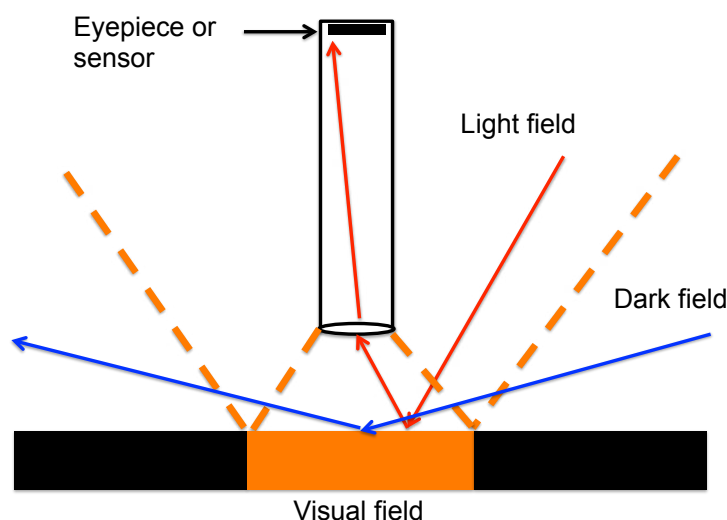


Figure 2.3: The light field and the dark field illumination on a plane surface

The light field illumination has the simplest setup and a light visual field but a relatively low contrast due to the specular reflections on reflective surfaces. The dark field illumination provides usually a dark background. However, lights can be diffused into the visual field by textured surfaces, which shows the elevation variation of the surface (Fig. 2.4). The dark field illumination has been successfully used to monitor the propagation of the oxidation aging by measuring the evolution of the lighted zone [54,72]. In our study, photos as shown in Fig. 2.5(a) were captured with the microscope under the dark field illumination. The contrasts of the photos have been then enhanced so that the lighted zone is more visible (Fig. 2.5(b)).

Fig. 2.6(a) shows the surface of a sample aged for 6 weeks under the light field illumination. Due to the low contrast of the light field illumination, the surface state seems to be identical although the sample has been aged. Fig. 2.7(d) shows the same surface under the dark field illumination. The lightness of the coating resin may be attributed to the different refrangibility of the semitransparent resin. The darkness of most part of the sample shows that the surface of most part is clean and planar, which validates the automatic polishing process in another way. However a lighted zone can be observed on the edge of samples. It shows a variation of the surface state, which can be explained by the diffusion/reaction process of the oxidation aging. The edge zone is usually importantly aged since a significant quantity of oxygen can be provided from the exposed surfaces. The matrix at the edge zone have been extracted instead of having been polished during the polishing process due to the stresses and the weakening effect generated by the oxidation aging. The extractions of the matrix leaves a textured

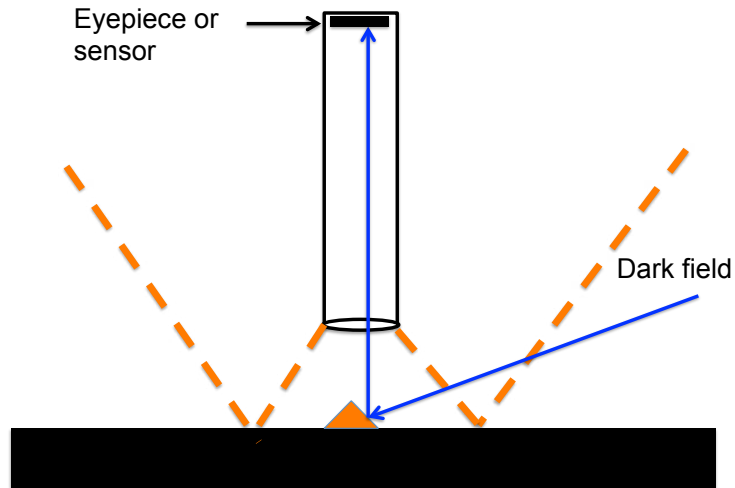


Figure 2.4: Dark field illumination on a textured surface

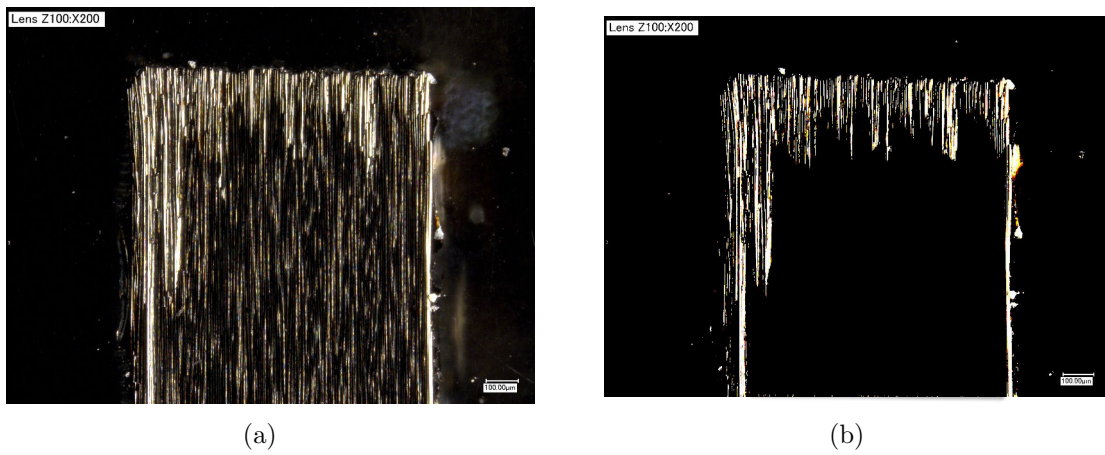


Figure 2.5: Image of surface of an aged sample under dark field illumination
(a) original (b) enhanced

surface which diffuses light and is lighted under the dark field illumination. The lighted zone represents actually an oxidized/damaged zones. It provides an important indicator of the oxidation aging on the microstructure of composite materials.

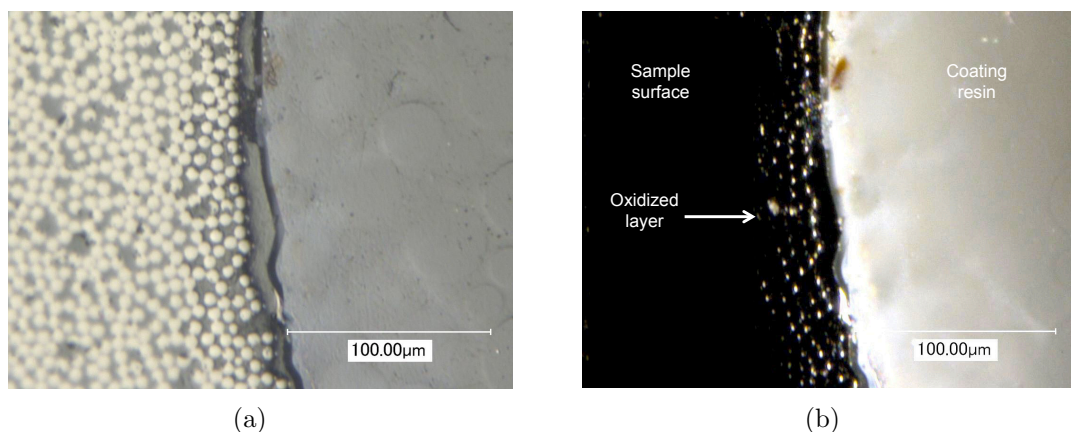


Figure 2.6: A surface perpendicular to fibers of samples aged for 6 weeks under (a) the light field illumination (b) the dark field illumination

2.3.2 The anisotropic propagation of the oxidation aging

The oxidation aging is a local phenomenon controlled by the oxygen diffusion and the oxidation reaction. The propagation of the oxidation aging is generally limited by the amount of the oxygen that diffuses into the material rather than by the reaction rate. As the lighted zones under the dark field illumination represent the effect of the oxidation aging, it is chosen to be the indicator to monitor the propagation of the oxidation aging. Fig. 2.7 shows the microscopic observations of the surfaces perpendicular to the fibers of samples aged for different durations under the dark field illumination. Lighted zones due to the extraction of the matrix were observed on the surfaces of the aged samples.

Lighted zones were also observed on the surfaces parallel to the fibers on the aged samples under the dark field illumination due to the extraction of fibers (Fig. 2.8).

The average thicknesses of the lighted zones are measured from the microscopic observations and given in Tab. 2.2. The propagations of the oxidized/damaged zone in both directions are composed of two steps as shown in Fig. 2.9. At the beginning of the aging process, the oxidized/damaged zone propagates fast because sufficient oxygen can be easily provided by the air for the oxidation aging at the zones near the exposed surfaces. With the continuation of the aging process, less and less oxygen could diffuse into the deeper region. The propagation of the oxidized/damaged layer thus slows down. But unlike a previous study [23], the propagation of the oxidation aging in the transverse direction does not tend to an asymptotical thickness in our study. The difference may be attributed to the different diffusion/reaction rates of

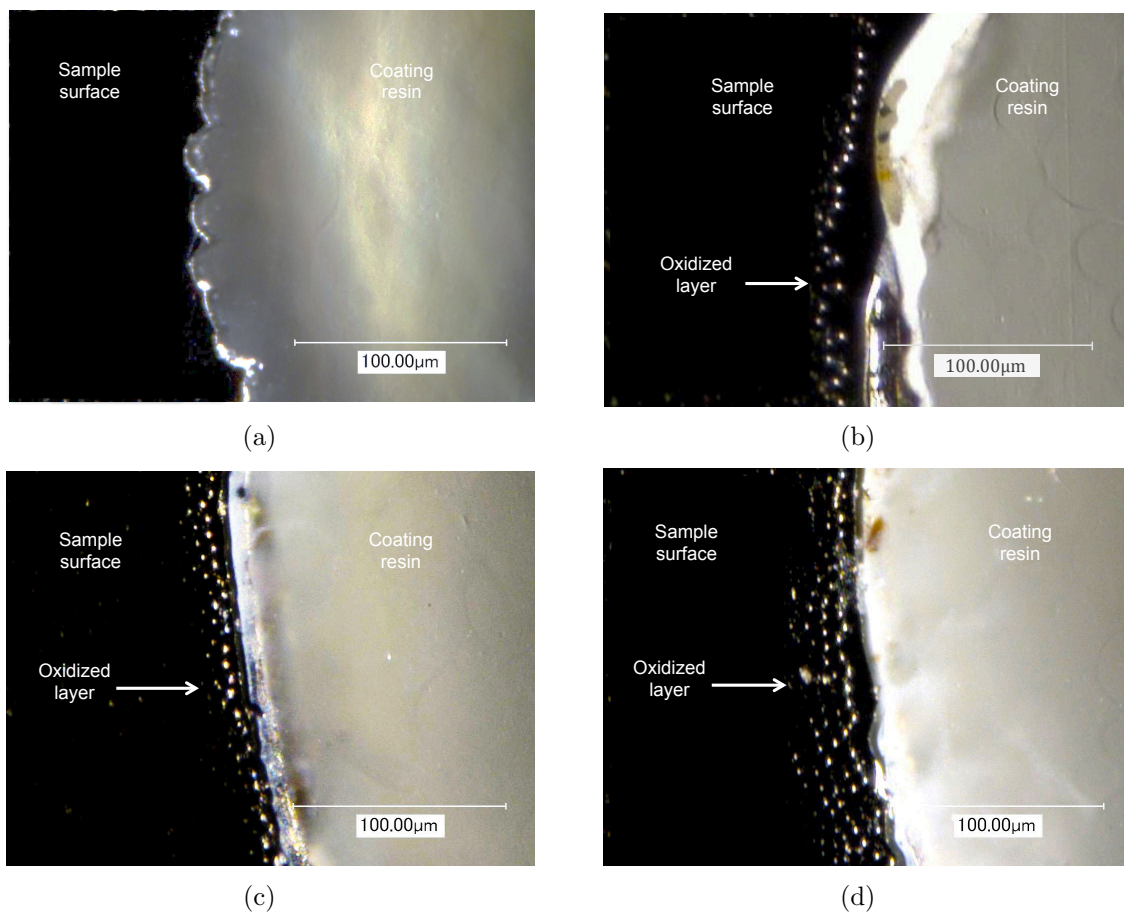


Figure 2.7: Surfaces perpendicular to fibers under dark field illumination (a) unaged (b) aged for 1 week (c) aged for 3 weeks (d) aged for 6 weeks

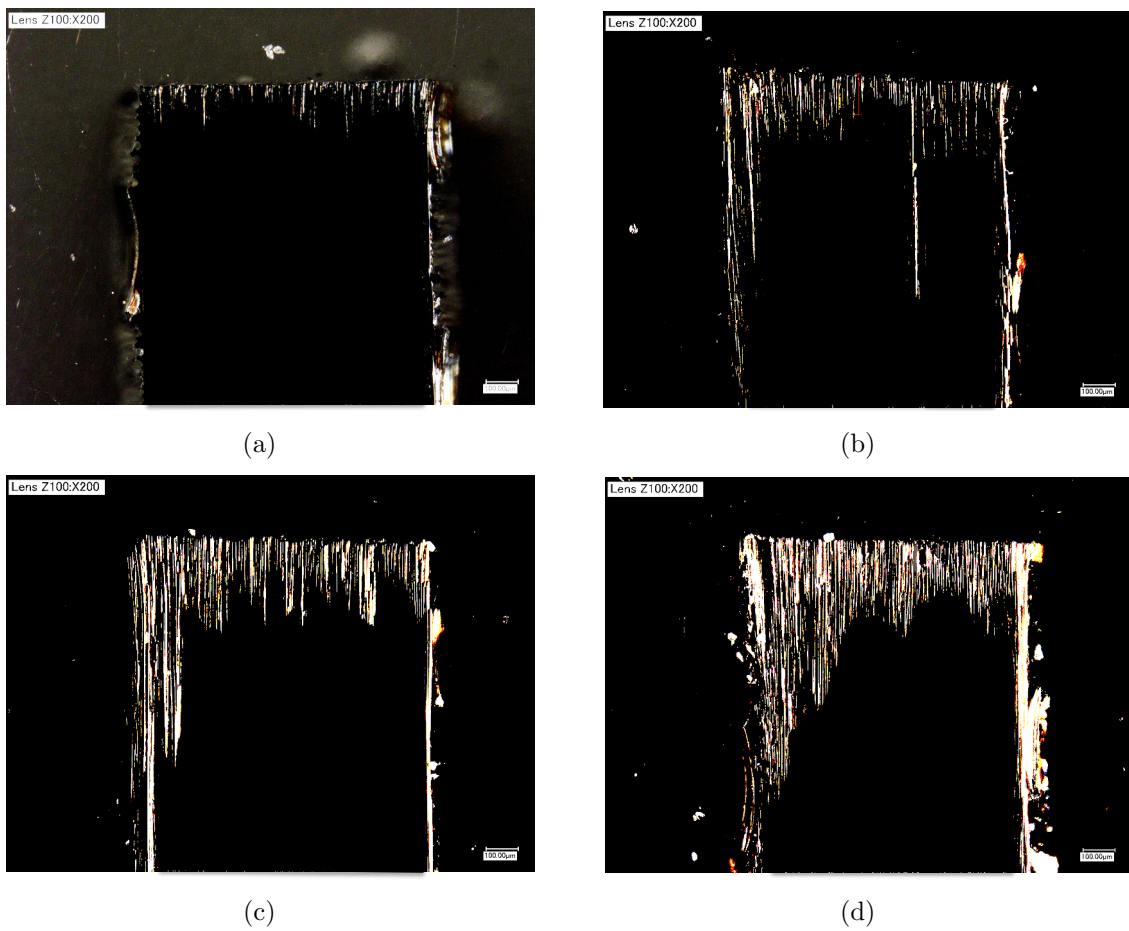


Figure 2.8: Surfaces parallel to fibers under dark field illumination (a) unaged (b) aged for 1 week (c) aged for 3 weeks (d) aged for 6 weeks

different materials. An asymptotical thickness could be expected after the aging of a longer duration.

Table 2.2: The evolution of the average thickness of the oxidized/damaged layer

Aging time (h)	Axial propagation (μm)	Transverse Propagation (μm)
168	128	7.3
504	213	19.7
1008	315	33.3

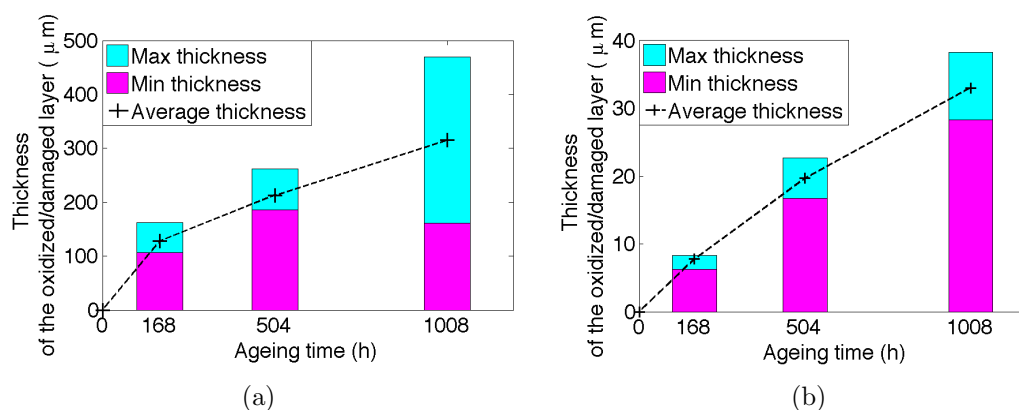


Figure 2.9: Evolutions of the thickness of oxidized/damage zone (a) along the direction of the fibers (b) transverse to the direction of the fibers

Furthermore, it is confirmed that the propagation of the oxidation aging is anisotropic on a composite ply by comparing the oxidized/damaged zones in the two directions. It has been well documented that the propagation of the oxidation along the direction of the fibers is faster than that transverse to the direction of the fibers on unidirectional composites [23, 52, 70]. For our material, the anisotropy ratio of the propagation is about 10 which is comparable to the ratio identified in a previous study which is 8 [39]. The slight difference can be attributed to different materials and different aging conditions. Two reasons have been given to explain the anisotropic propagation. In the transverse direction, the presence of fibers prevents the oxygen diffusions [23]. In the axial direction, the propagation of the oxidation aging is accelerated by the stress and the damage at the fiber/matrix interphase.

2.3.3 Coupling between the oxidation aging propagation and damage mechanisms

In the axial direction, the strong coupling between the propagation of the oxidation aging and the damage mechanisms is a well known phenomenon [39, 52, 54]. On one hand, the stress and the damage at the interphase zone accelerate the oxygen diffusion, on the other hand, the oxidation aging induces the interface degradation. The two phenomena accelerate each other, which allows the oxidation aging to penetrate towards the core of the material. Stresses at the interphase, which are generated by the oxidation induced shrinkage, depend on the different local percentages of the matrix. The damage mechanisms at fiber/matrix interphase zone may thus occur at different moments, which explains the irregular front of the oxidized/damaged zone in Fig. 2.8 and the important variations of the oxidized/damaged zone in Tab. 2.2.

In the transverse direction, cracks crossing partially a composite ply were observed with an optical microscope (Fig. 2.10). It has been documented that cracks may initiate on the surfaces perpendicular to the fibers and propagate along the direction of the fibers in isothermal or thermal cycling oxidation conditions [52, 73]. In our study, observations have been carried out on $[90/0]_s$ samples to observe the cracks which initiate on the free surfaces parallel to the fibers and propagate transverse to the direction of the fibers. About thirty cracks within a distance of 10 mm were observed on the external 90° plies which are exposed to the oxidative environment and aged at 180°C . The anisotropic thermal expansion coefficients of a composite ply generate tensile stresses in 90° plies of $[90/0]_s$ samples after the cooling step of the manufacture. With the process of the oxidation aging, the tensile stresses are enhanced by the shrinkage and the increase of the elastic modulus induced by the oxidation aging, which may initiate cracks. In this thesis, the generation of cracks by the effects of the oxidation aging without any additional mechanical loading is also referred to as the self-cracking phenomenon.

Moreover, cracks in classical mode extend instantly throughout the thickness of the 90° ply and stop at the interfaces with the adjacent plies. However, on the aged samples, most of the cracks initiate from the oxidized external surfaces and cross partially the 90° plies. The lengths of the cracks are quite variable as shown in Fig. 2.11, but the average length is slightly higher than the thickness of the oxidized/damaged layer estimated with the dark field microscopy ($53\ \mu\text{m}$ versus $33\ \mu\text{m}$).

Therefore, the partial cracks on the samples aged for 6 weeks are also considered as the cracks crossing the oxidized layer. Furthermore, the partial cracks also enable the damage assisted propagation of the oxidation aging which is shown as an oxidized/damaged zone around the crack tips (Fig. 2.12). The preference of the cracks crossing the oxidized layer will be further explored with the simulation tool at the microscale from an energetic point of view in Chapter 5.

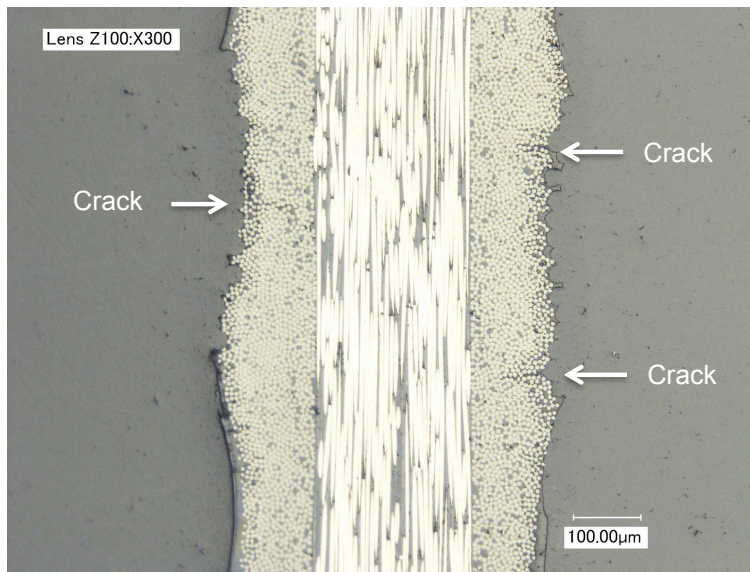


Figure 2.10: The surface of an unaged samples after polishing

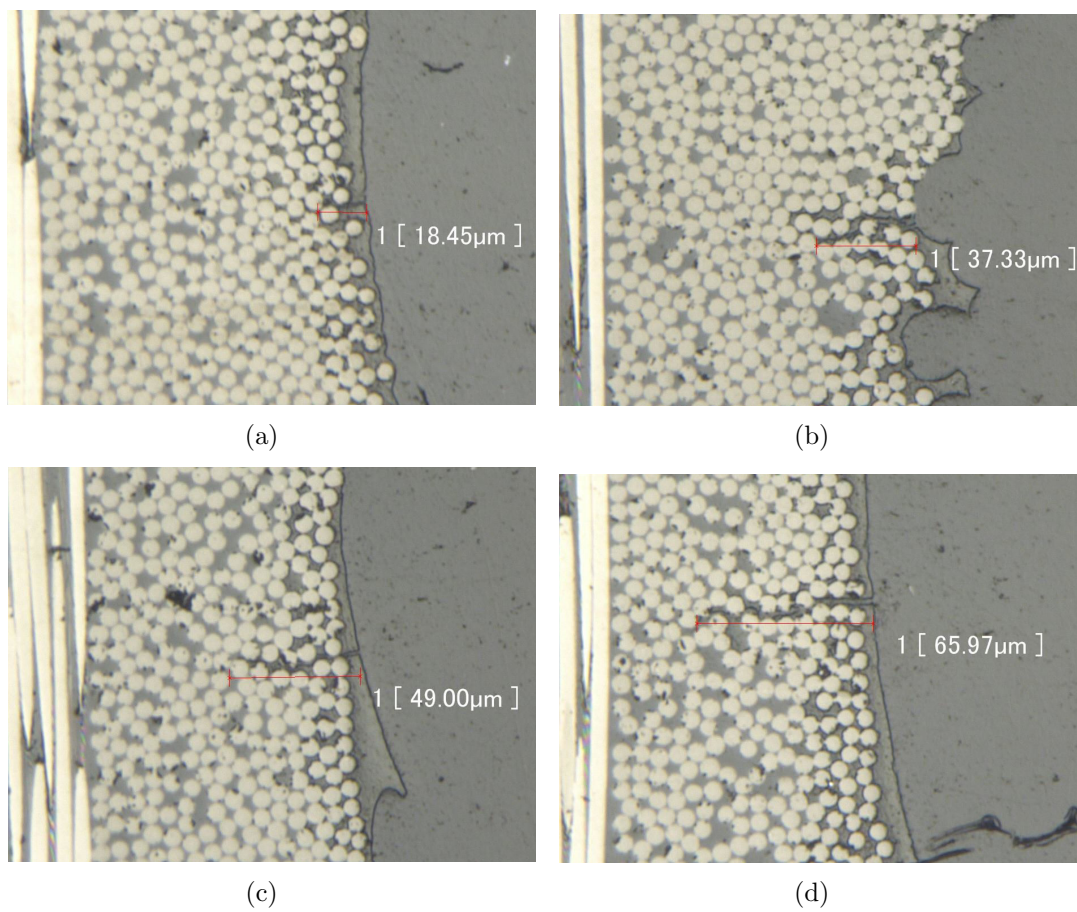


Figure 2.11: Partial cracks of different lengths

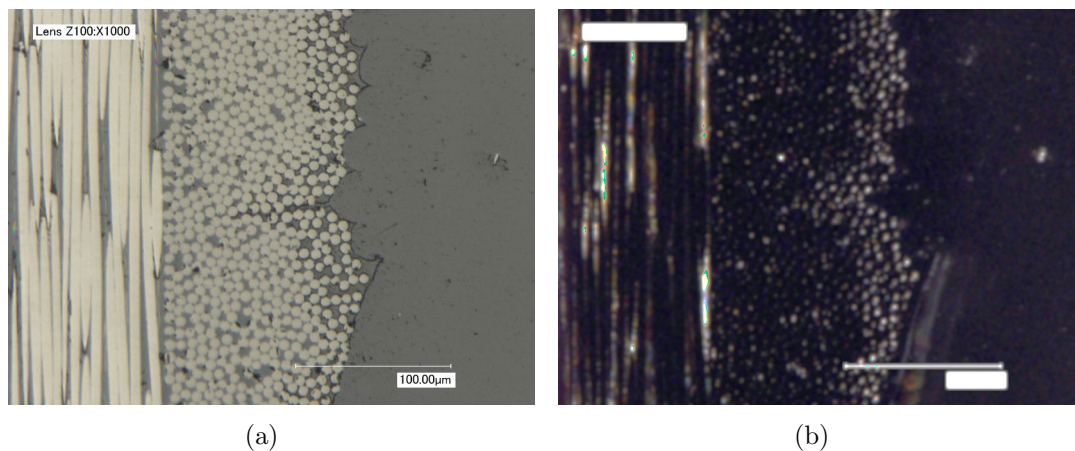


Figure 2.12: Damage assisted propagation of the oxidation aging on samples with partial cracks (a) Light field illumination (b) Dark field illumination

2.4 Conclusion

This chapter has presented the preliminary microscopic observations on the polished surfaces of samples aged for different durations. The surface of oxidized/damaged zone has been used as the indicators to monitor the propagation of the oxidation aging thanks to its lightness under the dark field illumination. The propagation on a composite ply is confirmed as an anisotropic phenomenon. The oxidation propagates much faster from the surfaces perpendicular to the fibers than from the surfaces parallel to the fibers. Moreover, the oxidation aging could change the cracking behavior of laminated composites. Spontaneous cracks crossing only the oxidized layer have been observed on the $[90/0]_s$ samples aged at $180\text{ }^\circ\text{C}$ in the air for 6 weeks.

Thanks to the above-mentioned microscopic observations, a general understanding of the oxidation propagations and of the effects of the oxidation aging on the laminated composites has been obtained. The oxidation aging has two effects on laminated composites, a surface effect and an edge effect as shown in Fig. 2.13. The surface effect extends over the entire outer surface of the laminate through a thickness comparable to the one of a ply. It weakens the material, increases the elastic modulus of the material, induces the shrinkage within the oxidized layer and may activate the self-cracking phenomenon which will tend to stop at the adjacent plies. The edge effect penetrates much faster from the surfaces perpendicular to fibers due to the coupling between the oxidation and the mechanisms at the fiber/matrix interphase.

Different experimental activities and numerical activities were developed and performed to study the two effects. For the surface effect, tensile tests were carried out on the $[90/0]_s$ samples aged at $180\text{ }^\circ\text{C}$ in the air for different durations to observe the behavior of the oxidized laminated composites. Studies at the microscale are introduced

to search the meso-scale properties of an aged composite ply via a homogenization method. A meso-scale modeling strategy is proposed to describe the behavior of composite materials observed from meso-scale tests with properties characterized from the micro-scale study. For the edge effect, a new test has been developed in LMT-Cachan based on the standard climbing drum peel test (ASTM D1781-98 [20]) to study the effects of the oxidation aging on the interlaminar fracture criteria.

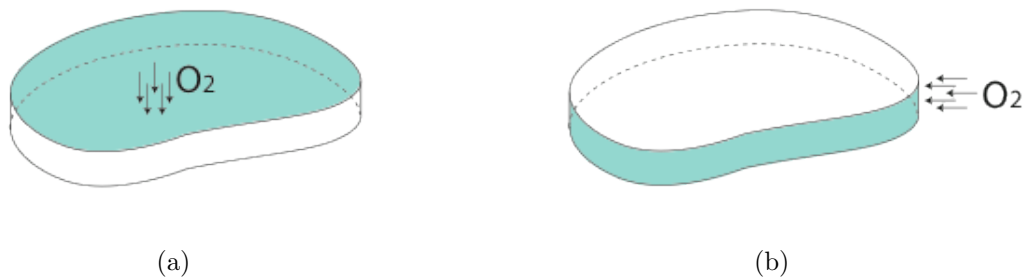


Figure 2.13: (a) Surface effect (b) Edge effect

Chapter 3

Micro-scale modeling and homogenization of the oxidized composite material

Contents

3.1	Introduction	54
3.2	The properties of the oxidized resin	54
3.3	Homogenization method	56
3.3.1	Homogenization without the effects of the oxidation aging	56
3.3.2	Homogenization with the effects of the oxidation aging	59
3.3.3	FEM calculations of a unit cell of composite materials	62
3.4	Stress field around fibers	64
3.5	Homogenized properties of composite materials	66
3.5.1	Stiffness of unaged composite materials	66
3.5.2	Elastic modulus of aged composite materials	66
3.5.3	Shrinkage of aged composite materials	68
3.6	Discussion	68

3.1 Introduction

The properties of an oxidized composite ply are required to study the behavior of the oxidized laminated composites. However, the mechanisms of the oxidation aging on composite materials occur actually at a lower scale which is the fiber/matrix scale. The oxygen reacts only with the organic matrix of composite materials at the studied temperature interval ($150^{\circ}C \sim 250^{\circ}C$), which leads to variations of the matrix properties. Since oxidation affects a limited portion of the composite in our study (less than a ply thickness), it is difficult to identify the properties of the oxidized composite using the standard tests on composite specimens.

In this chapter, two effects of the oxidation aging on the composite (increase of the elastic modulus and shrinkage) are going to be investigated. A micro-scale model is introduced, in which the composite material is considered to be a repetition of a periodic unit cell which contains two components, the fiber and the matrix. The matrix properties (elastic modulus and shrinkage) vary with the oxidation aging. The local stress-strain state within the unit cell is obtained via FEM simulations, and the mesoscale properties are calculated via a periodic homogenization. These homogenized properties are going to be used in the studies of the damage behavior of an oxidized composite ply in the following chapters.

The input data for the homogenization procedure are the properties of the fibers and of the matrix as functions of the oxidation level. Studies on the oxidized resin such as those discussed in Chapter 1 could provide the information for the material systems based on this resin. In the present case, however, the characterization of the oxidized matrix by the project partners was carried out in parallel with the work presented here. In the lack of the information on our material, pragmatic choices had to be made in order to feed the micro-scale model. This may affect the quality of the predictions, however it does not affect the foundation of the proposed approach.

3.2 The properties of the oxidized resin

As it has been discussed in Chapter 1, the properties of the oxidized resin vary with the oxidation process. Different studies propose to describe them as functions of a parameter representing the oxidation level, for example a weight loss term [44] or the concentration of oxidation products (Q) [16, 49]. The oxidation level, in turn, can be predicted as a function of the aging conditions (time, temperature, oxygen concentration, distance from the sample boundary, ...) by using a diffusion/reaction model such as the one proposed by Colin [89–91]. These two steps are essential to characterize the oxidation behavior of a given resin, and thus to provide information to predict the effects of the oxidation on the composite material.

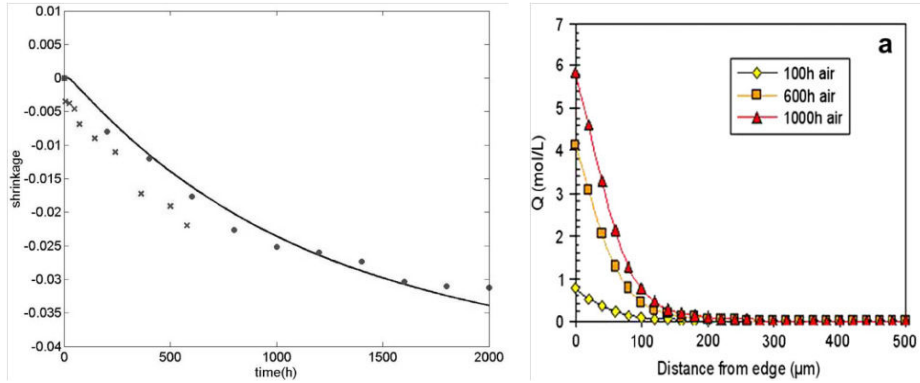


Figure 3.1: (a) Shrinkage of a $70 \mu\text{m}$ matrix film aged at $150 \text{ }^\circ\text{C}$ in air, (x) measured by optical microscopy, (o) calculated from experimental values of weight loss and density increase, (-) calculated with Matlab software [16] (b) Epoxy resin, prediction of the concentration of oxidation products after isothermal aging of different times at $150 \text{ }^\circ\text{C}$, under atmospheric air. [49]

While a lot of information is available in the literature on the oxidation of various epoxy resins, the oxidation behavior of the material considered was still under study. Indeed, the characterization works on our resin were carried out by the project partners in parallel with the present work. For this reason, some pragmatic choices had to be made in order to obtain the homogenized properties which is required in the rest of the study.

The composite specimens considered here were aged in air at $180 \text{ }^\circ\text{C}$ for a maximum duration of 6 weeks. For this reason, a relative concentration of oxidation products (q) is introduced in this work, defined as the ratio between the actual concentration (Q) and the concentration associated to samples aged for 1008 h at $180 \text{ }^\circ\text{C}$ in air (Q_{6w}) :

$$q = \frac{Q}{Q_{6w}} \quad 0 < q < 1 \quad (3.1)$$

A more complex was functional relation between the oxidation level and the matrix elastic modulus E_m identified in a previous study for an epoxy resin such as [49]. But similar information was not available for the material considered in this study. To simplify matters, here we assumed E_m to be a linear function of the relative concentration (q) :

$$E_m = E_{m0}(1 + \beta q) \quad (3.2)$$

where E_{m0} is the Young's modulus of the unaged matrix and β is a non-dimensional coefficient. At an aging condition similar to ours, the project partners have identified a 50% increase of the elastic modulus after 1010 h of aging, which allows us to set $\beta = 0.5$.

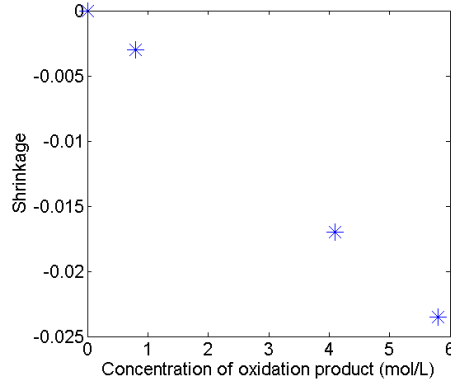


Figure 3.2: Shrinkage versus the concentration of oxidation products

Previous studies on different materials contain information on the shrinkage of thin matrix films, which can be considered to have a uniform oxidation level, versus the time (Figure 3.1(a)). Crossing this information with the oxidation level versus time predicted by the diffusion-reaction model (Figure 3.1(b)), one obtains an almost linear relation between the shrinkage and the oxidation level (Fig. 3.2). A linear relation is thus assumed here:

$$\epsilon_{ox} = \alpha q \quad (3.3)$$

Based on information from the project partners, the non-dimensional shrinkage coefficient α was set to -0.05.

3.3 Homogenization method

A homogenization method is an approach to find the effective properties of physical systems containing two or more length scales [75]. Homogenization methods have been successfully used on various problems including the properties of fiber reinforced composites in conjunction with the finite element method (FEM) [76, 77]. The composite material is assumed to be a repetition of a unit microstructure which is composed of a fiber and the surrounding matrix. The mesoscale properties of the oxidized composite material are obtained by homogenizing the behavior of the unit cell.

3.3.1 Homogenization without the effects of the oxidation aging

The homogenization method for the properties of the unaged composite material is presented following the demonstration in [78]. Consider a composite body occupying a domain Ω whose microstructure is constituted by the repetition of a periodic heteroge-

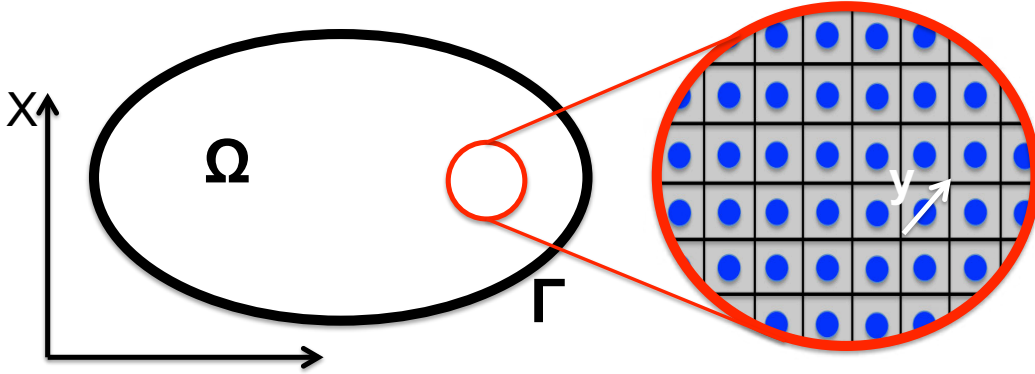


Figure 3.3: Periodic domain with two length scales

neous unit cell. The body is subjected to a system of body forces f . The characteristic length of the composite structure is L and the characteristic length of a unit cell is l . Their ratio ($e = l/L$) is usually very small. x is the coordinate associated to the mesoscale and y is the coordinate associated to the microscopic scale.

The unaged composite material is assumed to behave as a linear elastic material whose constitutive law and equilibrium equation are shown in the following equations

$$\sigma = E\epsilon \quad (3.4)$$

$$\text{div}\sigma = -f_i \quad (3.5)$$

The two-scale asymptotic expansion of the displacement is stated as

$$\begin{aligned} u(x, y) &= u_0(x, y) + eu_1(x, y) + e^2u_2(x, y) + \dots, \\ &= \sum_{i=1}^n e^i u_i(x, y) \quad \text{with } y = \frac{x}{e} \end{aligned} \quad (3.6)$$

The derivative of any functions depending on the two scales is given as

$$\frac{\partial}{\partial x_i}(\Phi(x, y)) = \frac{\partial \Phi}{\partial x_i} + \frac{1}{e} \frac{\partial \Phi}{\partial y_i}, \quad (3.7)$$

The strain tensor is expressed as

$$\begin{aligned}
\epsilon_e &= \frac{1}{2} \left(\frac{\partial u_k}{\partial x_l} + \frac{\partial u_l}{\partial x_k} \right) \\
&= \frac{1}{2} e^{-1} \left(\frac{\partial u_{0k}}{\partial y_l} + \frac{\partial u_{0l}}{\partial y_k} \right) + \frac{1}{2} \left(\frac{\partial u_{0k}}{\partial x_l} + \frac{\partial u_{1k}}{\partial y_l} + \frac{\partial u_{0l}}{\partial x_k} + \frac{\partial u_{1l}}{\partial y_k} \right) + \dots \\
&= \frac{1}{2} e^{-1} \nabla_y u_0(x, y) + \frac{1}{2} \sum_{i=0}^n e^i (\nabla_x u_i(x, y) + \nabla_y u_{i+1}(x, y))
\end{aligned} \tag{3.8}$$

Substituting Eq. (3.8) and Eq. (3.4) in Eq. (3.5), the equilibrium equation can be expressed as

$$\begin{aligned}
&e^{-2} \{ \text{div}_y [E(\nabla_y u_0(x, y))] \} + \\
&e^{-1} \{ \text{div}_y [E(\nabla_y u_1(x, y) + \nabla_x u_0(x, y))] + \text{div}_x [E \nabla_y u_0(x, y)] \} + \\
&e^0 \{ \text{div}_y [E(\nabla_y u_2(x, y) + \nabla_x u_1(x, y))] + \text{div}_x [E(\nabla_y u_1(x, y) + \nabla_x u_0(x, y))] \} + f_i + \\
&\sum_{i=1}^n e^i \{ \text{div}_y [E(\nabla_y u_{i+2}(x, y) + \nabla_x u_{i+1}(x, y))] + \text{div}_x [E(\nabla_y u_{i+1}(x, y) + \nabla_x u_i(x, y))] \} \\
&= 0
\end{aligned} \tag{3.9}$$

The following equations are obtained from the terms of the increasing order of e

$$e^{-2} : \text{div}_y [E \nabla_y u_0(x, y)] = 0 \tag{3.10}$$

$$e^{-1} : \text{div}_y [E \nabla_y u_1(x, y)] = -\text{div}_y [E \nabla_x u_0(x, y)] - \text{div}_x [E \nabla_y u_0(x, y)] \tag{3.11}$$

$$e^0 : \text{div}_y [E \nabla_y u_2(x, y)] = -\text{div}_y [E \nabla_x u_1(x, y)] - \text{div}_x [E(\nabla_x u_0(x, y) + \nabla_y u_1(x, y))] - f_i \tag{3.12}$$

According to the Lax–Milgram theorem, the e^{-2} equation (Eq. (3.10)) contains a solution which leads u_0 to be a function independent of y

$$u_0(x, y) = u_0(x) \tag{3.13}$$

Substituting Eq. (3.13) into the e^{-1} equation (Eq. (3.11))

$$\text{div}_y [E \nabla_y u_1(x, y)] = -\text{div}_y [E \nabla_x u_0(x, y)] \tag{3.14}$$

Thanks to the periodicity in the Y -domain, the integration of the right part of the equation is 0. There is a solution for the equation too, which leads $u_1(x, y)$ to be a linear function of $\nabla_x u_0(x)$ stated as

$$u_1 = \chi(y) \nabla_x u_0(x) \quad (3.15)$$

For the e^0 equation, the integration of the left part of the equation over y is zero using the periodic boundary condition for u_2 . The integration of the right part of the equation is thus null stated as

$$\int_Y -div_y [E \nabla_x u_1(x, y)] - div_x [E (\nabla_x u_0(x, y) + \nabla_y u_1(x, y))] - f_i dy = 0 \quad (3.16)$$

The first term is 0 due to the periodicity in the Y -domain. Substituting Eq. (3.15) into Eq. (3.16) and dividing the equation by $|Y|$, the above equation can be simplified as

$$div_x \frac{1}{|Y|} \int_Y E (1 + \nabla_y \chi(y)) dy \nabla_x u_0(x) = - \frac{1}{|Y|} \int_Y f_i dy \quad (3.17)$$

Comparing Eq. (3.17) with the homogenized equilibrium equation

$$div \Sigma = -\bar{f} \quad (3.18)$$

the homogenized stress in the Ω domain can be expressed as

$$\Sigma = \frac{1}{|Y|} \int_Y E (1 + \nabla_y \chi(y)) dy \nabla_x u_0(x) = H \bar{\epsilon} \quad (3.19)$$

where $\nabla_x u(x)$ is the average strain ($\bar{\epsilon}$) in Ω domain and H is the homogenized stiffness defined as

$$H = \frac{1}{|Y|} \int_Y E (1 + \nabla_y \chi(y)) dy \quad (3.20)$$

To determine H , global average strains ($\bar{\epsilon}$) are imposed on the periodic unit cell. By homogenizing the local stresses, the homogenized global stresses (Σ) can be obtained. Substituting $\bar{\epsilon}$ and Σ into the constitutive relation (Eq. (3.19)), one can obtain the elements of a homogenized stiffness matrix of the unit cell which is also the stiffness of an unaged composite ply.

3.3.2 Homogenization with the effects of the oxidation aging

In the case with the oxidation aging, the local constitutive relation becomes

$$\sigma = E_{ox}[\epsilon(u(x, y)) - \epsilon_{ox}] \quad (3.21)$$

where E_{ox} is the elastic modulus of the aged components, ϵ_{ox} is the oxidation shrinkage and ϵ is the total strain. The equilibrium equation (Eq. (3.5)) is still valid in the case with the oxidation shrinkage. Substituting the asymptotic expansion of the local strain (Eq. (3.8)) and the new constitutive law (Eq. (3.21)) into the equilibrium equation (Eq. (3.5))

$$\begin{aligned} & e^{-2} \{div_y [E_{ox} \nabla_y u_0(x, y)]\} + \\ & e^{-1} \{div_y [E_{ox} (\nabla_y u_1(x, y) + \nabla_x u_0(x, y) - \epsilon_{ox})] + div_x [E_{ox} \nabla_y u_0(x, y)]\} + \\ & e^0 \{div_y [E_{ox} (\nabla_y u_2(x, y) + \nabla_x u_1(x, y))] + div_x [E_{ox} (\nabla_y u_1(x, y) + \nabla_x u_0(x, y) - \epsilon_{ox})]\} + f_i \\ & + \sum_{i=1}^n e^i \{div_y [E_{ox} (\nabla_y u_{i+2}(x, y) + \nabla_x u_{i+1}(x, y))] + div_x [E_{ox} (\nabla_y u_{i+1}(x, y) + \nabla_x u_i(x, y))]\} \\ & = 0 \end{aligned} \quad (3.22)$$

Equations in the increasing order of e are written as follows

$$e^{-2} : div_y [E_{ox} \nabla_y u_0(x, y)] = 0 \quad (3.10)$$

$$e^{-1} : div_y [E_{ox} \nabla_y u_1(x, y)] = -div_y [E_{ox} (\nabla_x u_0(x, y) - \epsilon_{ox})] - div_x [E_{ox} \nabla_y u_0(x, y)] \quad (3.23)$$

$$e^0 : div_y [E_{ox} \nabla_y u_2(x, y)] = -div_y [E_{ox} \nabla_x u_1(x, y)] - div_x [E_{ox} (\nabla_x u_0(x, y) + \nabla_y u_1(x, y) - \epsilon_{ox})] - f_i \quad (3.24)$$

The oxidation shrinkage does not affect the e^{-2} equation (Eq. (3.10)), thus $u_0(x, y)$ is always independent of y . Thanks to $u_0(x, y) = u_0(x)$ and the periodicity in the Y -domain, the the e^{-1} equation can be simplified as the following equation.

$$div_y [E_{ox} \nabla_y u_1(x, y)] = -div_y [E_{ox} (\nabla_x u_0(x) - \epsilon_{ox})] \quad (3.25)$$

which implies the solution of u_1 is in the form as

$$u_1 = \chi(y) \nabla_x u_0(x) - B(y) \quad (3.26)$$

where $\chi(y)$ and $B(y)$ are the solutions of

$$\int_Y div_y [E_{ox} (1 + \nabla_y \chi(y))] dy = 0 \quad (3.27)$$

$$\int_Y \operatorname{div}_y [E_{ox} (\epsilon_{ox} + \nabla_y B(y))] dy = 0 \quad (3.28)$$

For the e^0 equation, the integration of the left part of the equation over y is zero using the periodic boundary condition for u_2 . The integration of the right part of the equation is thus null also.

$$\int_Y \operatorname{div}_y [E_{ox} \nabla_x u_1(x, y)] + \operatorname{div}_x [E_{ox} (\nabla_x u_0(x, y) + \nabla_y u_1(x, y) - \epsilon_{ox})] + f_i dy = 0 \quad (3.29)$$

Thanks to the periodicity in Y , the first term of Eq. (3.29) is null. Then substituting Eq. (3.26) into Eq. (3.29) and dividing by $|Y|$, the above equation can be simplified as

$$\operatorname{div}_x \frac{1}{|Y|} \int_Y [E_{ox} (1 + \nabla_y \chi(y)) \nabla_x u_0(x) - E_{ox} (\epsilon_{ox} + \nabla_y B(y))] dy = -\frac{1}{|Y|} \int_Y f_i dy \quad (3.30)$$

The above equation is comparable with the equilibrium equation

$$\operatorname{div} \Sigma = -\bar{f} \quad (3.18)$$

where

$$\Sigma = \frac{1}{|Y|} \int_Y E_{ox} (1 + \nabla_y \chi(y)) \nabla_x u_0(x) - E_{ox} (\epsilon_{ox} + \nabla_y B(y)) dy \quad (3.31)$$

According to the Eq. (3.20), the homogenized stiffness of the oxidized composite materials can be state as

$$H_{ox} = \frac{1}{|Y|} \int_Y E_{ox} (1 + \nabla_y \chi(y)) dy \quad (3.20)$$

Considering

$$C = \frac{1}{|Y|} \int_Y E_{ox} (\epsilon_{ox} + \nabla_y B(y)) dy \quad \text{and} \quad \bar{\epsilon}_{ox} = H^{-1} C \quad (3.32)$$

and substituting Eq. (3.20) and Eq. (3.32) into Eq. (3.31)

$$\Sigma = H_{ox} (\bar{\epsilon} - \bar{\epsilon}_{ox}) \quad (3.33)$$

The two effects (increase of the elastic modulus and shrinkage) of the oxidation aging can be calculated in two steps. First, to obtain the homogenized stiffness of the

aged composite materials, the volume of the aged matrix is assumed to be unvaried, which means the homogenized shrinkage due to the oxidation aging ($\bar{\epsilon}_{ox}$) in Eq. (3.33) is 0. The above equation can be simplified as

$$\Sigma = H_{ox}\bar{\epsilon} \quad (3.34)$$

H_{ox} is resolved with the same method used in the case of the unaged composite material. Second, the shrinkage in the oxidized matrix is taken into account and $\bar{\epsilon}$ is assumed to be 0. The homogenized shrinkage of the aged composite material ($\bar{\epsilon}_{ox}$) is thus solved by substituting the homogenized stress (Σ) and the homogenized stiffness (H_{ox}) into Eq. (3.35).

$$\Sigma = -H_{ox}\bar{\epsilon}_o \quad (3.35)$$

3.3.3 FEM calculations of a unit cell of composite materials

The Finite Element Method (FEM) has been successfully used in the application of the homogenization theory in the studies on composite materials [76, 77]. In this section, a FEM model of a unit cell of the composite material at the fiber/matrix scale is developed with ABAQUS. The properties of the unaged composite material are firstly studied. Then the increase of Young's modulus and the shrinkage of the oxidized matrix, which are functions of the oxidation level (q), are introduced in the micro-scale models to provide the necessary micro-scale information for the presented homogenization method.

3.3.3.1 Modelling of a unit cell of unaged composite materials

A composite material ply is considered to be the repetition of a cubic unit cell which is taken out and modeled (Fig. 3.4(a)). According to the information provided by the project partners, fibers account for 66% of the mass fraction of the studied material. Considering the fiber density as 1700 kg/m^3 and the epoxy matrix density as 1200 kg/m^3 , fibers account for about 55% of the volume fraction. The diameter of fibers is measured as $5 \text{ }\mu\text{m}$ with a microscope, which leads the edge of the cubic cell to be about $6 \text{ }\mu\text{m}$. The mesh at the fiber/matrix interphase is refined and the contact at the fiber/matrix interface is assumed to be perfectly bonded and is free of friction.

The boundary condition is an essential problem for a numerical study on the unit cell. In our study, nodes on one surface are constrained with the nodes on the opposite surface to impose the periodic condition and a global strains ($\bar{\epsilon}$) to the unit cell. Furthermore, generalized plane strain is assumed in the direction parallel to the fibers in order to simulate the behavior of the composite material away from the edges.

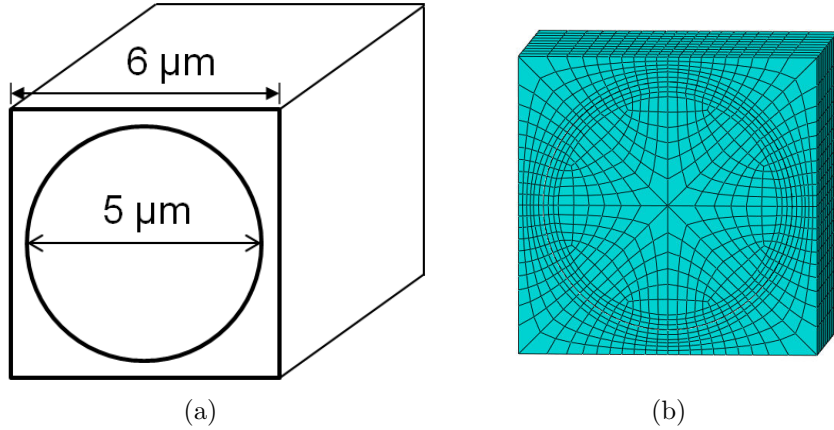


Figure 3.4: (a) Geometry and (b) Mesh of a unit cell

The properties of the fibers and the matrix are also important issues in this study because the properties of the composite material depend on the properties of its components. The matrix is modeled as a linear elastic and isotropic material. The properties of the unaged matrix are given in Tab. 3.1. The Young's modulus of the unaged matrix (E_{m0}) was identified experimentally by the project partners. Different identification methods (ultra micro indentation, dynamic mechanical analysis, atomic force microscopy, tensile tests) result in a variation of about 50%. The E_{m0} applied to the fiber/matrix scale model is the average of all the results. The Poisson's ratio is referenced from a similar matrix in the literature [80].

Table 3.1: Properties of the unaged matrix in the FEM calculations

Young's modulus E_m (GPa)	Poisson's ratio ν_m
3.3	0.35

Carbon fibers are modeled as a linear elastic and transverse isotropic material. The five independent elastic parameters are shown in Tab. 3.2. The exact properties of the fibers of our material are unknown. So the longitudinal modulus is considered to be the same as an industrial HTS carbon fiber (T300) which is 230 *GPa* [79]. There is an important variation of the transverse modulus of fibers (E_2) in the literature. E_2 identified experimentally with ultrasonic scattering [81] or the nano-indentation technique [82, 83] is generally between 5~14 *GPa*, but the value identified analytically with mixture laws or numerically with homogenization methods vary between 25~30 *GPa* [84]. As it is the simulations that are carried out in this section, E_2 is considered to be 30 *GPa*. Furthermore, this value is consistent with the transverse modulus calculated with a model based on the orientations of carbon crystals [85]. The rest of the parameters are taken from the literature [80].

Table 3.2: Fiber properties in the FEM calculations

E_1 (GPa)	E_2 (GPa)	G_{12} (GPa)	ν_{12}	ν_{23}
230	30	15	0.3	0.455

3.3.3.2 Introducing the oxidation effects into the micro-scale models

The two effects of the oxidation aging on the matrix are introduced into the micro-scale model. q is considered to be homogenous in the matrix of a unit cell. Although the oxidation aging is a non-homogeneous phenomenon on composite plies, since the dimension of a unit cell is very small compared with the general distance of the oxygen diffusion ($\approx 150 \mu m$), the variation of q within a unit cell is almost negligible. The behavior of an oxidized unit cell is calculated point by point at different levels of q . The Young's modulus and the shrinkage of the oxidized matrix at different oxidation levels are shown in Tab. 3.3.

Table 3.3: Matrix modulus and shrinkage versus q

q	0	0.2	0.4	0.6	0.8	1
E_m (GPa)	3.3	3.63	3.96	4.29	4.62	4.95
ϵ_{ox}	0 %	-1 %	-2 %	-3 %	-4 %	-5 %

3.4 Stress field around fibers

At the micro scale, the two effects of the oxidation aging on the matrix generate an important stress field around the fibers. Fig. 3.5(a) show the radical stress field at the polar coordinate system of an unit cell aged for 6 weeks with the total average strain ($\bar{\epsilon}$) is 0. The entire periodic cell suffers a significant tensile stress field in the polar coordinates. Thanks to the symmetry of the model geometry and of the stress field, normal stresses along only a quarter of the interface have been plotted (Fig. 3.5(b)). The zone which is rich in the matrix possesses a higher tensile stress. Since the interface is considered to be perfectly bonded, the stress at the interface reaches about 500 MPa. In reality, the fiber/matrix debonding can be expected at this level of stress.

This result confirms the tensile stress field around the fiber/matrix interface which has been documented in the literature [18,92]. A non-tensile stress field under the matrix shrinkage determined by other researchers (Fig. 3.6) [93] can be probably attributed to be the wrong boundary conditions imposed on the unit cell.

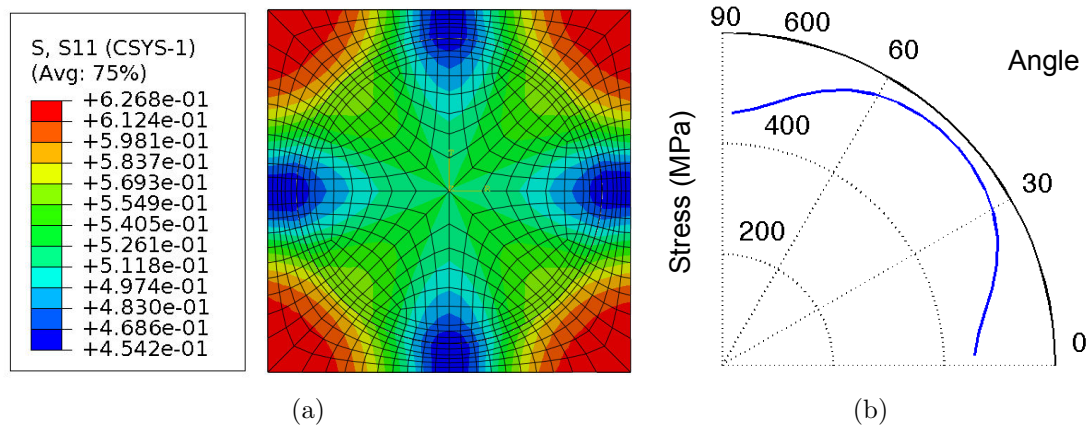


Figure 3.5: (a) Stress field in the polar coordinate system of samples aged for 6 weeks(Gpa) (b) Stresses along one quarter of the fiber/matrix interface

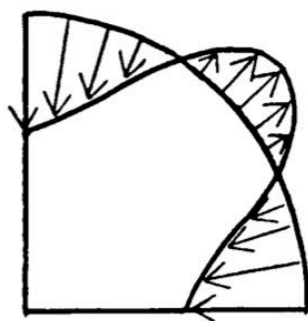


Figure 3.6: Non-tensile stress field around the fiber/matrix interface due to the residual thermal shrinkage according to [93]

3.5 Homogenized properties of composite materials

3.5.1 Stiffness of unaged composite materials

Via the homogenization method presented in the previous sections and the associated FEM calculations, the homogenized stiffness matrix of an unaged composite ply, is obtained as

$$H = \begin{bmatrix} 128.97 & 4.21 & 4.21 & 0 & 0 & 0 \\ 4.21 & 13.21 & 6.05 & 0 & 0 & 0 \\ 4.21 & 6.05 & 13.21 & 0 & 0 & 0 \\ 0 & 0 & 0 & 3.41 & 0 & 0 \\ 0 & 0 & 0 & 0 & 3.41 & 0 \\ 0 & 0 & 0 & 0 & 0 & 2.63 \end{bmatrix} GPa \quad (3.36)$$

According to the Hooke's law of transverse isotropic material,

$$\begin{pmatrix} \epsilon_{11} \\ \epsilon_{22} \\ \epsilon_{33} \\ \gamma_{12} \\ \gamma_{13} \\ \gamma_{23} \end{pmatrix} = \begin{pmatrix} \frac{1}{E_1} & -\frac{\nu_{12}}{E_1} & -\frac{\nu_{13}}{E_1} & 0 & 0 & 0 \\ -\frac{\nu_{12}}{E_1} & \frac{1}{E_2} & -\frac{\nu_{23}}{E_2} & 0 & 0 & 0 \\ -\frac{\nu_{13}}{E_1} & -\frac{\nu_{23}}{E_2} & \frac{1}{E_2} & 0 & 0 & 0 \\ 0 & 0 & 0 & \frac{1}{G_{12}} & 0 & 0 \\ 0 & 0 & 0 & 0 & \frac{1}{G_{12}} & 0 \\ 0 & 0 & 0 & 0 & 0 & \frac{2(1+\nu_{23})}{E_2} \end{pmatrix} \cdot \begin{pmatrix} \sigma_{11} \\ \sigma_{22} \\ \sigma_{33} \\ \tau_{12} \\ \tau_{13} \\ \tau_{23} \end{pmatrix} \quad (3.37)$$

The elastic properties of the unaged composite ply are obtained as shown in Tab.3.4.

Table 3.4: Homogenized material properties of an unaged composite ply

E_1 (GPa)	E_2 (GPa)	G_{12} (GPa)	ν_{12}	ν_{23}
127.13	10.39	3.41	0.22	0.45

where E_1 is the axial elastic modulus, E_2 is the transverse elastic modulus, G_{12} is the in-plane shear modulus, ν_{12} and ν_{23} are the Poisson's ratios.

3.5.2 Elastic modulus of aged composite materials

Due to the variation of the Young's modulus of the aged matrix (Tab. 3.3), the properties of the aged composite materials vary with the oxidation levels also (Tab. 3.5). The longitudinal modulus is almost unvaried as it is driven by the longitudinal modulus of the fibers which is unaffected by the oxidation aging. However, the transverse modulus and the shear modulus increase slightly nonlinearly with the increase of the aging time (Fig. 3.7). They increased respectively 30% and 36% after an aging of 1008 h in air at 180 °C.

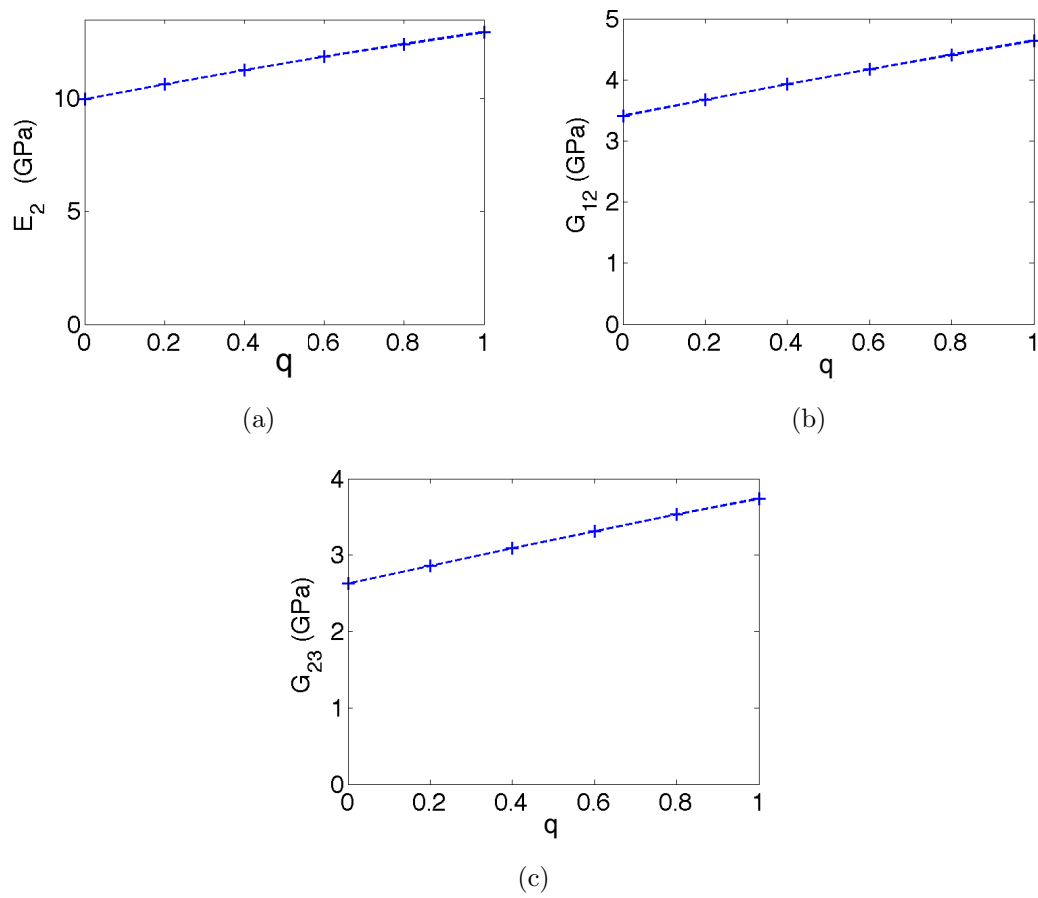


Figure 3.7: Homogenized (a) transverse modulus (b) in-plane shear modulus (c) out-of-plane shear modulus versus the relative concentration of oxidation products

Table 3.5: Elastic properties of the oxidized composite material at different levels of q

q	0	0.2	0.4	0.6	0.8	1
E_1 (GPa)	127.13	127.32	127.50	127.71	127.90	128.10
E_2 (GPa)	10.39	11.10	11.78	12.42	13.04	13.63
G_{12} (GPa)	3.41	3.67	3.93	4.17	4.41	4.64
G_{23} (GPa)	2.63	2.86	3.09	3.31	3.53	3.74
ν_{23} (GPa)	0.453	0.462	0.470	0.479	0.486	0.493

3.5.3 Shrinkage of aged composite materials

Given the homogenized stiffness of the oxidized composite material, the homogenized shrinkage obtained by Eq. (3.35) is shown in Tab. 3.6. Shrinkage hardly exists along the fiber direction of a composite ply, because the longitudinal strain of the composite material is dominated by the fibers of high longitudinal modulus. However the oxidized composite material possesses important shrinkage in the transverse direction.

Table 3.6: Shrinkage of composite material versus matrix modulus

q	0	0.2	0.4	0.6	0.8	1
ϵ_{11}	0 %	0.00 %	0.00 %	0.00 %	0.00 %	0.00 %
ϵ_{22}	0 %	0.46 %	0.91 %	1.36 %	1.80 %	2.23 %

3.6 Discussion

In this chapter, the elastic modulus and the shrinkage of the oxidized composite ply for several given oxidation levels (q) are obtained via a homogenization method. These properties can be used either to fit with mathematical correlations, for example the modified mixture laws [94], or to predict directly the elastic modulus and the shrinkage at any oxidation levels with the interpolation method. The predicted properties are going to be used in the following meso-scale experimental or numerical studies where q is not homogeneous within a ply.

The micro-scale model has also confirmed the tensile stress field at the fiber/matrix interface. An further exploration of the damage mechanisms at the interface zone could be carried out.

Normally, it is difficult to identify directly the meso-scale properties of the oxidized composite material since the oxidation aging is a non-uniform local phenomenon whose mechanisms affect at a smaller scale. However, the presented homogenization method

enabled us to carried out a numerical identification, which makes it become a useful method in the study of the oxidation aging.

It also needs to note that the homogenized properties of composite materials depend strongly on the properties of its components. In the lack of the knowledge of our material, the properties of similar materials in literature and some simplification have to be performed in this fiber/matrix scale study. Properties and variations may be predicted with errors compared to the reality, but these errors could be corrected once the exact properties and oxidation process are available. Furthermore, the model does not take into account the possible interface degradation generated by the important stress field around the fibers which may result in an overestimation of the effective modulus.

Chapter 4

Experimental characterization of the mechanical behavior of oxidized composite specimens

Contents

4.1	Introduction	72
4.2	Material and aging conditions	72
4.3	Quasi-static tensile test	73
4.3.1	Test setup	73
4.3.2	Digital image correlation (DIC)	74
4.3.3	Evaluating the kinetics of transverse cracking with DIC	76
4.3.4	Results	80
4.4	Non-destructive free vibration tests	83
4.4.1	Identification of the transverse modulus by vibration tests	83
4.4.2	Modeling of the free vibration tests	85
4.5	Conclusion	87

4.1 Introduction

The aim of this chapter is to characterize experimentally the effect of the oxidation aging on the mechanical behavior of composite specimens. The elastic and damageable behavior of an elementary ply can be easily identified for the unaged specimens starting from simple tests on a few basic stacking sequences. In aged composites, on the other hand, the effect of oxidation is often limited within a thin surface layer, thus making it more difficult to characterize the behavior of the oxidized material.

In Chapter 3, the periodic homogenization was used to calculate the properties of our material as functions of the oxidation level, taking into account the shrinkage and increase in elastic modulus of the matrix. This model, however, does not account for the presence of damage, for example the fiber/matrix debonding. Experimental information on the elastic modulus of the oxidized layer would allow to indicate the presence of damage mechanisms and to evaluate its effect as compared to the modification of the matrix elastic properties.

The presence of oxidation may also lead to a different damage evolution with respect to the unaged specimens. In particular, the shrinkage and the weakening effect of the oxidized layer may facilitate the appearance of transverse cracks, such as the partial cracks observed in Chapter 2. Experimental data on the crack density evolution for the aged and the unaged specimens would allow to understand and quantify the interaction between the oxidation and the transverse cracking.

Two types of tests are carried out in order to gather experimental information on the elastic modulus and on the transverse cracking evolution of the oxidized composite specimens. Tensile tests on the aged and the unaged $[90/0]_s$ samples allow to characterize the crack density evolution of the samples aged for different times. Digital Image Correlation (DIC) was used to measure the local strain within the specimen and a procedure for automatic crack counting was developed. While the crack density evolution was found to vary significantly with the oxidation level, no appreciable difference was detected in the elastic behavior between the aged and the unaged samples, because it is dominated by the unaffected 0° plies. In order to increase the participation of the outer oxidized layers in the global response of the specimen, non destructive free vibration tests were carried out on the same samples, allowing to obtain qualitative information on the elastic properties of the oxidized layer.

4.2 Material and aging conditions

The material used in this study was presented in Chapter 2. The sequence of the laminated composite plate was chosen to be $[90/0]_s$. The measured total thickness of the plate was about 0.52 mm containing four plies of 0.14 mm thick. The plate was cut

into samples whose dimensions are 180 mm (L) \times 20 mm (W) \times 0.52 mm (H) with a water jet cutter which allows to reduce the scraped material and damage during cutting process. Zones of 40 mm on both ends of samples were reserved for the jaws of the hydraulic machine and bonded with composite tabs. The effective length is thus 100 mm as shown in Fig. 4.1. The samples were dried at $70\text{ }^\circ\text{C}$ for 7 days, then divided into 4 groups. Each group contains three samples. One group was kept directly in a vacuum desiccator with the calcium chloride inside. The other groups were kept in the same desiccator after aging of 168 h (1 week), 504 h (3 weeks) and 1008 h (6 weeks) at $180\text{ }^\circ\text{C}$ in an oven. The same samples are subjected to non destructive free vibration tests and then to tensile tests.

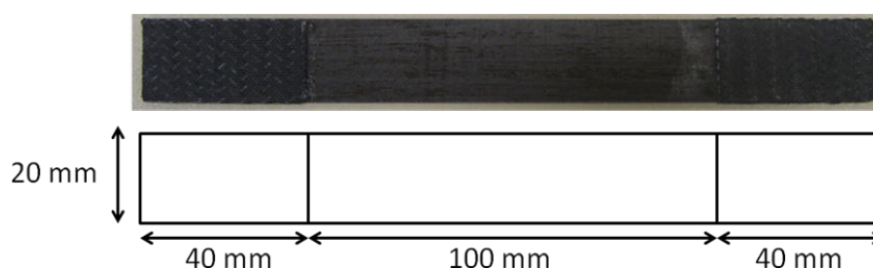


Figure 4.1: Dimension of $[90/0]_s$ samples of HTS/TACTIX material

Cross-ply specimens with stacking sequences of $[90_m/0_n]_s$ and $[0_n/90_m]_s$ are usually used to evaluate the crack density evolution [95,96,105]. In our test, the sequence $[90/0]_s$ has been chosen for two reasons. First, the 90° plies, in which transverse cracking occurs, are the external plies and thus they are exposed directly to the oxidative environment. Second, the overall laminate thickness is kept small in order to maximize the effect of the oxidized layer on the global specimen behavior.

4.3 Quasi-static tensile test

4.3.1 Test setup

The tensile tests are carried out with an INSTRON MTS 810 material testing system at environmental temperature, $20\text{ }^\circ\text{C}$. The experimental setup of the tests is shown in Fig. 4.2.

The tensile test is displacement controlled at a rate of $1\text{ mm}/\text{min}$. Digital Image Correlation (DIC) is used to capture both the global strain and the crack density evolution. A speckle pattern is painted on both sides of the specimen and two CCD cameras ($3000\text{ Pixels} \times 4000\text{ Pixels}$) with objectives (Sigma 105 1 : 2.8D) are set against each of the two surfaces, taking pictures at a frequency of 1 photo/1.5 second. One camera takes pictures of the entire surface of the sample: these are referred to as global

pictures and they provide the average longitudinal strain (Fig. 4.3(a)). The other takes pictures of a zone of $20\text{ mm} \times 20\text{ mm}$: these are referred to as local pictures and they allow us to count the number of cracks thanks to an automatic post-treatment of the DIC results (Fig. 4.3(b)).

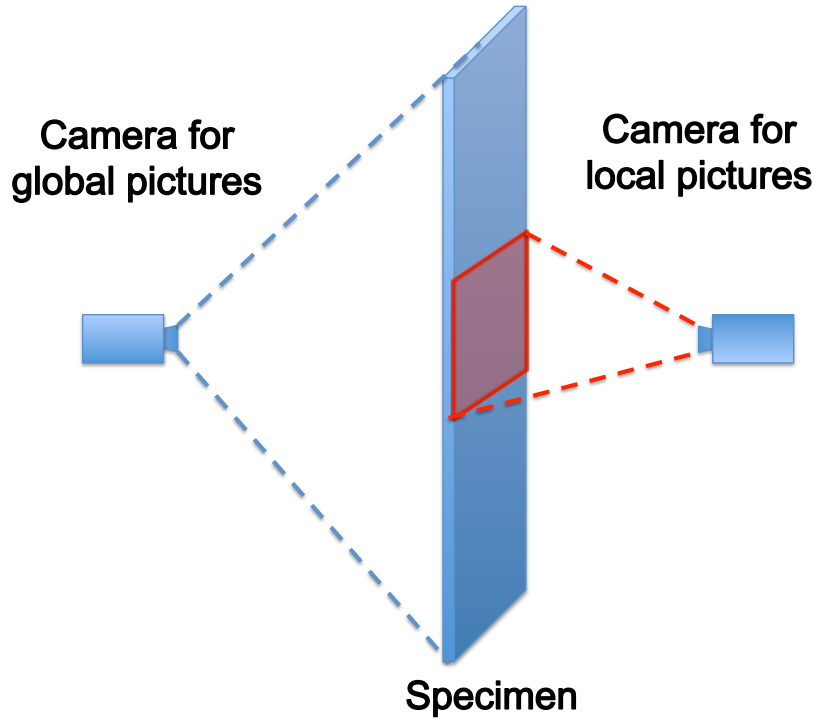
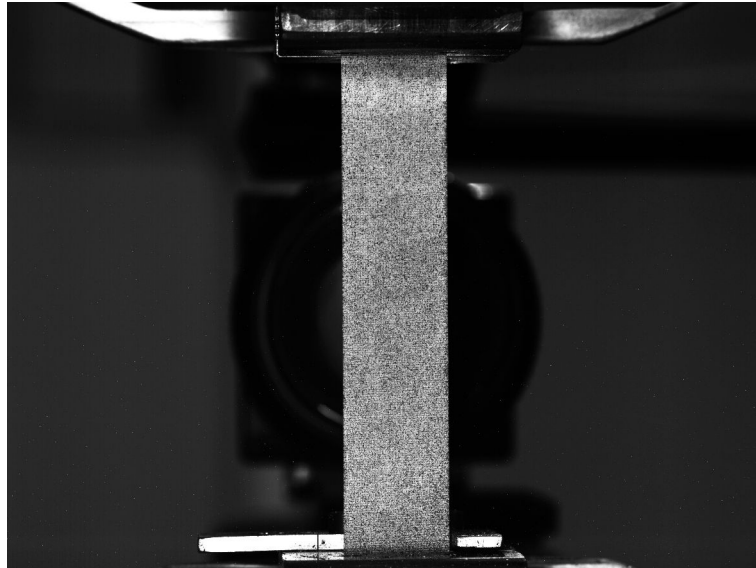


Figure 4.2: Setup of tensile test

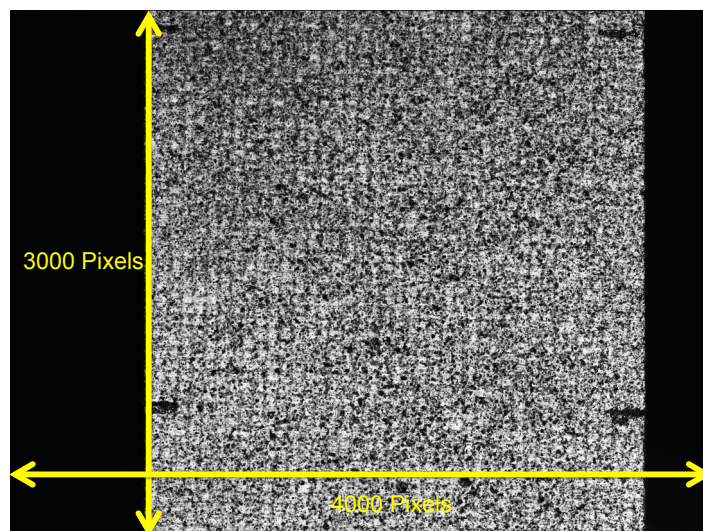
4.3.2 Digital image correlation (DIC)

Digital image correlation (DIC) is a technique to measure 2D and 3D displacement fields as well as other parameters by matching images [98–100]. The DIC method has been successfully used to measure the propagation of cracks [101] or to estimate the crack opening displacements [102]. In our study, cracks are detected and counted by analyzing the strains measured by DIC.

To determine the displacement field, an image is considered to be composed of many sub-images which is called a zone of interest (ZOI). Each ZOI contains several pixels and an intensity information called the gray level. To estimate the displacement of a ZOI, the positions of a ZOI in two images are tracked. As explained in [100], considering $f(x)$ the intensity information of a reference ZOI and $g(x)$ the intensity information of ZOIs on a deformed image, one has



(a)



(b)

Figure 4.3: (a) Global picture (b) Local picture

$$g(x) = f[x + u(x)] \quad (4.1)$$

where $u(x)$ is the unknown displacement field which allows to relate the ZOIs in the two images. Assuming that the intensity information of the reference image are differentiable, the expansion of $g(x)$ to the first order is stated as

$$g(x) = f(x) + u(x) \cdot \nabla f(x) \quad (4.2)$$

The displacement u can be obtained by minimizing the difference between $f(x + v)$ and $g(x)$

$$\min ||g(x) - f(x) - v(x) \nabla f(x)||^2 \quad (4.3)$$

where v is a trial displacement. The strains are calculated from the deformation gradient tensor F and a vector dx_0

$$dx = F dx_0 \quad (4.4)$$

F is related to the displacement gradient ∇u by

$$F = I + \nabla u \quad (4.5)$$

where I is the second order identity tensor. The strain tensor ϵ is defined as

$$\epsilon = \frac{1}{2} [\nabla u + (\nabla u)^t] \quad (4.6)$$

For example, Fig. 4.4 shows the measured longitudinal strain of a sample, which in this case is constant over a ZOI.

4.3.3 Evaluating the kinetics of transverse cracking with DIC

To evaluate the crack density evolution, the average longitudinal strain on the specimen (ϵ_a) and the number of cracks should be measured as a function of time. In these tests, ϵ_a is obtained by averaging the strains of all the ZOIs on a global picture and the number of cracks is evaluated from the DIC result of local pictures.

Cracks are the cause of a discontinuity in the displacement field. In the DIC approach presented here, which assumes a continuous displacement, cracks appear as zones in which the strain is higher than the average. An example is given in Fig. 4.5, which shows the DIC results of three local pictures under increasing load. On Fig. 4.5(a),

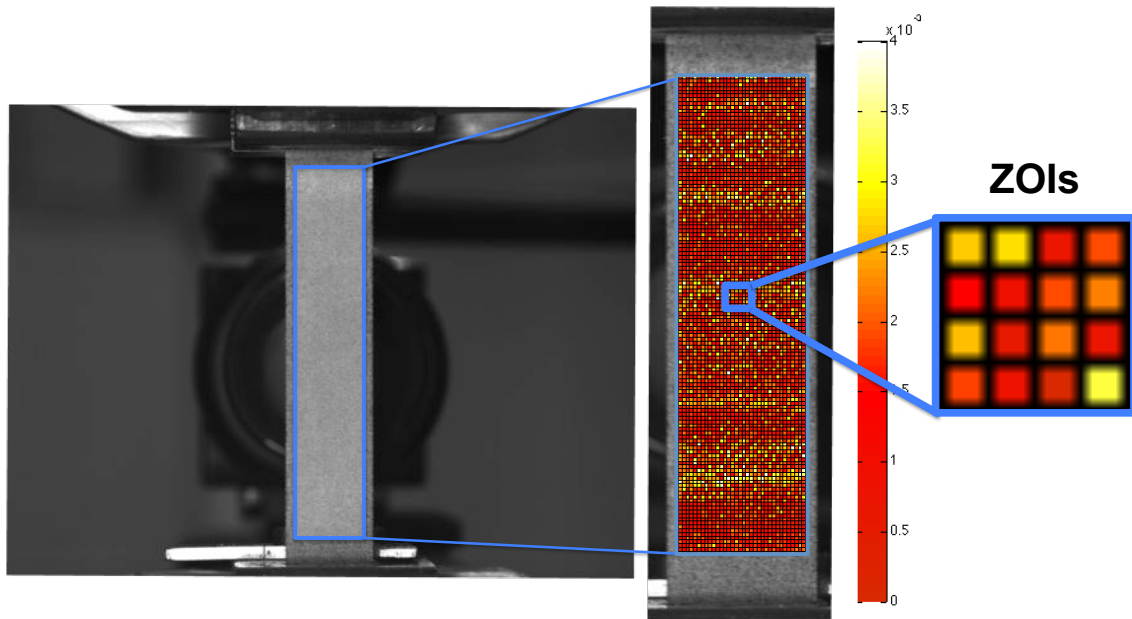


Figure 4.4: The longitudinal strain field composed every ZOIs on a sample surface

no cracks have appeared yet. On Fig. 4.5(b), two cracks have appeared and another has initiated from the left edge. It crosses the entire width of the sample later on Fig. 4.5(c).

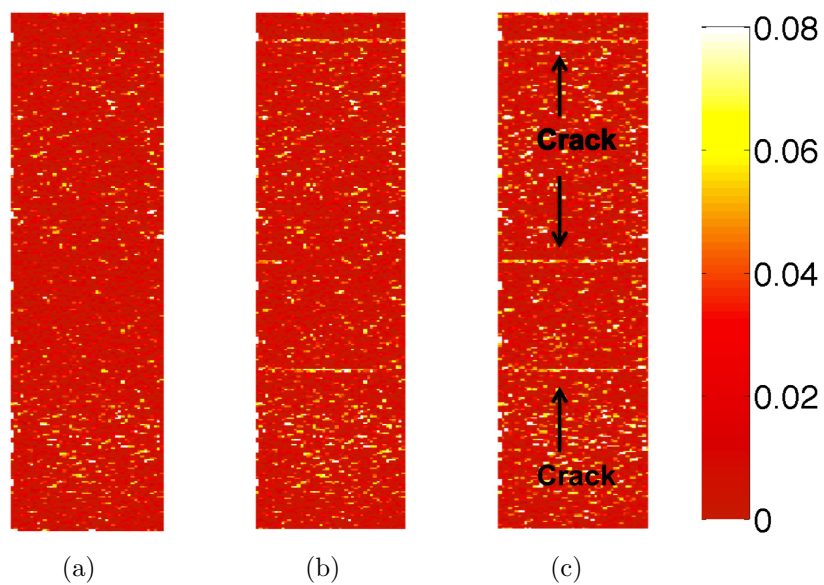


Figure 4.5: DIC results of local pictures for increased loading at the average longitudinal strain of (a) 0.29% (b) 0.32% (c) 0.34%

In order to obtain a correct evaluation of the crack density from DIC, the spatial resolution (related to the pixel size and to the ZOI size) should be at least smaller than the minimum distance between two cracks. Furthermore, the crack opening should be wide enough to make a significant difference on the measured local strain, and thus to be distinguished from other sources of variability and noise.

In these tests, the minimum distance between cracks is estimated based on an expected saturation of crack density of $\rho_s = 0.7$ (a typical value for unaged samples). According to the definition of $\rho = h/D$ (Eq. (1.6)), the average distance between two cracks is around $450 \mu m$. 3000 pixels are laid along a length of about $20 mm$ on the local pictures (Fig. 4.3(b)), which leads each pixel to represent a zone of about $6.6 \mu m \times 6.6 \mu m$. A ZOI in this study is set to be a zone of 8 pixels \times 8 pixels, which leads each ZOI to represent a region of $53 \mu m \times 53 \mu m$. Nine or eight ZOIs can be laid along the average distance between two cracks (Fig.4.6) which is fine enough to count the cracks on the unaged samples or a higher crack density due to the oxidation aging.

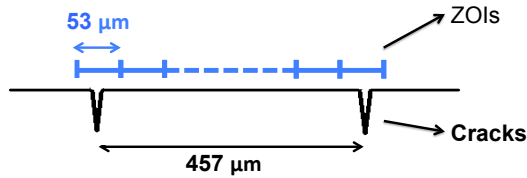


Figure 4.6: Size of ZOI compared with the maximum crack density

In order to distinguish the variations of longitudinal strain due to cracks from other sources of variation and noise (e.g., photo noise, readout noise, dark current noise for CCD cameras [103]), a threshold Δ is introduced as follows (see also Fig. 4.7)

$$\epsilon_{crack} > \epsilon_a + \Delta \quad (4.7)$$

The number of cracks of one column of ZOIs is obtained by counting the peaks of the longitudinal strains which overpass the sum of ϵ_a and Δ .

The threshold should be higher than the oscillations of noises but lower than the high strain due to cracks so that information will not be polluted by noises or covered by a too high threshold. Different values of the threshold were tested (Fig. 4.8(a)) and compared to direct observation of the cracks on the local photos (Fig. 4.9): finally, a value of $\Delta = 0.08$ was retained and used for the analysis of all samples. Furthermore, since in this type of tests cracks generally traverse the entire width of the sample, the number of cracks retained on a sample is the average of the results of three columns of ZOIs which are located respectively in the left, the right and the middle part of the analyzed zone (Fig. 4.8(b)). Even so, cracks with a very small opening displacement (such as the partial cracks observed in Chapter 2 on specimens aged 6 weeks) may not be detected with this method.

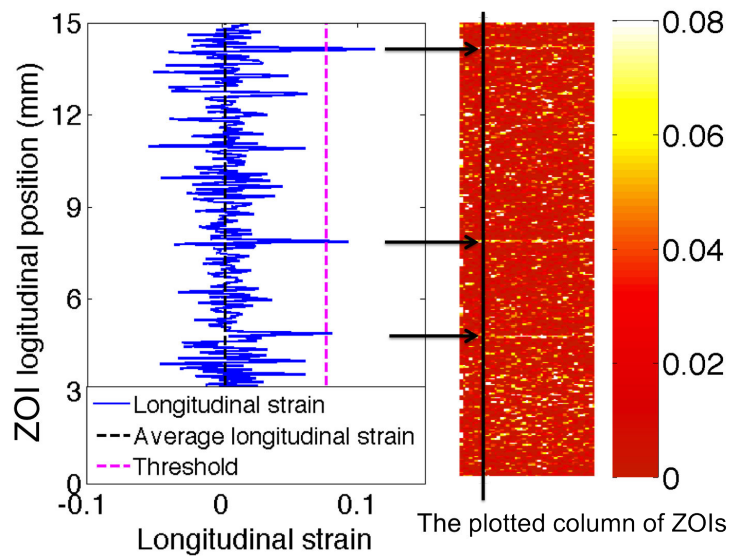


Figure 4.7: Longitudinal strains of one column of ZOIs versus their longitudinal positions

The detection method described here has been automated to analysis a series of photos taken during an entire tensile process to obtain the crack density evolution.

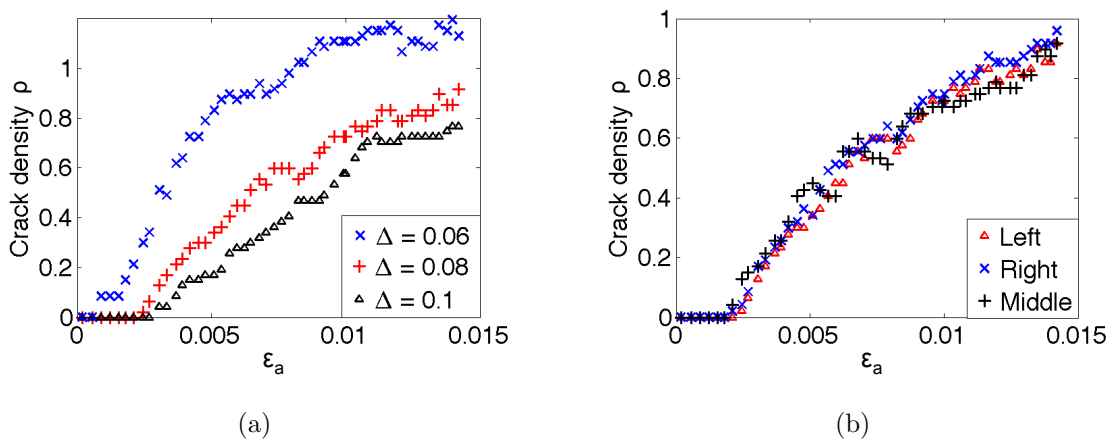


Figure 4.8: Analysed crack density evolutions (a) with different thresholds (b) of three columns of ZOIs

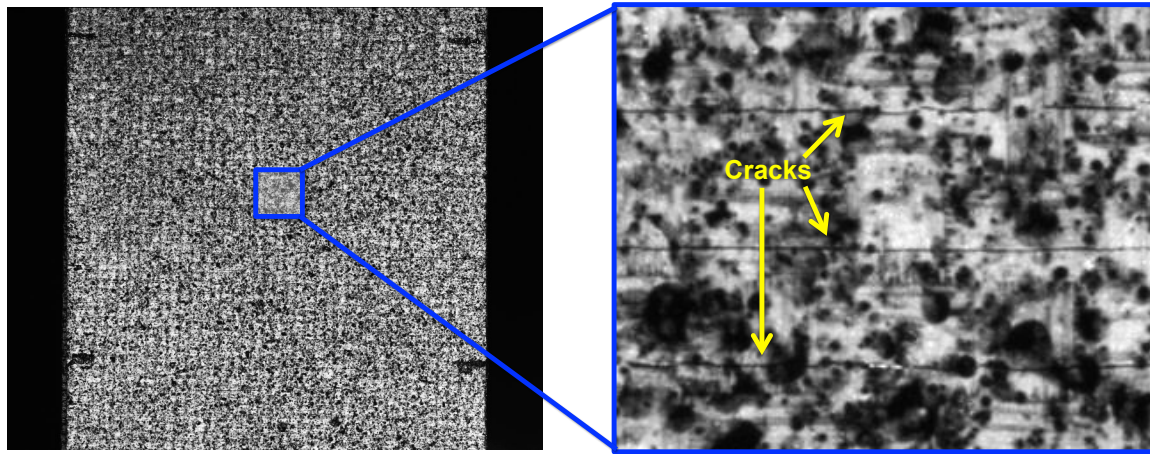


Figure 4.9: Optical observations on zoomed local photos

4.3.4 Results

4.3.4.1 Global behavior of the aged and the unaged specimens

Fig. 4.10 shows the average stress provided by the material testing system as a function of the average longitudinal strain, where the average longitudinal strain is obtained from the global pictures with DIC. The global behavior of the aged and the unaged specimens is analogous because the longitudinal modulus of $[90/0]_s$ composite laminates is controlled by the longitudinal modulus of 0° plies, which is stable under oxidation aging. A slight non-linearity at the beginning of each tensile process is attributed to the fiber realignment.

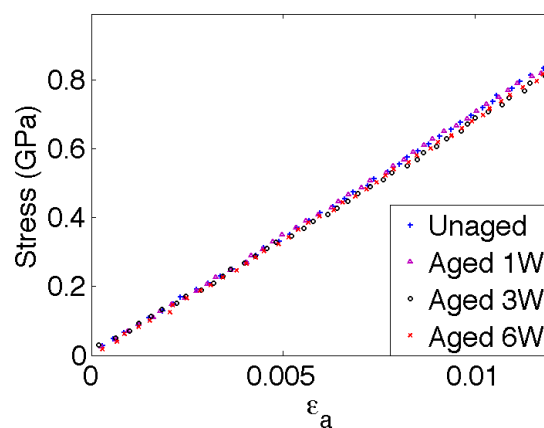


Figure 4.10: Tensile stress as functions of average longitudinal strains

The longitudinal moduli of the laminated composites aged for different times ($E_{x,lam}$) are obtained by measuring the slopes of the data as shown in Tab. 4.1. The relative

variations of the longitudinal modulus of the laminated composites ($\frac{E_{x,lam} - E_{x,lam0}}{E_{x,lam0}}$) are not larger than the variability of the tests on the same group of specimens. For this reason, the effect of oxidation aging on the elastic properties cannot be detected with these tests. Free vibration tests on the same specimens are considered instead.

Table 4.1: Longitudinal modulus of laminated composites aged for different time

Aging time	0 h	168 h (1W)	504 h (3W)	1008 h (6W)
$E_{x,lam}$ (GPa)	69.90 \pm 2.5%	68.10 \pm 3.9%	68.97 \pm 5.6%	67.43 \pm 5.4%
Relative variation of $E_{x,lam}$		-2.6%	-1.4%	-3.5%

4.3.4.2 Crack density evolution

Fig. 4.11 shows the evolutions of crack densities as a function of the average strain for unaged samples (Unaged) and samples aged respectively 168 h (Aged 1W), 504 h (Aged 3W) and 1008 h (Aged 6W) at 180 °C. The DIC results of two samples and the optical observations of one sample within the same group are given to validate the automatic post-treatment base on DIC analysis. The DIC results of the unaged samples and of the samples aged for 168 h and 504 h have a good precision within each group and a good consistency with the optical observations. Due to the quality of the surface painting, only one sample aged for 1008 h has been successfully explored with DIC.

In spite of the fact that cracks crossing the oxidized layer have been observed on the samples aged for 6 weeks in Chapter 2, no cracks have been detected by DIC at the beginning of the tensile test. As it has been anticipated, the opening of these cracks is very small and it can not be detected by our automaticDIC procedure. During the tensile test, some cracks crossing the oxidized layer continue to open or to propagate throughout the entire ply. The increase of the crack opening enabled the cracks to be detected by DIC, which is the reason why the crack density increased more sharply at the low average longitudinal strain on the sample aged for 6 weeks (Fig. 4.11(d)). The interpretation will be further discussed and demonstrated quantitatively in the following chapter by numerical studies. A lower threshold may allow to detect the cracks crossing the oxidized layer, but noises will not be distinguished from the cracks. At last, it is decided to use the same threshold in the post-treatment of all the samples, which allows us to compare the kinetics of the cracks crossing the entire ply.

Fig. 4.12 shows the crack density evolutions of one sample of each group. Cracks of the aged samples initiate at lower average longitudinal strains than the unaged sample. Moreover, the critical longitudinal strain decreases and the crack density increases with the increase of the aging time.

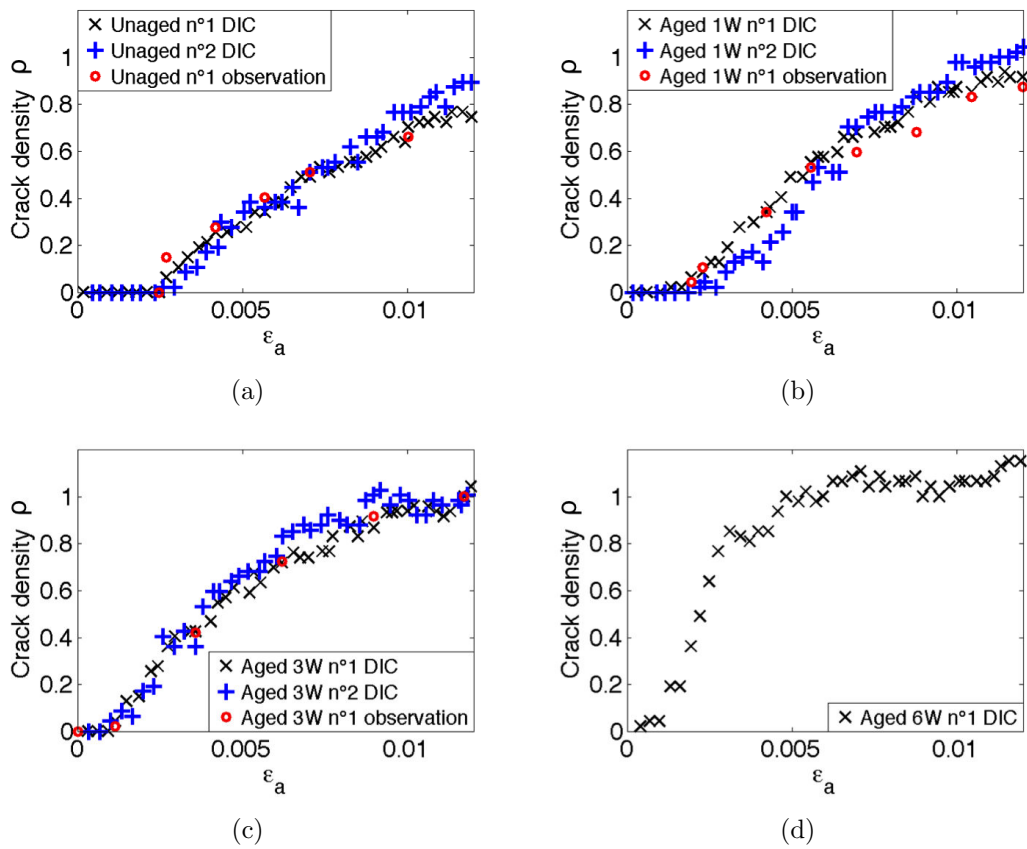


Figure 4.11: Crack density evolutions as a function of the average longitudinal strain of samples (a) unaged (b) aged for 1 week (c) aged for 3 weeks (d) aged for 6 weeks

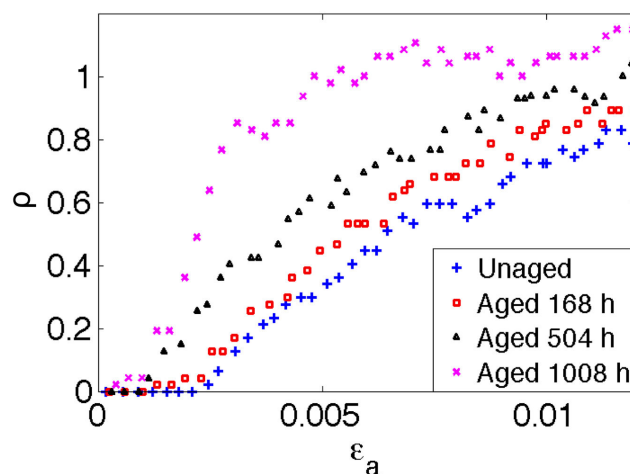


Figure 4.12: Crack density evolutions as functions of the average longitudinal strain

The crack density evolution of an oxidized cross-ply laminate has been also studied in a previous study [55]. In that case, cracks on the aged samples also initiate earlier than on the unaged samples, however, the crack density evolutions in the 90° ply of the samples aged at the same temperature are almost identical no matter the aging times. The different observations can be attributed to the different position of the 90° plies within the stacking sequence. In [55], the sequence of the samples is $[0/90]_s$, thus oxidation affects the whole thickness of the ply, but only on the ply edges. Furthermore, the thickness of the inner double 90° ply is around 0.5 mm . The cracking phenomenon of thick plies depends on the initiation of cracks which is driven by a critical stress. In the present case, the sequence of our samples is $[90/0]_s$: the 90° plies are the external plies, thus oxidation affects only a portion on the ply thickness, but over the whole ply surface.

4.4 Non-destructive free vibration tests

4.4.1 Identification of the transverse modulus by vibration tests

As it was seen in Section 4.3.4.1, the global behavior in tensile tests on $[90/0]_s$ specimens does not allow one to identify the effect of the oxidation aging on the transverse elastic modulus of the oxidized material. A test which allows to increase the participation of the oxidized ply on the overall response is required. Non destructive vibration tests are thus developed and carried out before each tensile test with the same sam-

ples which would be used in tensile tests. The variation of the stiffness of the oxidized composite plies is related to the variation of the natural frequency of the samples.

The setup of the test is shown in Fig. 4.13. The total length of a sample is 180 mm where zones of 40 mm on both sides of the sample are bonded with composite tabs. On one side, the zone bonded with composite tabs is fixed leaving the rest of the sample (140 mm) free as the useful length (L). On the other side, an additional mass of 9.15 g is stuck at the end of the sample, which leads the mass at the end of the sample to be much more important than any other parts along the length of the sample. An initial displacement, which is small enough so that no cracks would be created during the vibration test, is imposed to the free end where attached an accelerometer. Once the end is released, acquisition of the free vibration behavior via a LMS Test.Lab system is carried out.

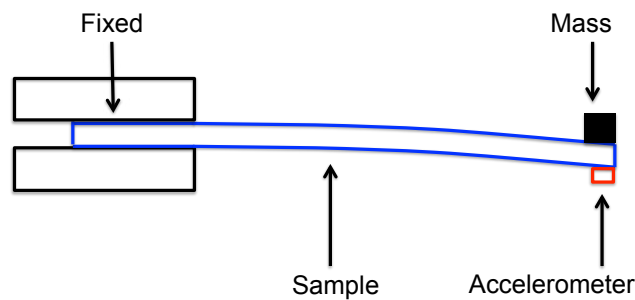


Figure 4.13: Setup of the non-destructive free vibration tests

Each sample is tested three times repeating the procedure from assembling the setup to launching a vibration (Fig. 4.14(a)). The frequency spectrum associated to the vibration history (Fig. 4.14(b)) as well as the natural frequency (f_n) can be obtained by analyzing the vibration history with FFT (Fast Fourier transform) method. The variability of the natural frequencies for the three tests on the same sample is very small (about 0.2%). The natural frequency of a sample is considered to be the average of the three tests.

The natural frequency of the samples aged for the same time are very repeatable. As shown in Tab. 4.2, the relative frequency variations are about 9 times higher than the variability of the tests, thus some information on the variation of the elastic properties with oxidation can be obtained.

Table 4.2: The natural frequencies of the samples aged for different times

Aging time	0 h	168 h (1W)	504 h (3W)	1008 h (6W)
f_n (Hz)	3.70 ±0.2%	3.71 ±0.3%	3.57 ±0.4%	3.50 ±0.6%
Relative variation of f_n		+0.3%	-3.5%	-5.4%

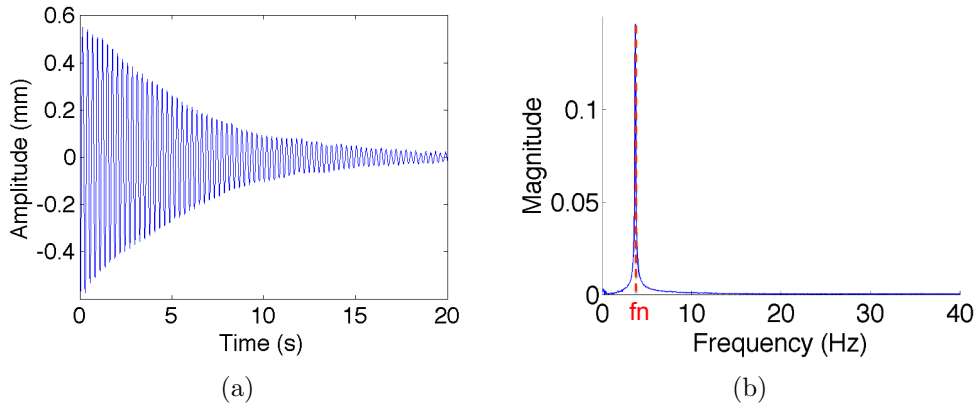


Figure 4.14: One example of the test results (a) Vibration history (b) Frequency spectrum

4.4.2 Modeling of the free vibration tests

Since an important additional mass (M) is positioned at the end of samples, the mass of the composite is neglected in the modeling. The stiffness of the laminated composites is related to the measured natural frequency as follows

$$K = (2\pi f_n)^2 M \quad (4.8)$$

Due to the test configuration, the bent samples can be also considered as an end loaded cantilever beams. The deflection of the beam is expressed

$$d = \frac{P}{K} = \frac{PL^3}{3EI_{eq}} \quad (4.9)$$

where EI_{eq} is the overall bending stiffness of the composite section. Substituting Eq. (4.8) into Eq. (4.9), EI_{eq} is expressed with the following equation

$$EI_{eq} = \frac{L^3(2\pi f_n)^2 M}{3} \quad (4.10)$$

The difference between EI_{eq} of the unaged samples and the aged samples is thus expressed as

$$\Delta EI_{eq} = EI_{eq} - EI_{eq,oxi} = \frac{4\pi^2 L^3 (f_n^2 - f_{n,oxi}^2) M}{3} \quad (4.11)$$

where $f_{n,oxi}$ is the natural frequency of the oxidized laminated composites. The difference between the aged and the unaged natural frequencies thus provides information

on the difference of the overall bending stiffness.

As the samples stacking sequence is $[90/0]_s$, EI_{eq} can be also expressed as Eq. (4.12) for unaged samples and Eq. (4.13) for aged samples

$$EI_{eq} = 2w \left[\int_0^h z^2 E_{x,0} dz + \int_h^{2h} z^2 E_{x,90} dz \right] \quad (4.12)$$

$$EI_{eq} = 2w \left[\int_0^h z^2 E_{x,0} dz + \int_h^{2h} z^2 E_{x,90oxi}(z) dz \right] \quad (4.13)$$

where z denotes the thickness direction of the laminate, w is the width of the specimen, h is the ply thickness, $E_{x,0}$ is the effective modulus of the 0° ply in the x direction (that is, E_1), $E_{x,90}$ and $E_{x,90oxi}$ are the effective moduli of the unaged and the aged 90° ply in the x direction (that is, E_2 and $E_{2,oxi}$). Since oxidation is non homogeneous throughout the sample thickness, $E_{2,oxi}$ depends on the distance from the exposed surfaces. $E_{2,oxi}$ is considered to be affected by two factors, the increase of the matrix elastic modulus and the oxidation aging induced damage mechanisms that reduce the modulus. The difference between Eq. (4.12) and Eq. (4.13) is expressed as

$$\Delta EI_{eq} = 2w \int_h^{2h} z^2 (E_2 - E_{2,oxi}(z)) dz \quad (4.14)$$

Combining Eq. (4.14) and Eq. (4.11),

$$2w \int_h^{2h} z^2 (E_2 - E_{2,oxi}(z)) dz = \frac{4\pi^2 L^3 (f_n^2 - f_{n,oxi}^2) M}{3} \quad (4.15)$$

In the above equation, the natural frequencies of the unaged and the aged samples are known parameters identified from the vibration tests. Considering the transverse modulus of the unaged samples as a known parameter, the only unknown parameter is $E_{2,oxi}(z)$. Some hypothesis on the variation of the oxidized elastic modulus through the ply thickness is required in order to identify a local value. In any case, the relative variations of f_n in Tab. 4.2 indicate qualitatively the variations of the effective transverse modulus of the oxidized ply.

The natural frequency of the samples aged for 1 week is similar to the unaged samples due to the short aging time. Then f_n decreases with the aging time. The negative relative variation of the natural frequency implies a decrease of the effective transverse modulus of the oxidized ply or the oxidized layer (about 10% of change in the overall stiffness for an aging of 6 weeks). Since the elastic properties have been proved to increase with the oxidation aging in Chapter 3 without taking into account the damage, the reductions of the effective transverse modulus of samples aged for 3

and 6 weeks can be only attributed to the oxidation induced damage. For the samples aged for 6 weeks, microscopic observations in the Chapter 2 have illustrated the cracks crossing the oxidized layer which are considered to be one of the sources of damage. For the samples aged for 3 weeks, since no cracks have been observed, the decrease of the effective transverse modulus seems to suggest the existence of the fiber/matrix interface debonding in the oxidized layer. Furthermore, the decrease of the effective transverse modulus implies that the reduction of the modulus due to damage is more important than the increase of the modulus due to the oxidation aging.

4.5 Conclusion

This chapter has presented two series of mesoscale tests and their results. The crack density evolution of the aged and the unaged $[90/0]_s$ samples, which are automatically evaluated via DIC, have been characterized from tensile tests. It is found that the critical longitudinal strain decreases and the crack density increases with the increase of the aging time. The crack density evolution of the unaged samples is going to be used to identify the critical strain energy release rate of the unaged material in the following chapter. The crack density evolution of aged samples results from the competition of two cracking mechanisms (partial cracks and cracks traversing the whole ply). A model to describe this competition is going to be discussed in the following chapter.

Tensile tests on $[90/0]_s$ samples are not sensitive enough to identify the transverse moduli of the oxidized layers because the oxidized 90° layer plays an unimportant role in the longitudinal behavior of the $[90/0]_s$ samples. The non-destructive vibration tests provide the natural frequency of the unaged and the oxidized composite laminates. The variations of the natural frequency implies the variation of the effective modulus of an oxidized ply. The decreased transverse moduli of the samples aged for 3 and 6 weeks indicate that the effect of the damage generated by the oxidation aging is more important than the increase of the elastic moduli.

Chapter 5

Towards a mesoscale modeling of transverse cracking in oxidized specimens

Contents

5.1	Introduction	90
5.2	Identification of G_c from the experimental results of the unaged samples	91
5.2.1	The micro-meso bridge for unaged plies	93
5.2.2	G_c of unaged samples	94
5.3	Modeling of the oxidized layer	96
5.3.1	Definition of a homogeneous equivalent oxidized layer	96
5.3.2	Oxidation profiles in the 90° ply	98
5.4	Micro-scale modeling of tranverse cracking of the oxidized samples	100
5.4.1	Transverse cracking during oxidation aging	100
5.4.2	Transverse cracking kinetics of the aged samples under tensile loading	102
5.5	Meso-scale modeling of tranverse cracking of the oxidized samples	107
5.6	Conclusion	108

5.1 Introduction

The modeling of the behavior of the oxidized laminated composites should take into account the effect of oxidation on the damage mechanisms. In Chapter 4, the kinetic of transverse cracking was observed experimentally for the aged and the unaged samples. This chapter focuses on the modeling of the observed phenomena at the microscale and the mesoscale.

Transverse cracking is one of the major damage mechanisms for laminated composites. In unaged samples, transverse cracks develop under tensile loading. Cracks generally initiate at the free edges and tend to cross the entire thickness of a ply. Transverse cracking reduces the stiffness of the laminate and, more importantly, it induces other damage mechanisms such as interlaminar delamination, which may lead to the final fracture of the laminate. Given the consequence of the transverse cracking, it is an essential phenomenon for the understanding and the modeling of the behavior of laminated composites.

In our aged samples, oxygen impacts the entire external surface of the laminate through a thickness less than a ply. Within the oxidized layer, the oxidation aging generates shrinkage and an increase of the elastic modulus of the matrix. On the $[90/0]_s$ samples, oxidation enhances the residual stresses generated by the manufacture temperature and stores additional energy. Consequently, the cracking phenomenon in the oxidized $[90/0]_s$ samples occurs earlier under tensile load as observed in the experiments of the previous chapter. In some aging conditions, cracks may appear in the absence of external applied loads, such as the cracks observed on the sample aged for 1008 h in Chapter 2. Moreover, cracks generated by the oxidation aging cross only partially the thickness of the 90° ply, which is quite different from the transverse cracking on unaged samples.

Many works have been carried out to explain, model and predict the transverse cracking on composite materials. Some researchers consider that a crack forms when the transverse stresses in plies reaches the strengths of those plies [104–106]. More recent works have described the cracking phenomenon in terms of an energy criterion [19, 108]. The strain energy release rate (G) is the released energy per unit of the fracture surface area, which is defined as

$$G = -\frac{\partial E_p}{\partial A} = -\frac{\partial(E_d - W_{ext})}{\partial A} \quad (5.1)$$

where E_p is the potential energy, E_d is the strain energy, W_{ext} is the work of external forces. Cracks propagate when G reaches the critical value G_c which is a material property. If propagation occurs at constant imposed displacements, the external work (W_{ext}) is constant and G can be simplified as

$$G = -\frac{\partial E_d}{\partial A} \quad (5.2)$$

The behavior of composite plies with the transverse cracking is studied at two scales in the mesoscale modeling strategy of LMT-Cachan. At the micro-scale, a composite ply is considered to be a continuous material but cracks are introduced as discrete entities. G of the transverse cracking is studied with a finite fracture mechanics approach which has been successfully used in previous studies on the transverse cracking [8, 107, 108]. G with a discrete representation is defined as

$$G = -\frac{\Delta E_d}{\Delta A} \quad (5.3)$$

where ΔA is the discrete variation of the crack surface area, ΔE_d is the variation of the strain energy between samples of two crack density states. At the mesoscale, the structure of a composite ply is continuous. The meso-scale damage due to the transverse cracking is homogenized from the micro-scale studies. The objective of this chapter is to extend the meso-scale modeling strategy to the studies on the oxidized plies.

5.2 Identification of G_c from the experimental results of the unaged samples

The critical strain energy release rate (G_c) is required for a study based on an energy criterion. The cracking behavior of an oxidized ply results from different effects of the oxidation aging, among others the weakening effect, which can decrease the G_c , and the shrinkage, which provides a supplementary driving force for the propagation. Since all of these effects are mixed during aging, it is impossible to identify G_c of the oxidized composite materials starting from self-cracking tests. In the following, G_c is assumed to be constant which enables us to study the role of the increase of elastic modulus and the shrinkage first. The value of G_c is identified from the experimental data of the unaged samples.

The behavior of the unaged laminated composites as predicted by the mesomodel of LMT-Cachan has been validated in various problems [32]. The identification of G_c consists of fitting the kinetics of cracking obtained from the tensile tests with the prediction of the mesomodel. These, in turn, are based on a micro-meso bridge in which the strain energy release rates and damage variables are calculated for different values of crack density and applied strain. The tensile test on the unaged samples is simulated using the material properties identified in Chapter 3.

The strain energy density of a composite ply with damages due to the transverse cracks is stated as [11]

$$e_d = \begin{bmatrix} \sigma_{11} \\ \sigma_{22} \\ \sigma_{33} \end{bmatrix}^t \begin{bmatrix} \frac{1}{E_1^0} & -\frac{\nu_{12}^0}{E_1^0} & -\frac{\nu_{12}^0}{E_1^0} \\ -\frac{\nu_{12}^0}{E_1^0} & \frac{1}{(1-\bar{d}_{22}[\sigma_{22}]^+)E_2^0} & -\frac{\nu_{23}^0}{(1-\bar{d}_{22}[\sigma_{22}]^+)E_2^0} \\ -\frac{\nu_{12}^0}{E_1^0} & -\frac{\nu_{23}^0}{(1-\bar{d}_{22}[\sigma_{22}]^+)E_2^0} & \frac{1}{E_2^0} \end{bmatrix} \begin{bmatrix} \sigma_{11} \\ \sigma_{22} \\ \sigma_{33} \end{bmatrix} \quad (5.4)$$

$$+ \frac{\sigma_{12}^2}{G_{12}^0(1-\bar{d}_{12})} + \frac{\sigma_{13}^2}{G_{12}^0} + \frac{\sigma_{23}^2}{G_{23}^0(1-\bar{d}_{23})}$$

where subscript 1 denotes the axial direction of elementary ply, 2 denotes the in-plane transverse direction and 3 denotes the out-plane direction. \bar{d}_{12} , \bar{d}_{22} , \bar{d}_{23} are damage variables of transverse cracking as functions of the crack density ρ . As samples are free of constraints in the out-plane direction during tensile tests, $\sigma_{33} = 0$, $\sigma_{13} = 0$ and $\sigma_{23} = 0$. Furthermore, in longitudinal tensile tests along the x direction, the 90° plies are mainly loaded in the transverse direction (22 direction), which propagates the Mode I cracking. As a result, the transverse cracking in our study is considered as a plane strain phenomenon, which provides two more conditions for the 90° ply, $\sigma_{12} = 0$ and $\epsilon_{11} = 0$ and a relation between σ_{22} and ϵ_{22}

$$\epsilon_{22} = -\frac{\nu_{12}^2}{E_1^0}\sigma_{22} + \frac{1}{(1-\bar{d}_{22})E_2^0}\sigma_{22} \quad (5.5)$$

Since $\frac{\nu_{12}^2}{E_1^0}$ is negligible compared with $\frac{1}{(1-\bar{d}_{22})E_2^0}$, the strain energy density can be simplified as

$$e_d = \frac{E_2^0(1-\bar{d}_{22})\epsilon_{22}^2}{2} \quad (5.6)$$

where the elastic strain ϵ_{22} is stated as

$$\epsilon_{22} = \epsilon_{22,a} - \alpha\Delta T \quad (5.7)$$

where $\epsilon_{22,a}$ is the total transverse strain of the 90° ply, which is also the total longitudinal strain (ϵ_a) for the laminate, α is the thermal expansion coefficient, ΔT is the temperature variation between the manufacture temperature and the environmental temperature of tests. According to the information provided by the project partners, $\alpha = 2.7 \times 10^{-5} \text{ } ^\circ\text{C}^{-1}$ and $\Delta T = 270 \text{ } ^\circ\text{C}$. Considering an elementary ply of length L and thickness h , the strain energy release rate can be obtained by substituting Eq. (5.6) into Eq. (5.2).

$$\begin{aligned}
 G &= -Lh \frac{\partial e_d}{\partial A} \\
 &= Lh \left[\frac{\epsilon_{22}^2 E_2^0}{2} \right] \frac{\partial \bar{d}_{22}}{\partial \rho} \frac{\partial \rho}{\partial A} \\
 &= h \left[\frac{\epsilon_{22}^2 E_2^0}{2} \right] \frac{\partial \bar{d}_{22}}{\partial \rho} \\
 &= h \left[\frac{\epsilon_{22}^2 E_2^0}{2} \right] f(\rho)
 \end{aligned} \tag{5.8}$$

where $\frac{\partial \bar{d}_{22}}{\partial \rho} = f(\rho)$ is the micro-meso bridge obtained from micro-scale simulations.

5.2.1 The micro-meso bridge for unaged plies

Micro-scale simulations and a finite fracture mechanics approach enable us to calculate the strain energy release rate for different values of ρ , and thus to identify the function $f(\rho)$ in Eq. (5.8).

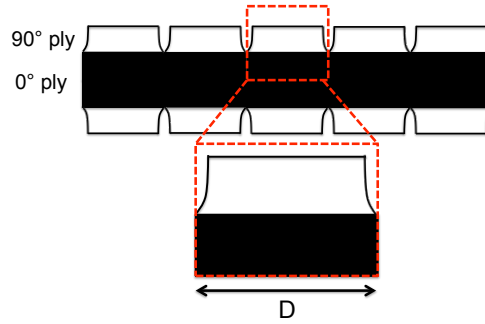


Figure 5.1: Locally periodic cracking and studied unit cell of sample

Cracks are considered to be locally periodic. The behavior of a composite sample can be obtained by studying one cell of the laminated composite between two cracks. Moreover it is sufficient to study only half of a cell thanks to the symmetric sequence of $[90/0]_s$ samples. The external 90° ply is equivalent to a double ply in terms of its transverse cracking behavior [10], thus the crack density is defined as $\rho = 2h/D$. The residual thermal strain is taken into consideration and the elastic properties of an unaged composite ply are those identified in the Chapter 3 via a homogenization method (Tab. 3.4). According to Eq. (5.3), G can be calculated as

$$G(\epsilon_{22}, \rho) = - \frac{E(\epsilon_{22}, 2\rho) - E(\epsilon_{22}, \rho)}{h} \tag{5.9}$$

where h is the growth of the crack surface area which is also the thickness of the 90° ply, $E(\epsilon_{22}, 2\rho)$ and $E(\epsilon_{22}, \rho)$ are the strain energy of two crack density states illustrated in Fig. 5.2

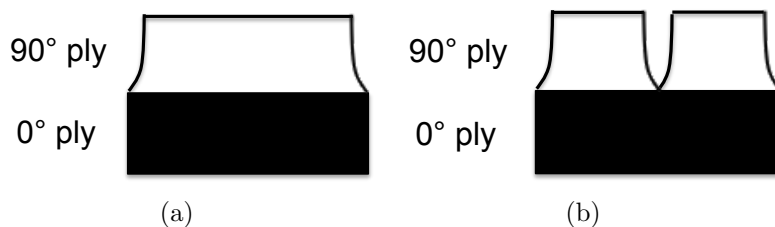


Figure 5.2: Periodic cells of samples with the crack density as (a) ρ (b) 2ρ

Assuming a constant elastic strain (ϵ_{22}), micro-scale studies allow to calculate point by point G for different ρ (Fig. 5.3(a)). Substituting the determined G into the mesoscale model (Eq. (5.8)), a discrete $f(\rho)$ can be identified. And $f(\rho)$ at any crack densities can be predicted by a method of interpolation (Fig. 5.3(b)).

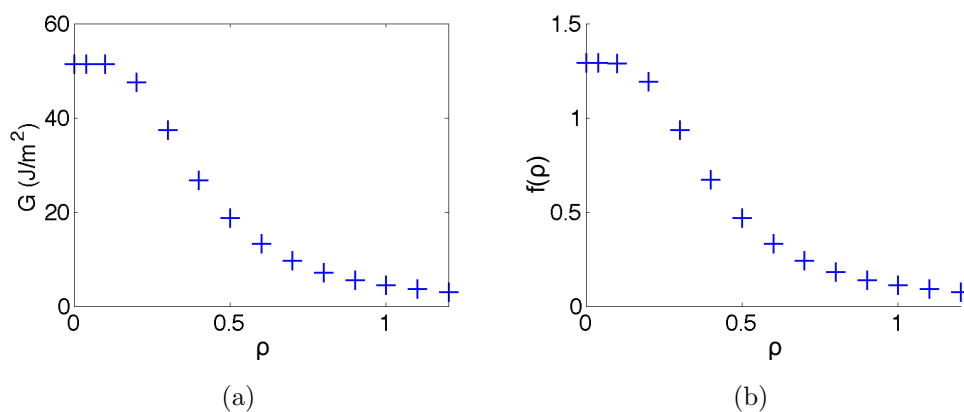


Figure 5.3: (a) G at $\epsilon_{22} = 0.0052$ and (b) $f(\rho)$ versus ρ

5.2.2 G_c of unaged samples

As G is a function of ρ and ϵ_a (Fig. 5.4(a)), the evolution of ρ can be related to ϵ_a by projecting their correlation at a given G as show in Fig. 5.4(b).

Furthermore, researchers have noticed that the kinetics of the transverse cracking obtained from a study based on the finite fracture mechanic should be scaled 1.2 to 1.45 times when comparing with the experimental data [8,96]. This allows to reconcile the discrete nature of transverse cracking, in which the local crack density jumps discretely between ρ and 2ρ when a new crack appears (see Fig. 5.2), with a continuous representation of ρ as the average crack density.

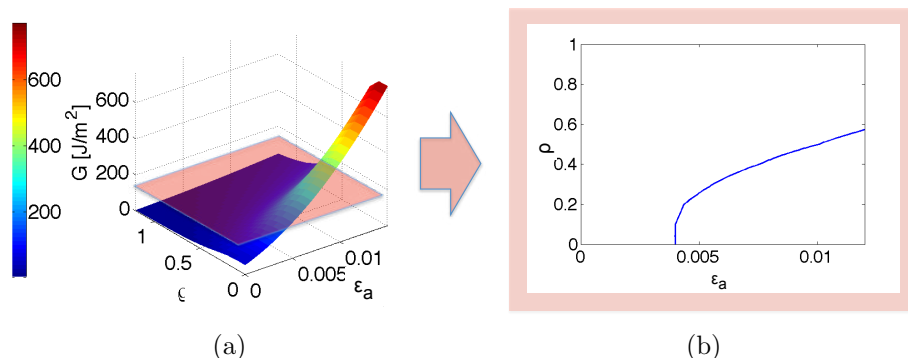


Figure 5.4: (a) G as a function of ρ and ϵ_{22} (b) Example of ρ versus $\epsilon_{22,a}$ at $G_c = 170 \text{ J/m}^2$

The critical energy release rate (G_c) is identified by fitting the scaled analyzed kinetic of cracking with the experimental results. In spite of a slight difference at the beginning of cracking, the predicted crack density evolution with $G = 170 \text{ J/m}^2$ and a scale factor of 1.55 fits the best with the experimental data of the tensile tests on the unaged samples (Fig. 5.5). At the beginning of the cracking, the predicted crack density increases sharply whereas the cracks detected experimentally initiate at a lower total longitudinal strain and increase smoothly. This difference has been noted by other researchers and explained with the preexisting damages or defects which facilitate locally the cracking phenomenon [55]. Consequently, G_c for the unaged composite ply is identified as 170 J/m^2 .

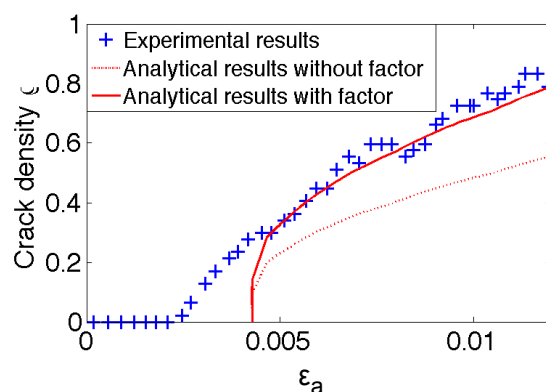


Figure 5.5: Experimental crack density evolution fitted by analytical results with $G_c = 170 \text{ J/m}^2$

Cracks in the oxidized samples are usually observed to initiate at lower loading levels or fatigue levels [22, 55]. This is related to a combination of different effects. Since the experimental information resulting from self-cracking tests is not enough to identify G_c

of the oxidized composite materials, its value is kept constant and equals to the one of the unaged samples in the following sections. This enables us to investigate first the effects of the increase of elastic modulus and the shrinkage on the transverse cracking behavior of the oxidized specimens.

5.3 Modeling of the oxidized layer

5.3.1 Definition of a homogeneous equivalent oxidized layer

In aged specimens, the oxidation level and the associated material properties vary locally across the oxidized zone, whose thickness may be lower than a ply's thickness. In classical mesoscale models, on the other hand, the elastic and damage behavior is considered homogeneous across the thickness of each ply. In order to preserve the existence of homogeneous layers, which is rather useful for mesoscale modeling, we chose to introduce an equivalent homogeneous oxidized layer for the following micro-scale study. The oxidized 90° ply thus consists of two parts, the homogeneous oxidized layer and the unoxidized layer (Fig. 5.6). The relative concentration of oxidation products q in the homogeneous oxidized layer and its thickness need to be defined.

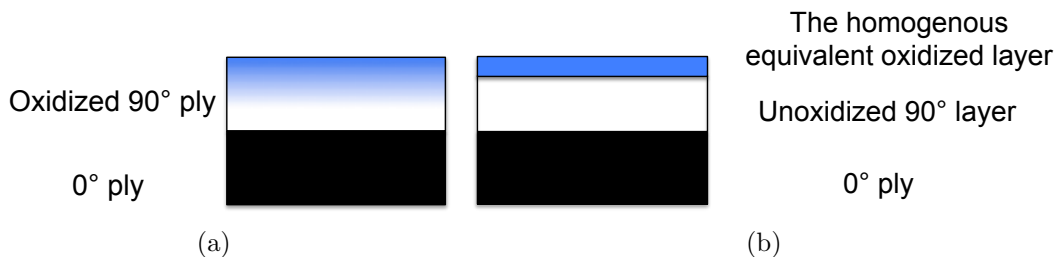
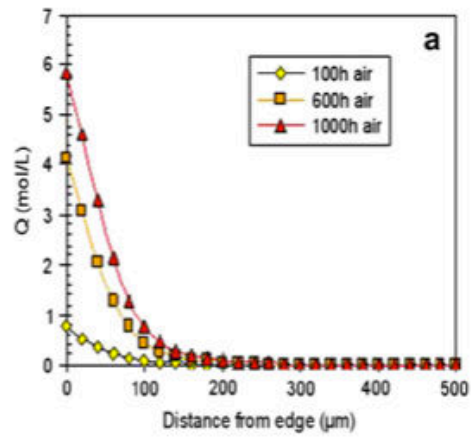
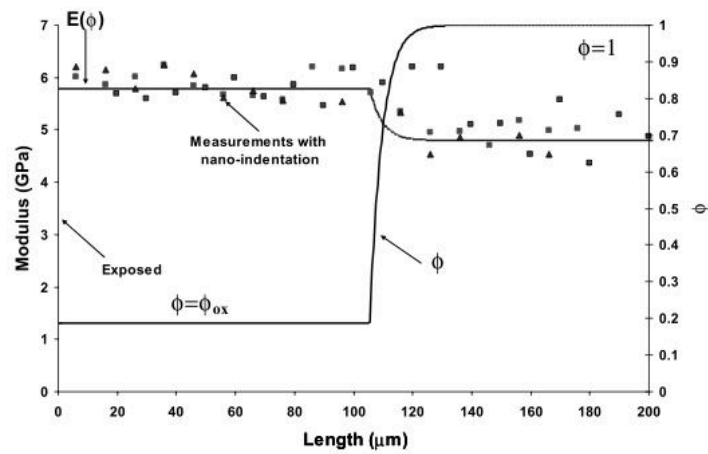


Figure 5.6: (a) Real oxidized ply and unoxidized layer (b) Homogeneous equivalent oxidized layer

Depending on the material composition and the aging condition, the oxidized layer may evolve in two ways. For materials possessing a low reactivity but high quantities of oxidizable sites, a saturation state of the oxidation will not be achieved in the aging time of our study (1008 h). The oxidation level increases continually with the aging time, but the thickness of the oxidized layer remains constant (Fig. 5.7(a)). This is well described by diffusion/reaction models in which the hypothesis of low conversion rates is introduced [23]. On the contrary, for materials possessing a high reactivity but low quantities of oxidizable sites, the oxidation aging reaches quickly a saturation state and the thickness of the oxidized zone continually increases. An indicator of this kind of process is the presence of a zone in which the matrix modulus is constant, but higher than the one of the unaged material (Fig. 5.7(b)). This situation is well described in the model of three zones [50, 51].



(a)



(b)

Figure 5.7: (a) Calculated concentration of oxidation products of an epoxy resin aged at 150 °C in the air [14] (b) G30-500/PMR-15 aged at 288 °C in the air [39]

There are thus two possible ways to model the thickness of the homogenous oxidized layer h_{eq} . It can be defined as Eq. (5.10).

$$h_{eq} = \frac{\int_0^h q(z, t) dz}{q(0, t)} \quad (5.10)$$

where h is the thickness of the oxidized ply. If the transient diffusion/reaction phase is short comparing to the aging time, $q(z, t)$ is proportional to the aging time, the ratio between $\int_0^h q(z, t) dz$ and $q(0, t)$ is time independent, leading to a constant value of the homogeneous oxidized layer. What varies with the duration of aging is the q in the homogeneous oxidized layer. This choice represents well the situation for the material possessing a low reactivity and high quantities of oxidizable sites.

A different definition of the homogeneous oxidized layer is the following

$$h_{eq} = \frac{\int_0^h q(z, t) dz}{q_{max}} \quad (5.11)$$

In this case, the relative concentration of the oxidation products in the equivalent homogeneous oxidized layer is a constant (which is the saturation level, $q_{max} = 1$) whereas the thickness of the homogeneous equivalent oxidation layer increases with the oxidation aging. This represents well the situation for the material possessing a high reactivity and low quantities of oxidizable sites.

In this study, the characterization and modeling of the diffusion/reaction behavior of the material was carried out by the project partners in parallel with the present work. For this reason, we chose arbitrarily to consider the first description of the oxidized layer, which is coherent with the behavior of a well known epoxy at about the similar aging condition [23]. In the next section, the oxidation profiles for different aging times are calculated based on the diffusion/reaction model and the material parameters in [23], which enables us to define the thickness of the homogeneous oxidized layer used in the modeling.

5.3.2 Oxidation profiles in the 90° ply

In order to determine the thickness of the homogeneous oxidized layer to be used in the modeling, one needs to determine the profiles of the relative concentration of the oxidation products (q) within the 90° ply.

Here, the oxidation profiles for different aging times are determined via the diffusion/reaction model of Colin [91], including the assumption of low conversion ratios to simplify the numerical resolution of the differential equations. The diffusion/reaction process in the transverse direction is described by the following equations [23]

$$\frac{\partial C}{\partial t} = D_2 \frac{\partial^2 C}{\partial x^2} - R(C) \quad (5.12)$$

$$R(C) = 2R_0 \Psi \frac{\beta^* C}{1 + \beta^* C} \left[1 - \frac{\Phi \beta^* C}{2(1 + \beta^* C)} \right] \quad (5.13)$$

$$\text{with } \Psi = \left(1 - \frac{\varphi}{2}\right) \left(1 + \frac{\varphi}{4}\right), \quad \Phi = \frac{1 - \varphi/2}{1 + \varphi/4} \quad \text{and} \quad \beta^* = \frac{\beta}{1 + \varphi/4} \quad (5.14)$$

where D_2 is the transverse diffusivity defined as

$$D_2 = \frac{1 - 2\sqrt{V_f/\pi}}{1 - V_f} D_1 \quad (5.15)$$

D_1 is the longitudinal diffusivity which equals the diffusivity of the neat resin D . The material parameters used are those of the well known epoxy aged at 180 °C in air, as shown in Tab. 5.1

Table 5.1: Parameters used in the diffusion/reaction calculation [23]

$D_1 = D$ ($m^2 \cdot s^{-1}$)	R_0 (s^{-1})	β ($l \cdot mol^{-1}$)	φ	C_0 ($mol \cdot m^{-3}$)	V_f
1.8×10^{-12}	9.4×10^{-6}	352	1.0×10^{-2}	3.5×10^{-3}	0.54

The profiles of the relative concentration of the oxidation products (q) for different aging times are calculated and shown in Fig. 5.8. Since the reaction rate depends only on the local concentration of the oxygen (C) and the transient phase of the oxygen diffusion is very short compared with the entire aging time (less than 1 hour vs. 1008 h), the local relative concentration of oxidation products ($q(x, t)$) is almost proportional to the aging time.

Based on these results, the homogeneous oxidized layer thickness is defined as $h_{eq} = 16.5 \mu m$. The relative concentration of the oxidation products q and the associated material properties of the ply are obtained by interpolating the homogenized values calculated in Chapter 3 as given in Table (5.10).

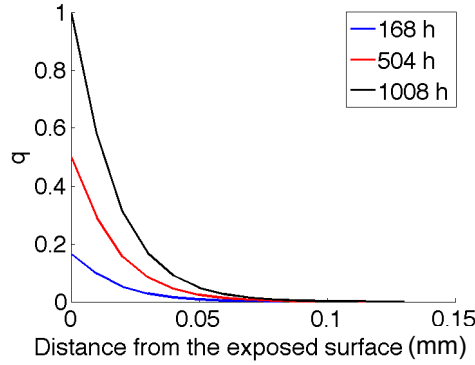


Figure 5.8: Predicted profile of q for samples aged for different times in air at 180 °C

Table 5.2: The oxidation levels and the properties of the oxidized composite materials aged for different times

Aging time (h)	q	E_1 (GPa)	E_2 (GPa)	G_{12} (GPa)	ν_{12}	ν_{23}	$\epsilon_{22,o}$
168	0.1667	127	10.98	3.63	0.45	0.22	0.38%
504	0.5	127	12.1	4.06	0.45	0.22	1.14%
1008	1	127	13.63	4.64	0.45	0.22	2.23%

5.4 Micro-scale modeling of transverse cracking of the oxidized samples

5.4.1 Transverse cracking during oxidation aging

It has been shown in Chapter 2 that cracks crossing partially a ply exist on the samples aged for 6 weeks. However, the same phenomenon has not been observed on the other aged samples. To understand the phenomenon, the strain energy release rates (G) of cracks crossing different thicknesses are studied at the micro-scale in ABAQUS with a finite fracture mechanic method.

G is calculated from the strain energy variation between periodic models of a healthy sample and of a sample with a crack crossing different thicknesses of 90° ply (Fig. 5.9). All the models contain 3 parts, the homogeneous oxidized 90° layer, the unoxidized 90° layer and the 0° ply. The material properties corresponding to a given level of oxidation q are attributed to the homogeneous oxidized layer. The thermal stress is taken into account. The out-of-plane direction of the sample is free of constraints but the longitudinal direction of the sample is constrained with the periodic conditions. No macroscopic displacement is applied, which allows to simulate a state after the aging

5.4. Micro-scale modeling of transverse cracking of the oxidized samples 99

and before the tensile test. Cracks of the lengths from the thickness of the homogenized oxidized layer to the thickness of an entire 90° ply are introduced. The interfaces of the three parts are perfectly bonded together. Mesh at the region of the crack tip and beside the interface are refined.

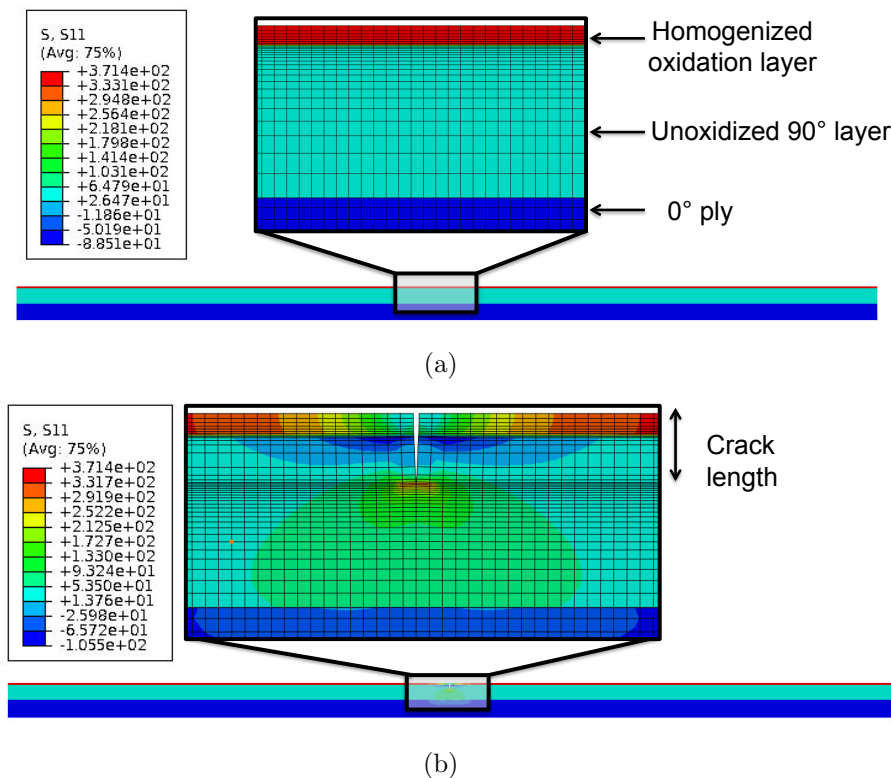


Figure 5.9: Longitudinal stress field of (a) models of healthy sample (b) models of cracked sample

G of cracks crossing different lengths on the samples aged for different times are shown in Fig. 5.10. G of the unaged sample and of the sample aged for 168 h and 504 h are lower than G_c ($170 J/m^2$) no matter the crack lengths whereas G of the sample aged for 1008 h has exceeded the criterion, which explains the observation that cracks exist only on the samples aged for 6 weeks. As no additional longitudinal displacement has been applied to samples, the strain energy is generated by the different thermal shrinkage between 0° ply and 90° and the additional oxidation shrinkage in the homogeneous oxidized layer. Consequently, a sample aged for a longer duration possesses a higher strain energy release rate.

Samples aged for different times show different tendencies with the increasing of the crack length. The energy release rate of the unaged sample increases almost proportionally with the increasing of crack length. Similarly to the unaged sample, G of the sample aged for 168 h increases with the crack length, though nonlinearly. The increase

of G with the crack length indicates that cracks are unstable. Therefore they will cross the entire ply in the unaged sample and the sample aged for 1 week. However, G of the sample aged for 1008 h decreases with the crack length after propagating through the homogeneous oxidized layer. In these samples, cracks crossing the oxidized layer are more stable and release more energy, which explains the preference of the cracks crossing partially the 90° ply samples aged for 6 weeks. The sample aged for 504 h seems in an intermediate state.

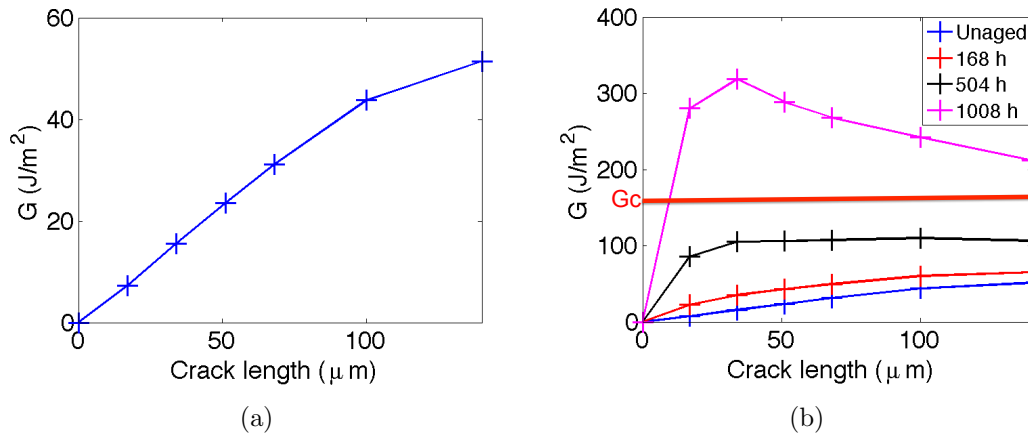


Figure 5.10: G versus different crack lengths (a) unaged sample (b) all the samples

The micro-scale study on G in this section verify our microscopic observations and explain the phenomenon of cracks crossing partially a ply. By evaluating the variation of G with the crack length, two modes of cracking seem to exist in the oxidized laminated composites. In one mode, cracks cross immediately the entire thickness of a ply once initiated, which is the classic mode of cracking in unaged samples. They are referred to as the complete cracks in the following sections. In the other mode, cracks cross partially the 90° ply. In certain aging conditions, partial cracks possess a higher strain energy release rate due to the presence of the oxidized layer and become the preferential mechanisms. According to the simulation results, the length of the partial cracks is slightly higher than the thickness of the homogenous oxidized layer. In the following study, however, partial cracks are assumed to cross only the thickness of the homogeneous oxidized layer to simplify the mesoscale modeling.

5.4.2 Transverse cracking kinetics of the aged samples under tensile loading

The study in the previous section explained the microscopic observations of the aged samples before tensile tests. In this section, the cracking kinetics of the aged $[90/0]_s$

5.4. Micro-scale modeling of tranverse cracking of the oxidized samples 101

samples under tensile load are going to be investigated via an incremental study.

In practice, energy is stored in samples during the tensile test until $G = G_c$. Then G will be limited at G_c by releasing the extra energy with new cracks. The energy release rate depends thus on two parameters, the applied longitudinal strain (ϵ_a) and the crack density (ρ).

The incremental study describes the behavior of the aged samples by considering small increments of ρ and ϵ_a . Given a pair of (ϵ_1, ρ_1) , if $G(\epsilon_1, \rho_1) < G_c$, samples are loaded in the tensile direction until $G(\epsilon_2, \rho_1) = G_c$, which means the samples have stored enough energy to propagate new cracks. The crack density thus increases from ρ_1 to ρ_2 . New cracks release the strain energy, which leads $G(\epsilon_2, \rho_2)$ to fall below G_c again. Therefore, a higher applied strain (ϵ_3) is required for G reaching G_c again, forming new cracks. The cracking kinetic is obtained by linking the points which satisfy the condition $G = G_c$ (Fig. 5.11). G_c in this study is assumed to be 170 J/m^2 and G is calculated at the micro scale with the finite fracture mechanic method.

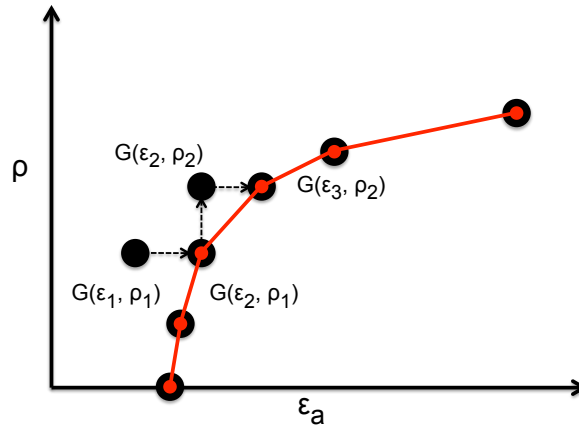


Figure 5.11: Illustration of the incremental study

A first study is carried out considering only the classic mode of cracking, that is the complete cracks. $G(\epsilon_a, \rho)$ is defined as Eq. (5.9) calculated from two periodic cells with different crack densities (Fig 5.2). The kinetics of cracking (Fig. 5.12) are obtained by plotting point by point the increments of (ϵ, ρ) which limit $G(\epsilon, \rho)$ at G_c . Furthermore, ρ is scaled with the factor 1.55 identified in the previous section when comparing the results obtained from a finite fracture mechanic method with the experimental data.

The kinetics of cracking for the samples aged for 1 and 3 weeks seems to be well represented with the micro-scale incremental studies by considering the complete cracks alone. Compared with the kinetic of cracking of the unaged sample, cracking occurs earlier in the samples aged for 1 week and even earlier for those aged for 3 weeks, as it has been observed in experiments. However, an overestimation of the numerical study can be noted at the beginning of the cracking phenomenon of the samples aged for 6

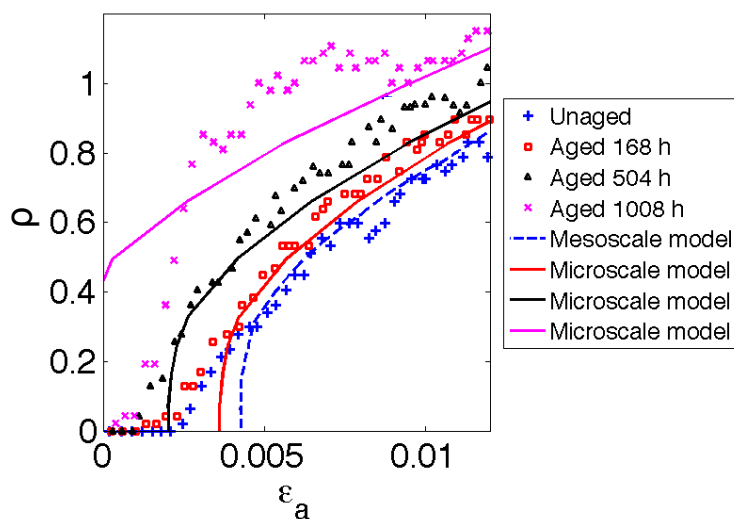


Figure 5.12: Kinetics of cracking without taking into account partial cracks of the samples aged for different times

weeks. According to the incremental study, the oxidation aging generates already a number of complete cracks before the tensile tests on samples aged for 1008 h, which can not be verified by our microscopic observations and the crack detection with DIC at the low applied strains. The inconsistency is attributed to the influence of the observed partial cracks which have not been taken into account.

The incremental study for the samples aged for 1008 h is thus modified by considering the presence of both partial and complete cracks. This leads to three possible cracking scenarios. Scenario A represents the creation of a new partial crack between existing cracks, which is located in the homogenous oxidized layer. Scenario B is the propagation of an existing partial crack to a complete crack, which is located in the unoxidized layer. And Scenario C is a new complete crack between existing cracks through the entire thickness of the ply. Since an oxidized composite ply consists of the homogeneous oxidized layer and the unoxidized layer, the crack densities within the two layers are normalized with respect to the corresponding thicknesses. The crack density in the homogeneous oxidized layer is noted ρ_p and the crack density in the unoxidized layer is noted ρ_t .

The strain energy release rate of the three scenarios are compared at each increment. The scenario whose strain energy release rate reaches firstly G_c with the increase of ϵ_a is considered preferential. The crack density in the associated layer is thus raised. G of the Scenario B is found always higher than G of the Scenario C.

Therefore, only two scenarios (A and B) take place during the tensile test. The strain energy release rate of partial cracks is referred to as G_p , on the other hand, the strain energy release rate of the crack propagation within the unoxidized layer is

5.4. Micro-scale modeling of transverse cracking of the oxidized samples 103

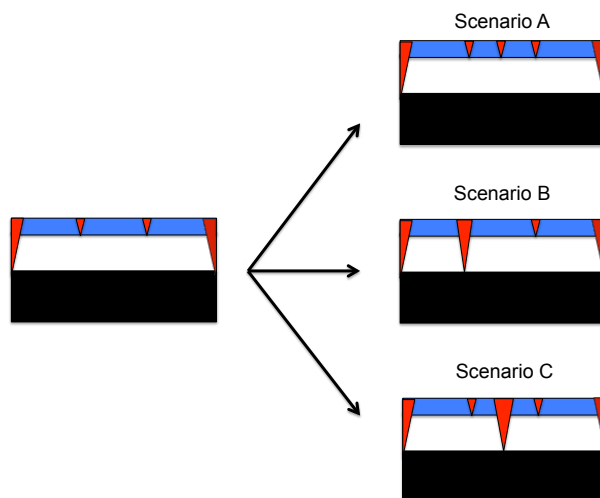


Figure 5.13: Three possible scenarios of cracking

Table 5.3: Example of the strain energy release rates for different scenarios ($\epsilon_a = 0$, $\rho_p = 0.38$, $\rho_t \approx 0$)

	Scenario A	Scenario B	Scenario C
G (J/m^2)	170	131	127

referred to as G_t . G_p and G_t are calculated with periodic cells whose length depending on the crack density in the unoxidized layer. The number of partial cracks depends on the length of the periodic cell. They are laid periodically along the length of the periodic cell as shown in Fig. 5.14.

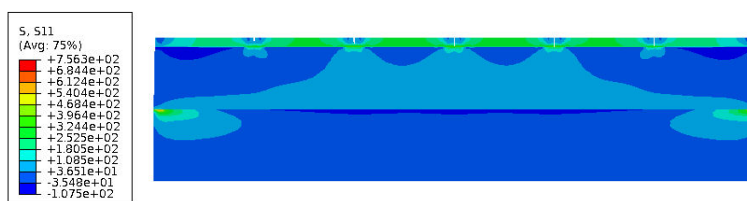


Figure 5.14: Exemple of the periodic model of $\rho_p = 0.2$ and $\rho_c = 0.3$

The result of the incremental study taking into account partial cracks is shown in Fig. 5.15. ρ_t is scaled with a factor of $\frac{h}{h-h_{eq}}$ in order to compare it with the crack density obtained with tensile tests or with the incremental study without taking into account the partial cracks which are calculated with h . Partial cracks are proved to be preferential during the aging process without additional tensile strain. The crack density of the partial cracks (ρ_p) increased until about 0.38 with no additional applied strain. With the tensile process, ρ_p continue to increase slightly to 0.40. Then the cracking process is dominated by the propagation of the existing partial cracks through the

unoxidized layer. The increase of partial cracks during this period is almost negligible. It is necessary to note that although ρ_p has been quickly overpassed by ρ_t , the number of partial cracks is still much higher than that of complete cracks because the thickness of the homogeneous oxidized layer is very small. Compared to the study considering only the complete cracks, the kinetic of the cracking crossing the entire layer has been delayed, because the partial cracks have released a part of the energy. The result of an incremental study with taking into account the partial cracks seems more coherent with the experimental data (Fig. 5.16).

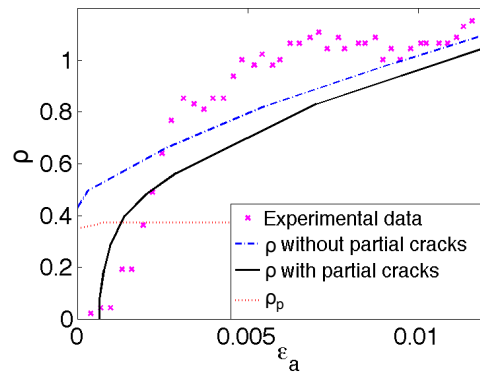


Figure 5.15: Comparison between kinetics of cracking with and without taking into account partial cracks for samples aged for 1008 h at 180 °C in the air

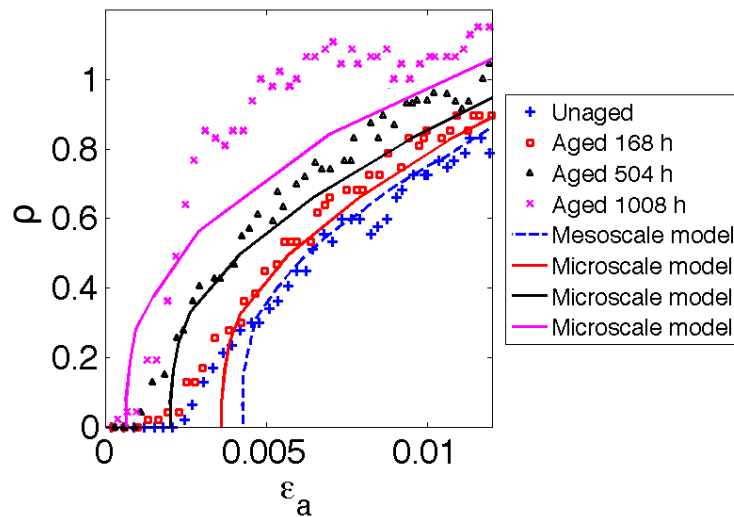


Figure 5.16: Kinetics of the complete cracks in the samples aged for different times

5.5 Meso-scale modeling of tranverse cracking of the oxidized samples

According to the meso-scale modeling strategy, the meso-scale behavior of a ply is homogenized from the micro-scale behavior. For the unaged samples with the classical complete cracking, the transverse cracks are translated into meso-scale damage variables and the bridge functions which are quasi-independent of the structure geometry, the loading conditions and the behavior of the adjacent plies [7].

In the case of the aged samples, an oxidized ply described as two homogeneous layers, the homogeneous oxidized layer and the unoxidized layer, which are strongly coupled (Fig. 5.13). The propagation of the existing partial cracks through the unoxidized layer does not only release the energy in the unoxidized layer but also the energy in the homogeneous oxidized layer. Fig. 5.17 shows the strain energy release rate of the partial cracks (G_p) on the sample aged for 6 weeks as a function of the total longitudinal strain compared with the crack density evolution of complete cracks ρ . G_p of the partial cracks decreases with the increase of the density of the complete cracks, although the total longitudinal strain has been increased.

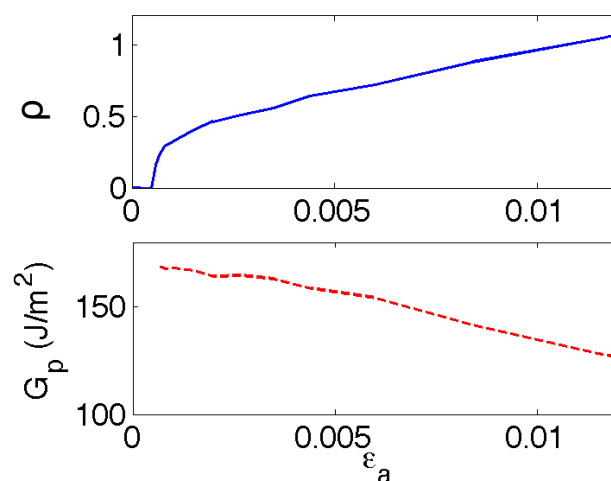


Figure 5.17: Evolution of G_p and the crack density of complete cracks versus the total strain at $\rho_p = 0.38$

One the other hand, the partial cracks in the homogeneous oxidized layer generate stress concentrations which influence the behavior of the unoxidized layer. Fig. 5.18 shows the energy release rate to propagate cracks in the unoxidized layer (G_t) during the aging process (ϵ_a). Though the crack density in the unoxidized layer remains 0, G_t decreases with the increase of the partial cracks which shows the partial cracks located in the homogeneous oxidized layer release the energy in the unoxidized layer also.

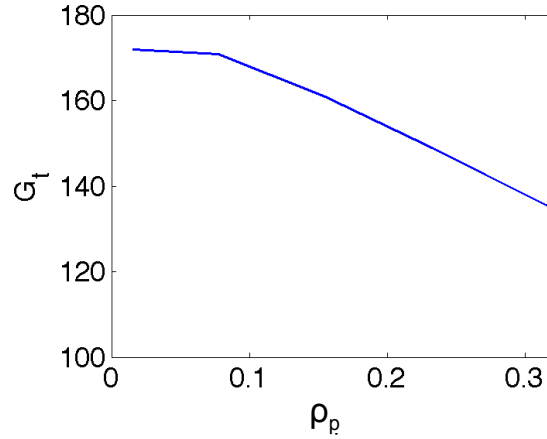


Figure 5.18: G_t influenced by ρ_p at $\epsilon_a = 0$

Due to the interactions of the two layers, the behavior of each of them is no longer independent, as the case for the unaged samples in the mesomodel of LMT-Cachan. A first idea to construct a mesomodel accounting for the oxidized layer is to construct a meso-scale model based directly on the kinetics of cracking obtained from micro-scale studies. To predict the behavior of an aged sample at any oxidation levels (q) and at any loading conditions ($\epsilon_a = 0$), it is required to realize firstly the micro-scale incremental studies taking into account the different scenarios. The results of the incremental study allow to determine point by point the ρ and ϵ_a which satisfy the condition $G(\epsilon_a, \rho) = G_c$. In this way, the crack densities of a layer are related directly to the meso-scale parameter ϵ_a . Starting from the crack density, damage variables can be defined as the case in the micro-meso bridge for unaged samples.

5.6 Conclusion

This chapter presented the modeling of the transverse cracking behavior of the oxidized ply taking into account two effects of the oxidation aging (increase of elastic modulus and shrinkage). This study provides a deeper understanding of the effect of the oxidation aging on the cracking behavior of an oxidized ply. A meso-scale modeling strategy based on the micro-scale description of the two competing cracking mechanisms has been proposed. The proposed strategy requires as input the diffusion/reaction behavior of the material, as well as the effect of oxidation on the matrix behavior.

The results of the micro-scale incremental study seem consistent with the kinetic of transverse cracking measured experimentally, although the possible weakening effect of the oxidation aging on G_c has not been taken into account. The reason may be attributed to the small thickness of the oxidized layer compared with the unoxidized layer. While the appearance of partial cracks during aging may be influenced by the

weakening of the oxidized layer, the evolution of complete cracks is driven by the critical strain energy release rate of the unaged material. In the following chapter, an experiment is developed and carried out focusing on the crack tip of the oxidized composite material to study the G_c weakened by the oxidation aging.

Chapter 6

The oxi-delamination test

Contents

6.1	Introduction	112
6.2	Material and experimental technology	112
6.2.1	The classical climbing drum peel test	113
6.2.2	Samples for the CDP tests	115
6.2.3	The oxi-delamination test: crack propagation driven by the oxidation	115
6.3	Results	117
6.3.1	G_c of unaged samples	117
6.3.2	Evolution of the displacement during the oxi-delamination tests	118
6.3.3	The propagation velocities under different external loads	119
6.4	Modeling of G_c at different oxidation levels	120
6.5	Conclusions	122

6.1 Introduction

The coupling between oxidation and crack propagation is detrimental to the response of composites in a high temperature environment. An example discussed in this work is the modification of the kinetic of transverse cracking for aged specimens, which was observed experimentally in Chapter 4 and modeled in Chapter 5. The proposed model takes into account the increase of the matrix elastic modulus and the shrinkage associated with oxidation, which modify the driving force for crack propagation. The material toughness G_c of the oxidized material, however, was assumed to be the same as that of the unaged material due to the lack of experimental information available for its identification.

In most experimental works available in the literature, the oxidation aging and the mechanical testing are carried out one after the other. As a result, cracks develop in the absence of external mechanical loads, thus the role of the different mechanisms related to oxidation cannot be dissociated. As for the mechanical response, it is often difficult to interpret since oxidation is not uniform across the specimen. For this reason, results such as [62] provide interesting information on the failure mechanisms of oxidized specimens, but they cannot be used directly to identify quantitatively the properties of the oxidized material. In this context, specific tests are required for the aged samples whose mechanism is more local.

A new test was conceived and carried out to study the propagation of Mode I delamination under external mechanical load and an oxidative environment. The oxi-delamination test is based on the standard climbing drum peel test (ASTM D1781-98 [20]). The samples are loaded with a constant external force, which is equivalent to provide a constant available strain energy release rate (G_{ext}). With the oxidation process, the weakening effect of the oxidation aging reduces G_c of the material to the imposed G_{ext} and propagates the delamination. The velocities of crack propagation for different available strain energy release rates can be related to the oxidation level via a diffusion/reaction model.

6.2 Material and experimental technology

The standard climbing drum peel (CDP) test [20] is typically used to identify the Model I critical strain energy release rate G_{Ic} associated to the skin/core debonding of sandwich specimens. In this test, the skin/core debonding is generated by rolling the skin of a sandwich specimen around a drum-like object at a constant speed. The critical strain energy release rate can be determined with the measured forces and displacements [109]. In this work, the test has been modified to study the oxidation-driven propagation of the delamination in composite specimens.

6.2.1 The classical climbing drum peel test

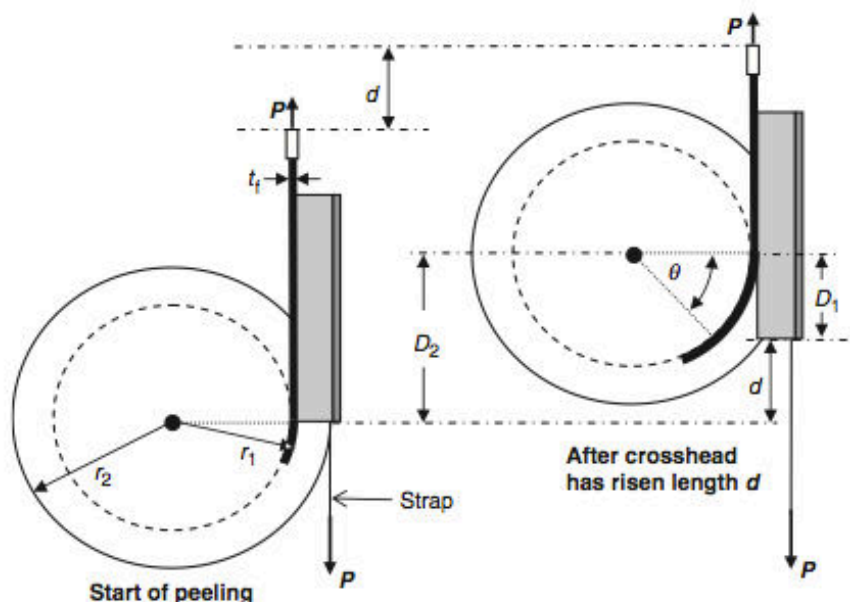


Figure 6.1: Setup of the standard climbing drum peel test [109]

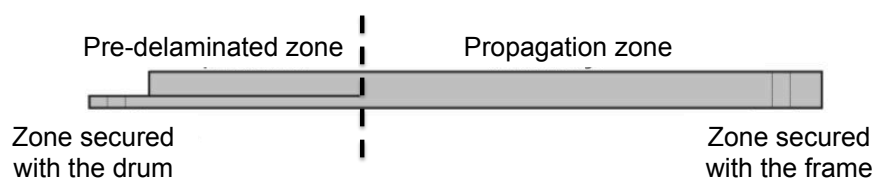


Figure 6.2: Sample for the climbing drum tests

A scheme of the standard CDP test set-up is shown in Fig. 6.1. The sample (Fig. 6.2) contains two parts: the pre-debonded zone (whose end is secured to the drum's internal radius) and the propagation zone (whose end is fixed to the loading frame).

The upper frame, which is also the loading frame, is driven by an upward displacement at a constant rate. The lower frame, which is a fixed frame, is attached to thin metal straps which are rolled around two flanges attached to the drum. As the radius of the flanges is larger than the internal radius of the drum, a torque is generated. With the imposed displacement, the straps unroll and the drum 'climbs' along the specimen, first rolling up the pre-debonded zone and then propagating the delamination along the interface.

Considering D_2 as the unrolled length of the strap and D_1 as the rolled up length of the delaminated layers, they can be expressed as

$$D_1 = \theta r_1 \quad (6.1)$$

$$D_2 = \theta r_2 \quad (6.2)$$

where r_1 and r_2 are the radii associated to the rolling up of the delaminated layers and of the straps and θ is the rolled angle of the drum. Their difference is the displacement imposed by the loading frame as shown in Fig. 6.1

$$d = D_2 - D_1 \quad (6.3)$$

Combining Eqs. (6.1), (6.2) and (6.3), one has the following relation between the measured displacement and the displacement of the drum along the specimen

$$D_1 = d \frac{r_1}{r_2 - r_1} \quad (6.4)$$

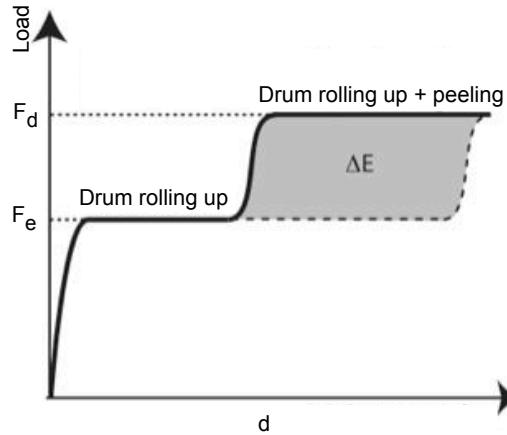


Figure 6.3: Typical curve of the applied displacement versus force of a climbing drum peel test

The imposed displacement and the resultant force are measured by the testing machine. A typical force/displacement plot is given in Fig. 6.3. Two constant load portions can be noted: the first value (F_e) corresponds to the force needed to make the drum climb along the specimen (which involves the increase of the drum's potential energy and the rolling up of the pre-delaminated part of the specimen), while the second value (F_d) includes the additional force required to propagate the delamination. The extra energy used to propagate the delamination (ΔE) is represented by the shaded area in Fig. 6.3. The critical strain energy release rate G_c is then calculated as follows, according to its definition:

$$G_c = \frac{\Delta E}{\Delta A} = \frac{(F_d - F_e)\Delta d}{\Delta D_1 w} = \frac{(F_d - F_e)(r_2 - r_1)}{r_1 w} \quad (6.5)$$

where w is the width of the samples.

6.2.2 Samples for the CDP tests

In our study, the skin/core debonding of sandwich specimens is replaced by the interlaminar delamination of monolithic composite specimens. The stacking sequence of the specimens is $[0_2/ + 45/ - 45/0]_s$, with a pre-delamination between the external double 0° ply and the 45° ply. The asymmetric position of the pre-delamination with respect to the midplane of the specimen ensures that the peeled layer, the double 0° ply, is relatively flexible while the rest of the sample is rigid enough to avoid the bending generated by the rolling drum.

Tests are carried out with a well known composite material whose information on the oxidation behavior is more rich [14, 49, 57]. For example, Colin and co-workers [57] have performed the self-cracking tests on a unidirectional laminate and identified the propagation velocity in the direction of fibers as $0.034 \mu\text{m}/\text{h}$ in air at 150°C . This allows to have an order of magnitude of the expected propagation velocities during the oxi-delamination test.

6.2.3 The oxi-delamination test: crack propagation driven by the oxidation

The standard CDP test has been modified in order to obtain a crack propagation which is driven by the oxidation aging. This test is called the oxi-delamination test.

First, the specimen is kept in a climatic chamber during testing, allowing to impose a high temperature which accelerates the oxidation aging. In principle, other means of acceleration, such as an increase of the oxygen partial pressure, could be used, however this type of equipment is not available in our experimental facilities.

Moreover, the order of magnitude of the propagation velocity is micrometers per hour. Since the oxidation-driven propagation is slow, it is interesting to carry out simultaneously multiple tests. For this reason, a smaller and lighter drum is conceived and manufactured (Fig. 6.4) taking care to make the drum's center of gravity overlap with its center of rotation. The new geometry of the drum allows to carry out three tests in the climatic chamber at the same time.

At last, in the oxi-delamination configuration, the test is carried out under force control. The upper frame is fixed to the climatic chamber, whereas the lower frame is loaded with weights whose resultant force F_{ext} is higher than F_e , but lower than F_d .

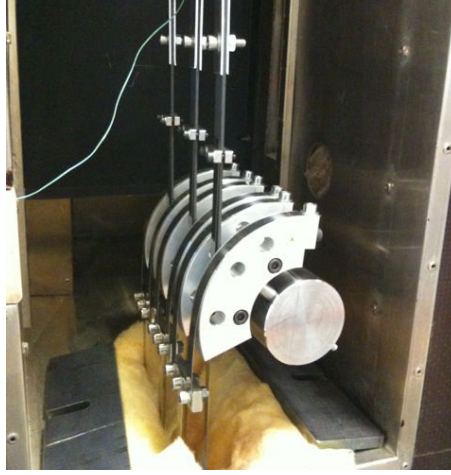


Figure 6.4: The three test setups in the climatic chamber

As it has been explained in Section 6.2.1, an applied force corresponds to an available energy release rate, G_{ext} , calculated as

$$G_{ext} = \frac{(F_{ext} - F_e)(r_2 - r_1)}{r_1 w} \quad (6.6)$$

In this case, G_{ext} is smaller than the G_c of unaged composite. Consequently, the delamination will not propagate until the interface is weakened by the oxidation aging and G_c on the crack tip reduces to G_{ext} . A measure of the relative displacement between the drum and the specimen, carried out with displacement transducers which are set outside of the climatic chamber, allows to measure the crack propagation velocity.

The same specimens are tested by different loading (F_{ext}). Each test lasts a week. The measured propagation velocities give an indication of the oxidation level on the crack tip corresponding to a given available strain energy release rate.

The displacements associated to the crack propagations are very small compared to the overall displacements associated to the tests, their accurate measure is an experimental difficulty which has been only partially overcome. The temperature oscillation within the climatic chamber provides a source of noise, since it causes different dilations between the different elements of the setup and, thus, generates an oscillation in the measure of the displacement. Fig. 6.5 shows the influence of the temperature measured with a thermocouple placed near one of the samples (right vertical axis) on the measure of the displacement over the same time frame (left vertical axis). Since the dilatation due to the temperature is reversible, an integration of measurement over a long duration can eliminate this noise. It should be also pointed out that, while the target temperature set for the climatic chamber was $150\text{ }^\circ\text{C}$, the temperature measured by the thermocouple placed beside the specimen was $133 \pm 2\text{ }^\circ\text{C}$.

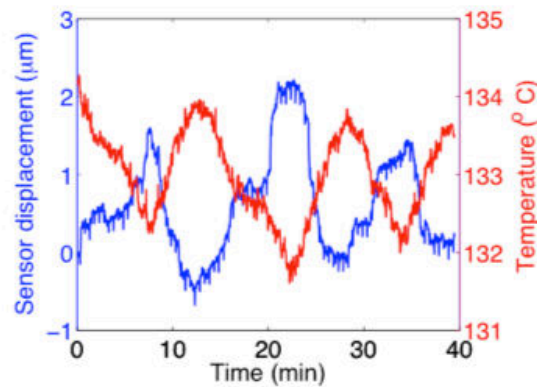


Figure 6.5: Effect of the temperature oscillation on the displacement measured by the sensor ($G_{ext} = 100 J/m^2$)

6.3 Results

6.3.1 G_c of unaged samples

Fig. 6.6 shows the results of three displacement-driven CDP tests performed in the climatic chamber on three different sample at a target temperature of $150^\circ C$. The classical test post-treatment (Eq. (6.5)) allows to identify the initial G_c for the three specimens in a range of $347\text{-}372 J/m^2$ and to fix the forces to be used for the oxy-delamination tests.

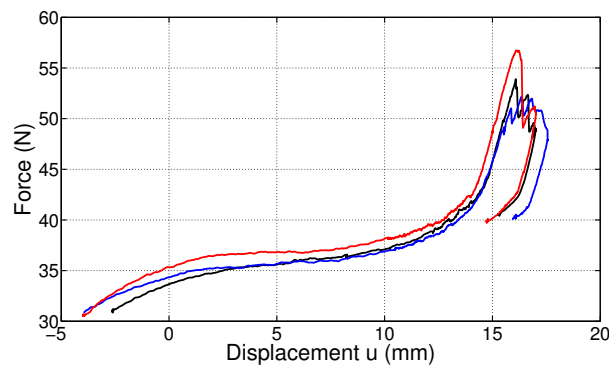


Figure 6.6: Force versus displacement for the displacement-driven CDP tests

The same samples are then used for the oxy-delamination tests for two reasons. First, it is more reasonable to compare G_c of the same sample before and after the aging. Furthermore, the displacement-driven delamination allows to initiate a real crack for the following tests, which is more realistic compared with the artificial pre-delaminated zone created during the manufacture of samples.

6.3.2 Evolution of the displacement during the oxi-delamination tests

The samples were then tested with increasing F_{ext} in the climatic chamber at a target temperature of $150\text{ }^{\circ}\text{C}$. Fig. 6.7 shows the measured displacements versus the time for three samples loaded with a same external force of 44 N (equivalent to $G_{ext} \approx 200\text{ J/m}^2$). In order to smooth out the sources of noise, the velocity associated to a given instant is extracted by fitting the displacement slope over a period of ± 24 hours. The velocities versus the time are given in Fig. 6.8.

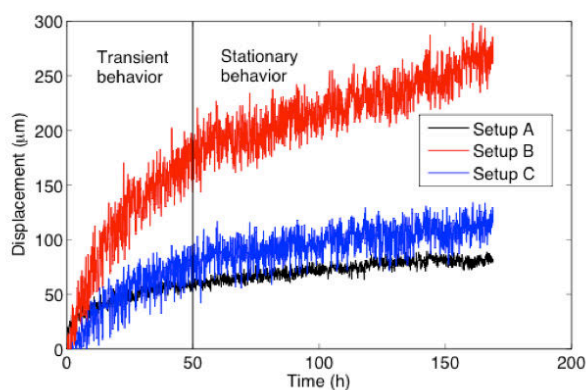


Figure 6.7: The measured displacement under a load of 44 N at $133\pm 2\text{ }^{\circ}\text{C}$ versus test time

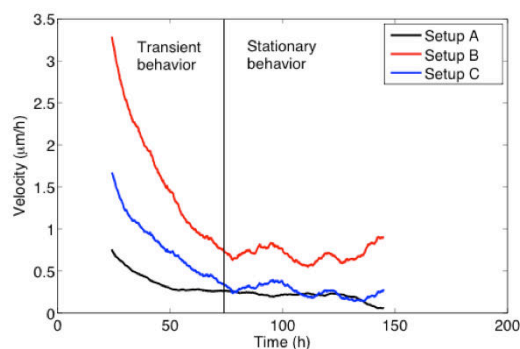


Figure 6.8: The propagation velocity under a load of 44 N at $133\pm 2\text{ }^{\circ}\text{C}$ versus test time

In all the measurements, a transient phase can be observed, followed by a stationary phase with constant velocity, generally after 50 hours of aging (Fig. 6.8). The velocity during the stationary phase could be related to an oxidation level (see Section 6.4): the average velocity after 50 hours is extracted for each level of imposed F_{ext} .

The transient phase may be associated to history effects, such as viscosity, which can come into play at a global level, polluting the local measurement of the crack tip. For this reason, a second series of tests was carried out, in which one of the three samples tested at the same time was used as a reference sample: it was loaded with the same mass as the others, but the delamination was mechanically blocked. The reference sample allowed to prove the presence of the global viscosity and friction effects on the displacement measurements, but these effects were not considered sufficient to completely explain the presence of the transient phase.

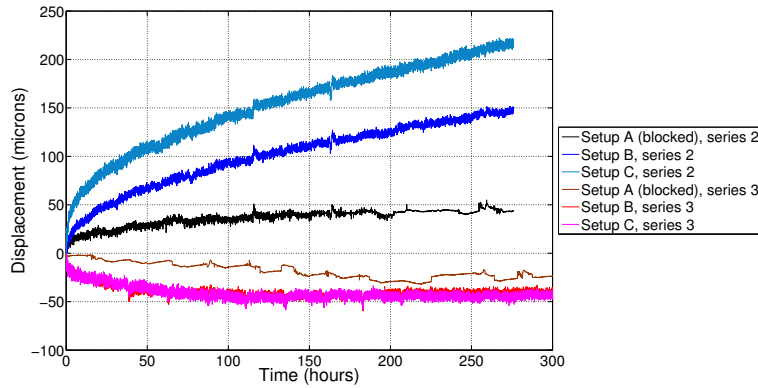


Figure 6.9: Displacement-time plots for increasing to 44 N (series 2) and decreasing to 44 N (series 3) load steps.

A third series of tests was then carried out, in which the external loads were decreased, rather than increased, at each step. Results for the same load level for increasing and decreasing external loads are given in Fig. 6.9. The transient phase is significantly different; furthermore, in the case of decreasing load steps, the crack propagation does not seem to have resumed even after 300 hours of aging. Local viscous effects, which have probably enhanced by the high temperature, could play a role in the observed behavior. The complete modeling and exploitation of these results is in progress, the model discussed in Section 6.4 does not account for viscous effects.

6.3.3 The propagation velocities under different external loads

The available strain energy release rate versus the inverse of the stationary propagation velocity obtained for increasing loads are plotted in Fig. 6.10. The stationary propagation velocity increases with the increase of G_{ext} . The presence of an external mechanical load accelerates significantly the propagation velocity compared with the velocity of self-cracking ($0.03 \mu m$) [57]. For G_{ext} lower than $100 J/m^2$, no significant propagation is observed on the test time frame. This gives an indication of the maximum degradation of the strain energy release rate associated to oxidation.

As the velocity is inversely proportional to the time, $\frac{1}{v}$ contains the information on

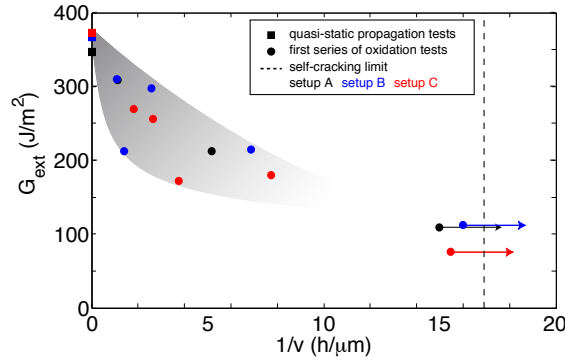


Figure 6.10: Different available energy release rate (G_{ext}) versus $1/v$

the aging time required to reduce G_c of the unaged samples to the available energy release rate G_{ext} and to propagate the crack. When plotting $\frac{1}{v}$ versus G_{ext} , it is not difficult to understand that a longer aging time (higher $\frac{1}{v}$) reduces G_c to a lower level which is almost half of the unaged samples.

In the following section, the efforts is going to be carried out to relate the propagation velocity to the oxidation levels via a diffusion/reaction model taking into account the advance of the delamination tip.

6.4 Modeling of G_c at different oxidation levels

In previous studies [23, 89, 91], the general expression of the one dimensional diffusion/reaction process of the oxidation aging in polymers or in composite materials has been stated as

$$\frac{\partial C}{\partial t} = D \frac{\partial^2 C}{\partial x^2} - R(C) \quad (5.12)$$

where $C(x, t)$ is the oxygen concentration, D is the diffusion coefficient and $R(C)$ is the instant oxygen consumption in the oxidation reactions. The concentration of the oxidation products (Q) generated by the oxidation reactions (Eq. (1.41)) could be used as the indicator of the oxidation levels. The aim of this section is to relate the oxidation levels at the crack tips (Q) to the variation of G_c .

$$Q(x, t) = \int_0^t R(C(x, \tau)) d\tau \quad (1.41)$$

For samples used in oxy-delamination test, since the exposed surface advances with the crack tip, the prediction of Q should take into account the propagation of the de-

lamination. Only the delamination during the stationary propagation phase is studied. A mobile coordinate (\bar{x}) associated to the crack tip is introduced as

$$\bar{x} = x - vt \quad (6.7)$$

where v is the stationary propagation velocity. It was observed that the velocity of the delamination propagation is of the order of the micrometers per hour. On the other hand, the diffusion/reaction process takes less than an hour to reach the stationary state of the oxygen concentration at the crack tip [89]. Therefore, the delamination propagation time is much longer than the time associated to diffusion/reaction and the concentration profile on the crack tip can be considered stationary:

$$\frac{\partial C}{\partial t} = 0 = D \frac{\partial^2 C}{\partial \bar{x}^2} - R(C) \Rightarrow C(x, t) = C_s(\bar{x}) \quad (6.8)$$

where $C_s(\bar{x})$ is a constant profile of the oxygen concentration from the crack tip as the function of the propagation velocity moving with the crack tips as shown in the Fig. 6.11.

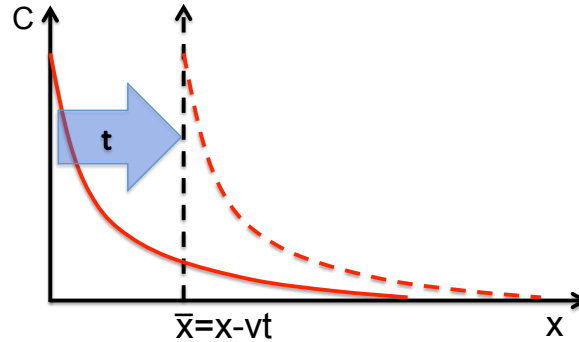


Figure 6.11: Example of the constant profile of the oxygen concentration moving with the crack tip

The concentration of the oxidation products at the crack tip ($Q(\bar{x})$) can be obtained from the following equation

$$\begin{aligned} Q(x, t) &= \int_{t_b}^t R(C_s(x - v\tau)) d\tau \\ &= \frac{-g(x - vt) + g(x - vt_b)}{v} \\ &= \frac{-g(\bar{x})}{v} \\ &= Q(\bar{x}) \end{aligned} \quad (6.9)$$

where g is the integral of the composed function $(R \circ C_s)$, t_b is the time when $C(x_s, t \leq t_b) = 0$. The oxidation level $(Q(\bar{x}))$ at the crack tip is thus proportional to $\frac{1}{v}$. The function g can be identified if the diffusion/reaction model is known.

Further modeling work is needed to account for the presence of viscous effects and, thus, to be able to account for all of the results obtained with the oxi-delamination test.

6.5 Conclusions

The oxy-delamination test proposed in this chapter allows to obtain some information on the fracture toughness G_c of the oxidized material. Crack propagation was observed to occur for values of the available strain energy release rate up to half of the unaged value, which confirms a decrease of the critical strain energy release rate for the oxidized material. The propagation velocities for different external loads can be used directly for specimens which evolve under the same environmental and mechanical conditions. A diffusion/reaction model was proposed to link the measured propagation velocity to an oxidation level and, thus, to identify G_c as a function of the oxidation level. Further work is needed to interpret and account for the history effects which were observed during the oxi-delamination tests.

Conclusion and perspectives

This work presents a contribution towards the understanding and modeling of the oxidation aging of composite materials and its coupling with their mechanical behavior. While the behavior of the oxidized neat resin is relatively well understood, the understanding of the oxidized composite material, especially its behavior at the scale of the laminate, is limited and phenomenological. Experimental and modeling work has been performed in this thesis to give our contribution on methodological aspects of this subject. A meso-scale modeling strategy taking into account the effects of the oxidation aging has been proposed to describe and predict the transverse cracking behavior of the oxidized samples. Experimental tests coupling oxidation and mechanical behavior were carried out: in particular, a new oxi-delamination test was developed to identify the fracture toughness of the aged composite material, which is difficult to obtain using classical test methods.

Preliminary microscopic observations on the polished sections of the oxidized samples confirmed the anisotropic propagation of the oxidation aging on our material by monitoring the thickness of the oxidized/damaged zone. The oxidation aging impacts preferentially the surfaces perpendicular to the fibers due to the presence of the fiber/matrix interphase and the damage in this zone. Moreover, spontaneous cracks crossing partially the oxidized ply, which is not a classical mode of cracking in laminated composites, have been observed on the $[90/0]_s$ samples aged at 180 °C in the air for 6 weeks.

The meso-scale modeling strategy of the LMT-Cachan is extended to the study of the oxidation aging. The proposed strategy studies the problem starting from the micro-scale properties of the oxidized matrix at the fiber/matrix scale and moving up to the prediction of the mesoscale behavior of the oxidized ply via an homogenization method. The aim is to be able to study the behavior of laminated composite specimens, describing each ply and interface at the meso-scale.

At the fiber/matrix scale, the elastic properties and the volume of the oxidized matrix, which vary with the oxidation levels, have been related to the variation of the mesoscale properties of the composite material with a periodic homogenization method. The homogenized mesoscale elastic modulus and shrinkage have been respectively modeled as functions of the relative concentration of the oxidation products. The homogenized description does not account for the development of damage during aging, which could result in a decrease of the elastic modulus of the oxidized composite. Experimental results of free vibration tests on oxidized and non oxidized $[90/0]_s$ specimens show evidence of a decrease in the global flexural stiffness of the laminate, which points towards the presence of damage in specimens which were aged at 180 °C in air for more than 3 weeks.

The oxygen diffusion from the surface parallel to the fibers is modeled as a one dimensional diffusion/reaction process, which results in a non-homogeneous oxidation of the external ply. To simply matters for a meso-scale description, the oxidized composite ply is considered here to be composed of two layers, the non-oxidized layer and the homogeneous oxidized layer, in which the oxidation level is constant and evolves with the aging time.

The ply description using two homogeneous layers and the properties of the oxidized composite predicted via the homogenization method are used to construct a micro-scale model of a laminated composite and to understand and predict the transverse cracking behavior of oxidized $[90/0]_s$ specimens. The evolution of transverse cracking during tensile loading for different durations of aging was observed experimentally, using Digital Image Correlation in order to automatically trace the crack density as a function of the average tensile strain. The experiments showed that the average strain associated to transverse cracking decreases and the crack density increases with the increase of the aging time. In the specimens aged at 180 °C in air for 6 weeks, partial transverse cracks were observed before loading and they should be taken into account in the modeling.

The micro-scale model allows to interpret and reproduce the experimental results. First of all, calculations of the strain energy release rates for different crack lengths allow to explain the presence of partial cracks from an energetic point of view. Indeed, the shrinkage effect of the oxidation aging stores energy in the oxidized ply. In some situations, the strain energy release rate of a crack crossing only the oxidized layer is higher than the one of a crack crossing the entire ply, which leads the partial cracking to be preferential.

Due to the presence of partial cracks, incremental simulations are then performed to simulate the cracking behavior of the oxidized ply under a tensile load taking different possible scenarios into account. The classical mode of cracking, which is cracks crossing the entire ply, is found to dominate the cracking behaviors of $[90/0]_s$ samples aged for 1 and 3 weeks at 180° in the air. However, on the samples aged for 6 weeks, partial cracking is proved to be preferential at low applied longitudinal strain. The increase of the partial cracks density is soon replaced by the propagation of partial cracks through the entire oxidized ply at higher applied longitudinal strains.

A first meso-scale model is proposed, in which an oxidized ply is described as two related layers with different elastic properties and crack densities. The relation between the oxidation level, the applied strain and the crack densities in the two layers is explicitly calculated via micro-scale simulations.

In the micro-scale modeling of transverse cracking, the fracture toughness of the oxidized material was considered to be the same as the one of the unaged material for lack of experimental information. Indeed, the standard cracking and delamination tests do not allow to identify the effect of oxidation on the critical strain energy release rate. To this aim, a new oxi-delamination test has been developed based on the standard

climbing drum peel test. The test studies the propagation of a Mode I delamination under combined external mechanical loading and oxidation. G_c of the oxidized samples is found to decrease with the increasing of the aging time. A model has been proposed to relate G_c with the concentration of the oxidation products, which represents the oxidation levels, via the stationary propagation velocity measured from the test. For the time being, this model does not account for the history effects which were observed in the experimental tests.

Although the above modeling activities or experimental activities have provided a better understanding of the behavior of the oxidized laminated composites, some information is still missing, which requires the efforts on multi directions.

First, the modeling strategy presented in this thesis relies strongly on the micro-scale studies. One has to repeat the micro-scale incremental studies for the samples of any other oxidation levels or of any other sample sequences. A better understanding on the interactions between the homogeneous oxidized layer and the unoxidized layer is required. A model which can be applied into general situations can be constructed by introducing a coupling parameter to model the cracking behavior, which involves several scenarios. Also, the diffuse damage (fiber/matrix interface debonding) is another major damage mechanism for the oxidized composite materials which was not account for in this work. A better modeling of this mechanism and its the coupling with oxidation propagation require a better understanding of the microstructure of the oxidized composite material. It can be considered to introduce a interface fracture criterion and the damage assisted diffusion into the fiber/matrix scale model and use the homogenization method to obtain the mesoscale damage behavior or diffusion process.

The development of the models requires tests to identify the necessary parameters. However the classic standard tests for the unaged samples do not seem to be appropriate enough to identify the properties of oxidized zone whose thickness is small compared with the entire thickness of laminate. It should be considered to maximize the effect of the oxidized layer on the global specimen behavior, for example using thinner specimens in tensile tests or thicker specimens in vibration tests. Non-standard tests and the associated identification method developed for the oxidized samples may be also required in the following study. The oxy-delamination test for the G_c have provided interesting information, but there is still some difficulties to overcome before a clear quantitative identification carried out, for example the viscoelastic of the material.

Bibliography

- [1] Z. Hashin, Failure criteria for unidirectional fiber composites. *Journal of Applied Mechanics*, 47:329–334, 1980.
- [2] S. Li, S. Ghosh, Modelling interfacial debonding and matrix cracking in fiber reinforced composites by the extended Voronoi cell fem. *Finite Elements in Analysis and Design*, 43:397–410, 2007.
- [3] S. Tsai, E. Wu, A general theory of strength for anisotropic materials. *Journal of Composite Materials*, 5:58–80, 1971.
- [4] P. Ladevèze, Sur la mécanique de l’endommagement des composites, in: C. Bathias, D. Menkès (Eds.), *Comptes-rendus des JNC5*, Pluralis Publication, Paris, 667–683, 1986.
- [5] P. Ladevèze, E. LeDantec, Damage modelling for elementary ply for laminated composites. *Composite Science and Technology*, 43:257–267, 1992.
- [6] O. Allix, P. Ladevèze, Interlaminar interface modelling for the prediction of delamination. *Composite Structures*, 22:235–242, 1992.
- [7] P. Ladevèze, Multiscale computational damage modelling of laminate composites. In : *Multiscale modelling of damage and fracture processes in composite materials*, Springer Vienna, CISM courses and lectures, New York, 171-212, 2005.
- [8] P. Ladevèze, G. Lubineau, On a damage mesomodel for laminates: micro-meso relationships, possibilities and limits. *Composites Science and Technology* 61:2149–2158, 2001.
- [9] P. Ladevèze, G. Lubineau, An enhanced mesomodel for laminates based on micromechanics. *Composites Science and Technology*, 62:533–541, 2002.
- [10] P. Ladevèze, G. Lubineau, On a damage mesomodel for laminates: micromechanics basis and improvement. *Mechanics of Materials*, 35:763–775, 2003.

- [11] G. Lubineau, P. Ladevèze, Construction of a micromechanics-based intralaminar mesomodel and illustrations in ABAQUS/Standard. *Computational Materials Science*, 43:137–145, 2008.
- [12] O. Allix, D. Leveque, L. Perret, Identification and forecast of delamination in composite laminates by an interlaminar interface model. *Composites Science and Technology*, 58: 671-678, 1998.
- [13] L. Johnson, R. Eby, M. Meador, Investigation of oxidation profile in PMR-15 polyimide using atomic force microscope (AFM). *Polymer*, 44:187-197, 2003.
- [14] L. Olivier, N. HO, J. Grandidier, M. Lafarie–Frenot, Characterization by ultra-micro indentation of an oxidized epoxy polymer: Correlation with the predictions of a kinetic model of oxidation. *Polymer Degradation and Stability*, 93:489–97, 2008.
- [15] X. Colin, J. Verdu, Strategy for studying thermal oxidation of organic matrix composites. *Composites Science and Technology*, 65:411–419, 2005.
- [16] J. Decelle, N. Huet, N. Bellenger, Oxidation induced shrinkage for thermally aged epoxy networks. *Polymer Degradation and Stability*, 81:239-248, 2003.
- [17] K. Pochiraju, G. Tandon, G. Schoeppner, Evolution of stress and deformations in high-temperature polymer matrix composites during thermo-oxidative aging. *Mechanics of Time-Dependent Materials*, 12:45–68, 2008.
- [18] M. Lafarie-Frenot, J. Grandidier, M. Gigliotti, L. Olivier, X. Colin, J. Verdu, J. Cinquin, Thermo-oxidation behavior of composite materials at high temperatures: A review of research activities carried out within the COMEDI program. *Polymer Degradation and Stability*, 95:965-974, 2010.
- [19] A. Parvizi, K. Garrett, J. Bailey. Constrained cracking in glass fibre-reinforced epoxy cross-ply laminates. *Journal of Material Science*, 13:195-201, 1978.
- [20] ASTM-D1781. Standard test method for climbing drum peel for adhesives.
- [21] D. Lévêque, A. Schieffer, A. Mavel, J. Maire, Analysis of how thermal aging affects the long-term mechanical behavior and strength of polymer–matrix composites. *Composites Science and Technology*, 65:403–409, 2005.
- [22] M. Lafarie-Frenot, S. Rouquie, Influence of oxidative environments on damage in c/epoxy laminates subjected to thermal cycling. *Composites Science and Technology*, 64:1725–1735, 2004.
- [23] X. Colin, 2000, Ph.D. thesis, Modélisation cinétique de la thermo-oxydation de matériaux polymères et composites á hautes performance thermomécanique, Ecole Nationale Supérieure des Arts et Metiers, Paris.

- [24] X. Buch, M. Shanahan, Thermal and thermo-oxidative ageing of an epoxy adhesive. *Polymer Degradation and Stability*, 68:403-411, 2000.
- [25] T. Dyakonov, P. Mann, Y. Chen, T. William, K. Stevenson, Thermal analysis of some aromatic amine cured model epoxy resin systems-II: Residues of degradation. *Polymer degradation and stability*, 54:67-83, 1996.
- [26] X. Colin, J. Verdu, Aging of organic matrix composite materials. in: *Wiley Encyclopedia of Composites*, John Wiley & Sons, Inc., 2011
- [27] N. Rasoldier, X. Colin, J. Verdu, M. Bocquet, L. Olivier, L. Chocinski–Arnault, M.–C. Lafarie–Frenot, Model systems for thermo-oxidised epoxy composite matrices, *Composites: Part A: Applied Science & Manufacturing*, 39:1522-1529, 2008.
- [28] L. Chocinski-Arnault, L. Olivier, M. Lafarie-Frenot, Effects of thermal oxidation on an epoxy–amine thermoset studied by mechanical spectroscopy. *Materials Science and Engineering A*, 521-522:287–290, 2009.
- [29] P. Ladevèze, G. Lubineau, D. Marsal, Towards a bridge between the micro- and mesomechanics of delamination for laminated composites. *Composites Science and Technology*, 66:698–712, 2006.
- [30] O. Allix, P. Feissel, P. Thevenet. A delay damage mesomodel of laminates under dynamic loading : basic aspects and identification issues. *Computers & Structures* 81:1177-1192, 2003.
- [31] J. Guimard, O. Allix, N. Pechnik, P. Thevenet, Characterization and modeling of rate effects in the dynamic propagation of mode-II delamination in composite laminates. *International journal of fracture*, 160:55-71, 2009.
- [32] E. Abisset, F. Daghia, P. Ladevèze. On the validation of a damage mesomodel for laminated composites by means of open-hole tensile tests on quasi-isotropic laminates. *Composites Part A: Applied Science and Manufacturing*, 42:1515–1524, 2011.
- [33] C. Hochard, P. Aubourg, J. Charles, Modelling of the mechanical behaviour of woven-fabric CFRP laminates up to failure. *Composites Science and Technology*, 61:221-230, 2001.
- [34] J. Bolland, C. Gee, Kinetic studies in the chemistry of rubber and related materials. II. The kinetics of oxidation of unconjugated olefins. *Transactions of the Faraday Society*, 42:236-244, 1946.
- [35] T. Kenneth, Gillen, L. Roger, C. Sandia, Techniques for Monitoring Heterogeneous Oxidation of Polymers. *Handbook of Polymer Science and Technology*, 1989.

- [36] P. Ladevèze, F. Daghia, E. Abisset and C. Le Mauff, A micromechanics-based interface mesomodel for virtual testing of laminated composites. *Advanced Modeling and Simulation in Engineering Sciences*, 1:7-23, 2013
- [37] L. Audouin, V. Langlois, J. Verdu, J. de Bruijn, Role of oxygen diffusion in polymer ageing: kinetic and mechanical aspects. *Journal of Materials Science*, 29:569-583, 1994.
- [38] M. Minervino, 2013, Ph.D.thesis, Effets de la thermo oxydation sur le comportement mécanique de matériaux composites pour applications aéronautiques. Ecole Nationale Supérieure de Mécanique et d'Aérotechnique, Poitiers
- [39] G. Tandon, K. Pochirajub, G. Schoeppner, Thermo-oxidative behavior of high-temperature PMR-15 resin and composites. *Materials Science and Engineering: A*, 498:150–161, 2008.
- [40] B. William, Characterization of PMR-15 polyimide resin composition in thermo-oxidatively exposed graphite fiber composite, *NASA Technical Report*, 80-C-10
- [41] T. Kenneth, T. Gillen, L. Roger, A. Carlos. Quintana modulus profiling of polymers. *Polymer degradation and stability*, 17:31-47, 1987.
- [42] M. Celina, Oxidation profiles of thermally aged nitrile rubber. *Polymer degradation and stability*, 60:493-504, 1998.
- [43] R. Clough, K. Gillen, Oxygen diffusion effects in thermally aged elastomers. *Polymer Degradation and Stability*, 38:47-56, 1992.
- [44] K. Pochiraju, G. Tandon, Interaction of oxidation and damage in high temperature polymeric matrix composites. *Composites: Part A*, 40:1931–1940, 2009.
- [45] H. McManus, R. Cunningham, Materials and mechanics analyses of durability tests for high-temperature. *High temperature and enviromental effects on polymeric composite: 2en volume*, ASTM STP 1302, 1997.
- [46] H. McManus, B. Foch, R. Cunningham, Mechanism-based modeling of long-term degradation. *J. Compos. Technol.*, 223:146–152, 2000.
- [47] X. Colin, C. Marais, J. Verdu, 2001, Thermal Oxidation Kinetics for a Polybis-maleimide. *Journal of Applied Polymer Science*, 82:3418–3430, 2001.
- [48] J. Richeton, G. Schlatter, K. Vecchio, Y. Rémond, S. Ahzi, A unified model for stiffness modulus of amorphous polymers across transition temperatures and strain rates. *Polymer*, 46:8194-8201, 2005.

- [49] L. Olivier, C. Baudet, D. Bertheau, J. Grandidier, M. Lafarie-Frenot, Development of experimental, theoretical and numerical tools for studying thermo-oxidation of CFRP composites. *Composites: Part A*, 40:1008–1016, 2008.
- [50] K. Pochiraju, G. Tandon. Modeling thermo-oxidation layer growth in high temperature resins. *Journal of Engineering Materials and Technology*, 128:107–16, 2006.
- [51] G. Tandon, K. Pochiraju, G. Schoeppner. Modeling of oxidative development in PMR-15 resin. *Polymer Degradation and Stability*, 91:1861–9, 2006.
- [52] G. Schoeppner, G. Tandon, E. Ripberger. Anisotropic oxidation and weight loss in PMR-15 composites. *Composites: Part A*, 38:890–904, 2007
- [53] M. Gigliotti, L. Olivier, D. Vu, J. Grandidier, M. Lafarie-Frenot, Local shrinkage and stress induced by thermo-oxidation in composite materials at high temperatures. *Journal of the Mechanics and Physics of Solids*, 59:696–712, 2011
- [54] D. Vu, M. Gigliotti, M. Lafarie-Frenot, Experimental characterization of thermo-oxidation-induced shrinkage and damage in polymer–matrix composites. *Composites Part A: Applied Science and Manufacturing*, 2012, 43:577–586.
- [55] D. Vu, M. Gigliotti, M. Lafarie-Frenot, The effect of thermo-oxidation on matrix cracking of cross-ply $[0/90]_s$ composite laminates. *Composites Part A: Applied Science and Manufacturing*, 44:114–121, 2013.
- [56] M. Lafarie-Frenot, Damage mechanisms induced by cyclic ply-stresses in carbon–epoxy laminates: Environmental effects. *International Journal of Fatigue*, 28:1202–1216, 2006.
- [57] X. Colin, A. Mavel, C. Marais, J. Verdu, Interaction between cracking and oxidation in organic matrix composites. *Journal of Composite Materials*, 39:1371–1389, 2005.
- [58] K. Bowles, Thermal and mechanical durability of graphite-fiber-reinforced PMR-15 composites. *Progress in Durability Analysis of Composite Systems*, 1998.
- [59] J. Nelson, Long-Term Thermal Aging of Two Graphite/Polyimide Composite Materials. *NASA Technical Paper*, 2369, 1984.
- [60] H. Parvatareddy, J. Wang, D. Dillard, T. Ward, M. Rogalski, Environmental aging of high-performance polymeric composites: Effects on durability. *Composites Science and Technology*, 53:399–409, 1995.
- [61] ASTM D638M-91 Test Method for Tensile Properties of Plastics

- [62] T. Tsotsis, S. Lee, Long-term thermo-oxidative aging in composite materials: Failure mechanisms. *Composites Science and Technology*, 58:355-368, 1998.
- [63] O. Ozcelik, L. Aktas, M. Altan, Thermo-oxidative degradation of graphite/epoxy composite laminates: Modeling and long-term predictions. *eXPRESS Polymer Letters*, 3:797-803, 2009.
- [64] J. Cinquin, B. Medda, Influence of laminate thickness on composite durability for long term utilisation at intermediate temperature (100-150 °C). *Composites Science and Technology*, 69:1432-1436, 2009.
- [65] T. Tsotsis, S. Kellerb, J. Bardisc, J. Preliminary, Evaluation of the use of elevated pressure to accelerate thermo-oxidative aging in composites. *Polymer Degradation and Stability*, 64:207-212, 1999.
- [66] S. Rouquie, M. Lafarie-Frenot, J. Cinquin, A. Colombaro, Thermal cycling of carbon/epoxy laminates in neutral and oxidative environment. *Composites Science and Technology*, 65:403-409, 2005.
- [67] M. Lafarie-Frenot, Damage mechanisms induced by cyclic ply-stresses in carbon-epoxy laminates: Environmental effects. *International Journal of Fatigue*, 28:1202-1216, 2006.
- [68] G. Lubineau, P. Ladevèze, D. Violeau, Durability of CFRP laminates under thermomechanical loading: A micro-meso damage model. *Composites Science and Technology*, 66:983-992, 2006
- [69] G. Lubineau, D. Violeau, P. Ladevèze, Illustrations of a microdamage model for laminates under oxidizing thermal cycling. *Composites Science and Technology*, 69:3-9, 2009
- [70] J. Nelson, Thermal aging of graphite polyimide composites. *Long-term behavior of composites*, 206-221, 1983.
- [71] Y. Weitsman, Stress assisted diffusion in elastic and viscoelastic materials. *Journal of the Mechanics and Physics of Solids*, 35:73-97, 1987.
- [72] R. Ripberger, G. Tandon, G. Schoeppner, Experimental techniques for characterizing thermo-oxidative behavior in high temperature polyimide composites. In: *Proceedings of the 2005 SEM annual conference and exposition*, Portland, 2005.
- [73] M. Lafarie-Frenot, S. Rouquie. Influence of oxidative environments on damage in C/epoxy laminates subjected to thermal cycling. *Composites Science and Technology*, 64:1725-35, 2004.

- [74] T. Tsotsis, Y. Weitsman, Energy release rates for cracks caused by moisture absorption in Graphite/Epoxy. *Composites. Journal of Composite Materials*, 24: 483-496, 1990
- [75] A. Benssousan, J. Lions, G. Papanicoulau, *Asymptotic Analysis for Periodic Structures*, American Mathematical Soc., Rhode Island, 2011.
- [76] A. Toledano, H. Murakami, A high order mixture model for periodic particulate composites. *International Journal of Solids and Structures*, 23:989-1002, 1987.
- [77] J. Guedes, N. Kikuchi, Preprocessing and postprocessing for materials based on the homogenization method with adaptive finite element methods. *Computer Methods in Applied Mechanics and Engineering*, 83:143-198, 1991.
- [78] S. Ghosh, K. Lee, S. Moorthy, Two scale analysis of heterogeneous elastic-plastic materials with asymptotic homogenization and Voronoi cell finite element model. *Computer Methods in Applied Mechanics and Engineering*, 132:63-116, 1996.
- [79] Torayca T300 Data Sheet, URL: <http://www.toraycfa.com/pdfs/T300JDataSheet.pdf>
- [80] E. Totry, J. Molina-Aldareguia, C. Gonzalez, J. Lorca. Effect of fiber, matrix and interface properties on the in-plane shear deformation of carbon-fiber reinforced composites. *Composites Science and Technology*, 70:970-980, 2010.
- [81] M. Ueda, T. Takiguchi. Measurement of transverse Young's modulus of fibers by angular characteristics of ultrasonic scattering. *Advanced Composite Materials*, 1:309-20, 1991.
- [82] P. Meurs, P. Schreurs, T. Peijs, H. Meijer. Characterization of interphase conditions in composite materials. *Composites Part A*, 21A:781-6, 1996.
- [83] R. Maurin, P. Davies, N. Baral, C. Baley. Transverse Properties of Carbon Fibres by Nano-Indentation and Micro- mechanics. *Applied Composite Materials*, 15:61-73, 2008.
- [84] H. Miyagawaa, C. Satoc, T. Masea, E. Drowna, L. Drzala, K. Ikegami, Transverse elastic modulus of carbon fibers measured by Raman spectroscopy. *Materials Science and Engineering: A*, 412:88-92, 2005.
- [85] C. Sauder, J. Lamon, Prediction of elastic properties of carbon fibers and CVI matrices. *Carbon*, 43:2044-2053, 2005.
- [86] S. Hsu, T. Vogler, S. Kyriakides, Inelastic behavior of an AS4/PEEK composite under combined transverse compression and shear. Part II: modeling. *International Journal of Plasticity*, 15:807-836, 1999.

- [87] L. Johnson, R. Ebya, M. Meador, Investigation of oxidation profile in PMR-15 polyimide using atomic force microscope (AFM). *Polymer*, 44:187–197, 2003.
- [88] K. Bowles, D. Papadopoulos, L. Inghram, L. McCorkle, O. Klan, Long-time durability of PMR15 matrix polymer at 204, 260, 288, and 316 C. *NASA/TM-2001-210602*, 2001.
- [89] X. Colin, C. Marais, J. Verdu. A new method for predicting the thermal oxidation of thermoset matrices: application to an amine crosslinked epoxy. *Polymer Testing*, 20:795-803, 2001.
- [90] X, Colin, C. Marais, J. Verdu. Kinetic modelling and simulation of gravimetric curves: application to the oxidation of bismaleimide and epoxy resins. *Polymer Degradation and Stability*, 78:545-553, 2002.
- [91] X, Colin, C, Marais, J. Verdu, Kinetic modelling of the stabilizing effect of carbon fibres on thermal ageing of thermoset matrix composites. *Composites Science and Technology*, 65:117-127, 2005.
- [92] A. Schieffer, J. Mairea, D. L ev eque, A coupled analysis of mechanical behaviour and ageing for polymer-matrix composites. *Composites Science and Technology*, 62:543–549, 2002.
- [93] T. Tsotsis, Y. Weitsman, Energy Release Rates for Cracks Caused by Moisture Absorption in Graphite/Epoxy Composites, *Journal of Composite Materials*, 24:483-496, 1990.
- [94] S. Tsai, H. Hahn, *Introduction to composite materials*, Technomic Publishing Company, INC. Lanscater, 1980.
- [95] K. Garrett, J. E. Bailey, Multiple Transverse Fracture in 90° Cross-Ply Laminates of a Glass Fibre-Reinforced Polyester. *Journal of Materials Science*, 12:157–168, 1997.
- [96] J. A. Nairn, S. Hu, Micromechanics of Damage: A Case Study of Matrix Microcracking. *Damage Mechanics of Composite Materials*, 187–243, 1994.
- [97] A. Highsmith, K. Reifsnider, *Damage in Composite Materials*, ASTM STP 775 103, 1982.
- [98] S. McNeill, W. Peters, M. Sutton, Estimation of stress intensity factor by digital image correlation. *Engineering Fracture Mechanics*, 28:101-112, 1987.
- [99] M. Sutton, J. Orteu, H. Schreier, *Image correlation for shape, motion and deformation measurements: basic concepts, theory and applications*. Springer, New York, 2009.

- [100] F. Hild, S. Roux, Digital image correlation. in: *Optical methods for solid mechanics: a full-field approach*, Publisher Wiley-VCH, Berlin, 2012.
- [101] S. Roux, J. Réthoré, F. Hild, Digital Image Correlation and Fracture: An Advanced Technique for Estimating Stress Intensity Factors of 2D and 3D Cracks, *Journal of Physics D: Applied Physics*, 42:214004, 2009.
- [102] W. Riddell, R. Piascik, M. Sutton, W. Zhao, S. McNeill, J. D. Helm, Determining fatigue crack opening loads from near-crack-tip displacement measurements. *Advances in fatigue crack closure measurement and analysis*, 2:157-174, 1999.
- [103] S. Roux, F. Hild, Stress intensity factor measurements from digital image correlation: post-processing and integrated approaches. *International Journal of Fracture*, 140:141–157, 2006.
- [104] K. Garrett, J. Bailey, Multiple transverse fracture in 90° cross-ply laminates of a glass fibre-reinforced polyester. *Journal of Material Science*, 12:157–168, 1977.
- [105] A. Parvizi, J. Bailey, On multiple transverse cracking in glass fibre epoxy cross-ply laminates. *Journal of Materials Science*, 13:2131-2136, 1978.
- [106] P. Manders, T. Chou, F. Jones, J. Rock, Statistical analysis of multiple fracture in 0/90/0 glass fibre/epoxy laminates. *Journal of Materials Science*, 18:2876-2889, 1983.
- [107] Z. Hashin, Finite thermoelastic fracture criterion with application to laminate cracking analysis. *Journal of the Mechanics and Physics of Solids*, 1996, 44:1129, 1996.
- [108] J. Nairn, S. Hu, J. Bark, A critical evaluation of theories for predicting microcracking in composite laminates. *Journal of Materials Science*, 28:5099-5111, 1993.
- [109] A. Nettles, E. Gregory, J. Jackson, Using the Climbing Drum Peel (CDP) Test to Obtain a GIC Value for Core/Face Sheet Bonds. *Journal of Composite Materials*, 41:2863-2876, 2007.
- [110] G. Tandon, W. Ragland, G. Schoeppner, Using optical microscopy to monitor anisotropic oxidation growth in high temperature polymer matrix composites. *Journal of Composite Materials*, 43:583-603, 2009.

List of Figures

1.1	The damage mechanisms in laminated composites [29]	7
1.2	Microscopic observation under lightfield illumination (A1) and differential interference contrast observation (A2) of a polished section of an epoxy resin aged for 200 h at 240 °C in the air [23]	14
1.3	Evolution of the thickness of the oxidized layers according to the two criteria on an epoxy resin aged at 240 °C in the air [23]	14
1.4	(a) Photomicrograph of PMR-15 resin aged at 288 °C in the air (b) Thicknesses of the oxidation layer and of the transition region versus the aging time. [39]	15
1.5	Mass variation of 50 μm thick bismaleimide resin aged in the environment of different oxygen pressure at 240 °C [23]	16
1.6	(a) Volume change of PMR-15 specimen in the air and in the argon [17] (b) Shrinkage of a 70 μm matrix film aged at 180 °C in the air [23]	16
1.7	(a) Shape of dynamic mechanical analysis (DMA) curves for a network before (full line) and after aging (dashed line) [26] (b) Isothermal aging at 150 °C of epoxy resin specimens, the elastic indentation modulus versus the distance from the edge [14]	17
1.8	Oxidation layer growth (lighter regions) and damage evolution in neat PMR-15 resin at 343 °C [44]	18
1.9	Relative oxygen concentration of PMR-15 resin exposed in the air at 288 °C [45]	19
1.10	(a) Mass variation of 50 μm thick bismaleimide resin aged in 1.2 bar oxygen at different temperatures (b) Oxygen concentration profile of bismaleimide aged for different times at 240 ° [23]	21
1.11	Mass variation of 50 μm thick resin aged at different temperatures [23] (a) Bismaleimide in 1.2 bar oxygen (b) Epoxy in 1 bar oxygen	21

1.12	Correlation between the measured elastic indentation modulus (EIT) and the calculated concentration of the oxidation products (Q) [14]	23
1.13	Schematic of the three zones in thermo-oxidation. [50, 51]	24
1.14	(a) Section of unidirectional G30-500/PMR-15 composite aged at 288 °C for different times. (b) Comparison of oxidation growth in the transverse and axial directions of unidirectional composites [52]	25
1.15	Comparison of oxidation growth in the transverse direction of composite and in the neat PMR-15 resin. [52]	25
1.16	(a) SEM observations of specimen surface aged 1000 h in the air at 150 °C (b) Shrinkage of the matrix between fibers with the presence of fiber/matrix debonding measured with CIM [54]	26
1.17	Evolution of TDL for (a) T800/HF655-2 system (b) IM7/977-2 system at 180 °C in the air and the expected cracking mechanisms [57]	27
1.18	Weight loss evolution of different geometries during the isothermal aging at 150 °C [64].	28
1.19	Volume change rates for specimens in the air and in the argon. [52]	29
1.20	Change in transverse modulus of IM8/954-2 composites as a function of the aging time and environment at 150 °C. [60]	29
1.21	Comparison of ultimate axial strains of unaged samples and samples aged for 2 months at 210 °C. [21]	30
1.22	Comparison of X radiographs at 500 cycles in (a) nitrogen (b) air and (c) oxygen [22]	30
1.23	Crack density evolution as functions of the applied stress on [0/90 ₃ /0] specimens aged for different times [55]	31
1.24	(a) Thermo-oxidation induced stress field close to the fibre/matrix interface (along path P1 to P2) (b) Experimentally measured vs. numerically predicted maximum chemical shrinkage depth as a function of the fibre-to-fibre distance in thermo-oxidized composite [18]	32
1.25	Oxidation growth prediction in an unidirectional composite with the orthotropic fiber-interphase assemblage diffusivity and the presence of a discrete crack [44]	32
1.26	Profile of stationary oxygen concentration (a) in the direction along the fibers (b) in the direction transverse to fibers [23]	35
2.1	(a) The geometry of samples (b) The observed surfaces	39
2.2	The surface of an unaged samples after polishing	40

2.3	The light field and the dark field illumination on a plane surface	41
2.4	Dark field illumination on a textured surface	42
2.5	Image of surface of an aged sample under dark field illumination (a) original (b) enhanced	42
2.6	A surface perpendicular to fibers of samples aged for 6 weeks under (a) the light field illumination (b) the dark field illumination	43
2.7	Surfaces perpendicular to fibers under dark field illumination (a) unaged (b) aged for 1 week (c) aged for 3 weeks (d) aged for 6 weeks	44
2.8	Surfaces parallel to fibers under dark field illumination (a) unaged (b) aged for 1 week (c) aged for 3 weeks (d) aged for 6 weeks	45
2.9	Evolutions of the thickness of oxidized/damage zone (a) along the direction of the fibers (b) transverse to the direction of the fibers	46
2.10	The surface of an unaged samples after polishing	48
2.11	Partial cracks of different lengths	48
2.12	Damage assisted propagation of the oxidation aging on samples with partial cracks (a) Light field illumination (b) Dark field illumination	49
2.13	(a) Surface effect (b) Edge effect	50
3.1	(a) Shrinkage of a 70 μm matrix film aged at 150 °C in air, (x) measured by optical microscopy, (o) calculated from experimental values of weight loss and density increase, (-) calculated with Matlab software [16] (b) Epoxy resin, prediction of the concentration of oxidation products after isothermal aging of different times at 150 °C, under atmospheric air. [49]	53
3.2	Shrinkage versus the concentration of oxidation products	54
3.3	Periodic domain with two length scales	55
3.4	(a) Geometry and (b) Mesh of an unit cell	61
3.5	(a) Stress field in the polar coordinate system of samples aged for 6 weeks(Gpa) (b) Stresses along one quarter of the fiber/matrix interface	63
3.6	Non-tensile stress field around the fiber/matrix interface due to the residual thermal shrinkage according to [93]	63
3.7	Homogenized (a) transverse modulus (b) in-plane shear modulus (c) out-of-plane shear modulus versus the relative concentration of oxidation products	65
4.1	Dimension of $[90/0]_s$ samples of HTS/TACTIX material	71

4.2	Setup of tensile test	72
4.3	(a) Global picture (b) Local picture	73
4.4	The longitudinal strain field composed every ZOIs on a sample surface	75
4.5	DIC results of local pictures for increased loading at the average longitudinal strain of (a) 0.29% (b) 0.32% (c) 0.34%	75
4.6	Size of ZOI compared with the maximum crack density	76
4.7	Longitudinal strains of one column of ZOIs versus their longitudinal positions	77
4.8	Analysed crack density evolutions (a) with different thresholds (b) of three columns of ZOIs	77
4.9	Optical observations on zoomed local photos	78
4.10	Tensile stress as functions of average longitudinal strains	78
4.11	Crack density evolutions as a function of the average longitudinal strain of samples (a) unaged (b) aged for 1 week (c) aged for 3 weeks (d) aged for 6 weeks	80
4.12	Crack density evolutions as functions of the average longitudinal strain	81
4.13	Setup of the non-destructive free vibration tests	82
4.14	One example of the test results (a) Vibration history (b) Frequency spectrum	83
5.1	Locally periodic cracking and studied unit cell of sample	91
5.2	Periodic cells of samples with the crack density as (a) ρ (b) 2ρ	92
5.3	(a) G at $\epsilon_{22} = 0.0052$ and (b) $f(\rho)$ versus ρ	92
5.4	(a) G as a function of ρ and ϵ_{22} (b) Example of ρ versus $\epsilon_{22,a}$ at $G_c = 170 J/m^2$	93
5.5	Experimental crack density evolution fitted by analytical results with $G_c = 170 J/m^2$	93
5.6	(a) Real oxidized ply (b) Homogeneous equivalent oxidized layer and unoxidized layer	94
5.7	(a) Calculated concentration of oxidation products of an epoxy resin aged at $150^\circ C$ in the air [14] (b) G30-500/PMR-15 aged at $288^\circ C$ in the air [39]	95
5.8	Predicted profile of q for samples aged for different times in air at $180^\circ C$	98

5.9	Longitudinal stress field of (a) models of healthy sample (b) models of cracked sample	99
5.10	G versus different crack lengths (a) unaged sample (b) all the samples	100
5.11	Illustration of the incremental study	101
5.12	Kinetics of cracking without taking into account partial cracks of the samples aged for different times	102
5.13	Three possible scenarios of cracking	103
5.14	Exemple of the periodic model of $\rho_p = 0.2$ and $\rho_c = 0.3$	103
5.15	Comparison between kinetics of cracking with and without taking into account partial cracks for samples aged for 1008 h at $180\text{ }^\circ\text{C}$ in the air	104
5.16	Kinetics of the complete cracks in the samples aged for different times .	104
5.17	Evolution of G_p and the crack density of complete cracks versus the total strain at $\rho_p = 0.38$	105
5.18	G_t influenced by ρ_p at $\epsilon_a = 0$	106
6.1	Setup of the standard climbing drum peel test [109]	111
6.2	Sample for the climbing drum tests	111
6.3	Typical curve of the applied displacement versus force of a climbing drum peel test	112
6.4	The three test setups in the climatic chamber	114
6.5	Effect of the temperature oscillation on the displacement measured by the sensor ($G_{ext} = 100\text{J}/\text{m}^2$)	115
6.6	Force versus displacement for the displacement-driven CDP tests	115
6.7	The measured displacement under a load of 44 N at $133\pm 2\text{ }^\circ\text{C}$ versus test time	116
6.8	The propagation velocity under a load of 44 N at $133\pm 2\text{ }^\circ\text{C}$ versus test time	116
6.9	Displacement-time plots for increasing to 44 N (series 2) and decreasing to 44 N (series 3) load steps.	117
6.10	Different available energy release rate (G_{ext}) versus $1/v$	118
6.11	Example of the constant profile of the oxygen concentration moving with the crack tip	119

List of Tables

2.1	The automatic polishing protocol	40
2.2	The evolution of the average thickness of the oxidized/damaged layer	46
3.1	Properties of the unaged matrix in the FEM calculations	61
3.2	Fiber properties in the FEM calculations	62
3.3	Matrix modulus and shrinkage versus q	62
3.4	Homogenized material properties of an unaged composite ply	64
3.5	Elastic properties of the oxidized composite material at different levels of q	66
3.6	Shrinkage of composite material versus matrix modulus	66
4.1	Longitudinal modulus of laminated composites aged for different time	79
4.2	The natural frequencies of the samples aged for different times	82
5.1	Parameters used in the diffusion/reaction calculation [23]	97
5.2	The oxidation levels and the properties of the oxidized composite materials aged for different times	98
5.3	Example of the strain energy release rates for different scenarios ($\epsilon_a = 0$, $\rho_p = 0.38$, $\rho_t \approx 0$)	103